Solid State Amperometric Sensor for the In-Situ Monitoring of Slag Composition and Transport Properties

by

Stephen C. Britten

S.B., Materials Science and Engineering (1994)

Massachusetts Institute of Technology

Submitted to the Department of Materials Science and Engineering in Partial Fulfillment of the Requirements for the Degree of Doctor of Philosophy in Metallurgy

at the

Massachusetts Institute of Technology

February 1998

[June 1998]

Signature of Author .....
Department of Materials Science and Engineering
January 9, 1998

Certified by .....
Uday B. Pal
John Chipman Associate Professor of Chemical Processing of Materials
Thesis Supervisor

Accepted by .....
Linn W. Hobbs
John F. Elliott Professor of Materials
Chairman, Departmental Committee on Graduate Students

Solid State Amperometric Sensor for the In-Situ Monitoring of
Slag Composition and Transport Properties

by

Stephen C. Britten

Submitted to the Department of Materials Science and Engineering
on January 9, 1998 in Partial Fulfillment of the Requirements for the Degree of Doctor
of Philosophy in Metallurgy

ABSTRACT

Conventional oxygen sensors have been used for several decades for better process control in metals industries. Such devices can accurately determine the oxidation state of the molten metal phase. Investigators understand the importance of the slag phase on the quality of the final product and therefore similar devices have been implemented recently for analysis of molten oxides. While open circuit potential measurements yield important thermodynamic information, this thesis will show that additional information can be gained by using amperometric techniques.

Three different amperometric techniques were examined for use in an in-situ, zirconia-based sensor to monitor the easily dissociable oxide composition of high temperature metallurgical slags. Applied DC potential steps and impedance frequency sweeps at applied DC potentials were shown to clearly distinguish between slags containing different quantities of FeOx while demonstrating similar oxygen activities – an improvement over conventional oxygen sensor technology. The techniques were also shown to reveal information on transport properties, dissociable oxide type, and buffering capacity of the slag to a given oxidation state.

In a separate set of experiments, coulometric titration was shown to easily differentiate between slags containing different quantities of FeOx in large concentrations. The ion-selective membrane properties of the zirconia allowed the coulometric titration to proceed at current efficiencies near 100% and may be useful for the recovery of commercial metals from oxide waste streams.

Thesis Supervisor: Uday B. Pal
Title: John Chipman Associate Professor of Chemical Processing of Materials

Table of Contents

Table of Figures

Table of Tables

Table of Appendices

Acknowledgements

I would like to thank Prof Uday B. Pal for his helpful guidance throughout the duration of the research. I wish him nothing but the best in all his future endeavors.

Thanks also to my thesis committee for assisting in direction and focus of the project: Prof. Tuller, Prof. Russell, Prof. Latanision, and Prof. Pal.

Discussions with the following individuals made work seem less like work: Prashant Soral, Ashish Agarwal, Shi Yuan, Filippos Patsiogiannis, Sridhar Seetharaman, David Wooley, Ben Nunes, Victor Stancovski, Harold Larson, Prof. Kuo-chih (George) Chou.

The National Science Foundation is gratefully acknowledged for their financial support on the project.

Thanks also to the Office of Naval Research for their financial support via a department of defense (DOD) graduate fellowship.

Most of all, I thank my fiancée, Alex Hou, for her love and confidence throughout the thesis. Alex, I love you with all of my heart – I will always be there for you when you need me.

Table of Symbols

a_i	none	activity of species i
A	cm^2	area
α	none	transfer coefficient
b_0	A	steady state current
b_1	A-$sec^{1/2}$	diffusional current
B	none	basicity
d	cm	distance between electrodes
c_i	mol/cm^3	concentration of species i
C_i^{app}	mol/cm^3	concentration at electrode surface of species i due to applied pot.
C_i^{bulk}	mol/cm^3	concentration of species i in the bulk solution
C_{dl}	F/cm^2	double-layer capacitance
C_W	F/cm^2	frequency dependent Warburg capacitance
D_i	cm^2/sec	diffusion coefficient of species i
E	V	potential of electrode or emf of a reaction
E^o	V	standard potential of electrode (relative to 1atm O_2)
E_{air}^0	V	standard potential of electrode (relative to 0.21 atm O_2)
$E_{air}^{0'}$	V	formal potential of electrode (relative to 0.21 atm O_2)
$E_{1/2}$	V	reversible half wave potential
E_{app}	V	applied potential
f	none	correlation factor
f	hz	frequency
F	C	Faraday constant (96320)
γ_i	none	activity coefficient of species i
γ_{rat}	none	γ_R/γ_O
ΔG	KJ/mol	Gibbs free energy change in a chemical process
ΔG^o	KJ/mol	standard Gibbs free energy change in a chemical process
h	cm	immersion depth of electrode

η	poise	viscosity
η	V	overpotential
i	A	current
i_0	A/cm^2	exchange current density
i_{app}	A	applied current
i_{tot}	A	total current
i(t)	A	AC signal
I_m	A	AC peak current
j	none	sqrt(-1)
k	J/K	Boltzman constant ($1.381x10^{-23}$)
k_r	cm/sec	reaction rate constant
K_{rxn}	changes	equilibrium constant of reaction
L	cm	length of electrode
λ	none	dimensionless kinetic parameter
μ_i	KJ/mol	chemical potential of species i
n	mol/cm^3	concentration of free electrons
n	none	electrons taking part in a reduction reaction
O	(subscript)	oxidized form of the standard system O + ne = R
p	mol/cm^3	concentration of holes
P_{O2}	atm	oxygen partial pressure
P_θ	atm	oxygen partial pressure where $\sigma_{ion}=\sigma_e$
$P_{\theta h}$	atm	oxygen partial pressure where $\sigma_{ion}=\sigma_p$
q	C	charge
Q	C	charge passed during electrolysis
θ	rad	phase angle of offset
r	cm	radius of electrode wire
r_i	cm	atomic radius of species i
R	J/(K-mol)	gas constant (8.314)
R	(subscript)	reduced form of the standard system O + ne = R
R_{ct}	Ω	charge transfer resistance
R_{sol}	Ω	solution resistance

R_W	Ω	frequency dependent Warburg resistance
s	time	Laplace plane variable
σ_i	1/(Ω-cm)	partial conductivity of species I
σ_{ion}	1/(Ω-cm)	ionic conductivity
σ_e	1/(Ω-cm)	electronic conductivity
σ_W	$\Omega/sec^{1/2}$	Warburg impedance variable
t	cm	thickness
t	sec	time
t_i	none	transference number of species i
t_{ion}	none	ionic transference number
T	K	temperature
τ_{dl}	sec	time constant for double-layer charging
u_i	$cm^2/(V\text{-}sec)$	mobility of species i
v(t)	V	AC signal
V	V	applied potential
V_m	V	AC peak voltage
V_{meas}	V	measured potential
ω	rad/sec	angular frequency
X_i	none	mole fraction of species i
X_{rat}	none	X_O/X_R
wt%i	wt%	wt% of species i
z_i	none	valence charge of species i
Z	Ω	impedance
Z'	Ω	real impedance
Z''	Ω	complex impedance
$\|Z\|$	Ω	magnitude of the impedance
Z_W	Ω	Warburg impedance

1 Introduction

Stabilized zirconia based oxygen sensors are utilized extensively throughout the steelmaking process for better control of deoxidation, continuous casting, and ingot-making processes[1,2,3,4] and for the prevention of blowholes, pinholes, or oxide inclusions within the steel[5]. Oxygen activity measurements are usually taken within the molten metal for a direct reading of the PPM oxygen dissolved within the steel melt. However, the composition of the slag phase should not be ignored, because it has a strong influence on the resulting composition of the final metal product. The relative amounts of transition metal oxides such as FeOx, CrOx, MnOx, are known to set the oxygen activity within an oxide melt, thereby controlling the oxidation and reduction reactions which occur at the slag/metal interface. Chemical analysis for these transition oxides require more than 30 minutes while processes such as ladle refining may be completed in less than 30 minutes. This delay creates difficulties in process control. In order to determine slag composition *in-situ*, several investigators have explored the use of zirconia probes to estimate the concentration of FeOx within the slag phase. By measuring the open circuit potential (OCV) across the probe, the oxygen activity of the slag phase can be estimated and then related the FeOx concentration by using knowledge of the slag structure and thermodynamics[6,7,8,9,10]. Unfortunately, such techniques become more difficult if the slag is not in equilibrium with iron or if the slag structure is not well known.

This thesis will demonstrate that additional knowledge of the slag structure and composition can be obtained by utilizing amperometric measurements in conjunction with the aforementioned thermodynamic OCV measurement. An amperometric

measurement yields kinetic information sensitive to the buffering capacity of the slag at a given oxidation state. Under controlled conditions, the resulting current is proportional to the concentration and transport properties of transition metal cations within the slag, and therefore the current is not only a function of the thermodynamic activity. Such a measurement can help to confirm the thermodynamic model used for the OCV measurement as well as provide additional information concerning the transport kinetics and buffering capacity of the slag phase. Furthermore, the use of AC impedance measurements, both independently and in conjunction with an applied DC potential, can be used to yield further information concerning oxidation state ratios for a given transition metal oxide. Additionally, at high frequencies the AC measurement can provide an estimate of the slag conductivity and would be of interest for EAF steelmaking. Amperometric techniques utilizing zirconia membranes have been successful at elevated temperatures for gas sensors[11,12,13,14], diffusion coefficient measurements[15], molten metal refining[16,17,18,19], fuel cells[20], and coulometric titration of oxygen[21,22].

The theory behind AC and DC electrochemical measurement techniques has been covered extensively by several authors[23,24] for analysis of aqueous based electrolyte solutions. However, the theory behind the use of such techniques should not change dramatically for different electrolyte systems such as molten salts or oxide melts. However, surprisingly little work has been done using such measurements on high temperature oxide systems. Electrolysis methods have been utilized with some success for determining cationic transport numbers within oxide melts[25,26] but few investigations focused on these systems as investigators realized that metals could not be produced

easily by direct electrolysis of molten oxides. Measurements by Goto and Schwerdtfeger[27,28] demonstrated the diffusive nature of the rate limitation at a metallic cathode for small applied potentials within oxide melts. Other measurements at lower temperatures for the analysis of glass have been conducted near 1200°C[29,30]. High frequency impedance measurements have been used for determining the bulk slag conductivity[31], however, the use of low frequency impedance to describe the relative concentrations of a given transition oxide species has not been demonstrated in the literature for steelmaking slag compositions. The limited number of measurements made for these systems can probably be attributed to the experimental difficulties associated with the operation of high temperature electrochemical cells which undergo problems with chemical stability of both electrodes and containment vessels. The use of a zirconia electrolyte is important because it will provide a foundation for a stable oxygen reference state, a conductive non-corrosive anode material, and a method for reducing electronic short-circuit conditions for slags containing large quantities of FeOx.

This thesis will provide an initial investigation into the use of amperometric methods in conjunction with a zirconia ion-selective membrane for providing information on the concentration and transport properties of easily dissociable oxides within molten oxide melts. By focusing mainly on demonstrating the ability of such techniques to analyze simple oxide systems containing known concentrations of dissociable oxides, this research will act as a foundation for future investigations interested in the analysis of more complex systems such as those found in the steelmaking process. The thesis will investigate several different amperometric techniques and their applicability to different slag compositions. Oxide melts containing large quantities of dissociable oxides provide

the most difficulty for most amperometric based measurements due to the large currents generated during the measurement which amplify any geometric uncertainties within the cell. A coulometric titration technique was found to work most satisfactorily for such melts and a similar approach might also be utilized for the production of metals without the use of carbon as in conventional steelmaking. Amperometric techniques offer the most interesting analysis for slags containing low concentrations of dissociable oxides. The low currents generated allow for increased sensitivity to the dissociable oxide species and thus a better estimation of the concentration and diffusion coefficients for the relevant cationic species.

The thesis will be organized as follows: Chapter 2 will describe the motivation for an amperometric sensor in more detail. Chapter 3 will characterize both the zirconia and the slag material under investigation. Chapter 4 will provide a background concerning the design of the sensor. Chapter 5 will investigate the ability of amperometric methods to distinguish between low FeOx containing slags with similar oxidation states. Chapter 6 will investigate the use of coulometric titration to yield information concerning slags with high FeOx concentrations. Chapter 7 will draw conclusions on the results discovered in chapter 5 and 6. Finally, Chapter 8 will describe several possible directions in which the work may proceed.

2 Motivation

2.1 Introduction

The fundamental driving force behind developing any slag sensor is to improve steel quality and yield. Metallurgists have known for several decades that proper control of the slag phase is important for attaining a metal phase which is low in oxide inclusions and impurities. This is because the slag acts to insulate the metal from the gas phase and many important reactions are limited at the slag-gas or slag-metal interfaces[32,33,34]. In addition, unwanted impurities from the metal phase are often removed to the slag. Since many slag properties are strongly influenced by the composition of the slag, better processing control could be implemented if the composition of the slag phase was well understood and could be measured more precisely.

The current method for determining the state of the steelmaking system is to take samples of the metal or the slag, and/or use an in-situ oxygen probe. These two techniques will be considered below.

2.2 Sampling Techniques

Sampling techniques have been utilized since the dawn of steelmaking in order to give the steelmaker an idea of what was present in the furnace during different processing steps. Samples are taken from the metal or from the slag and then analyzed in the laboratory. Metal samples can be measured for PPM oxygen content as well as various quantities of alloying additions. Slag samples can be examined by wet chemical

techniques[35] as well as spectroscopic techniques such as Mossbauer[36], Electron paramagnetic resonance (EPR)[37], and spectrophotometry[38] in order to yield both the type of oxide present and the relative concentrations of redox species. While such techniques are quite accurate for determining information on the oxidation state and composition for both the slag and the metal phases, there are two major drawbacks. First, the sample may change chemistry during sampling, removal, quenching, and transport. Therefore, the results may not be a true indication of the state of the system in the actual furnace. This is especially important for slag samples which may demonstrate changes in redox state during quenching due to reactions between different species[39]. Secondly, approximately 30 minutes are required for the laboratory analysis. This is too long to allow feedback of the data for process control. Therefore, a large database exists concerning the slag compositions and oxidation states which are beneficial for making a clean steel. However, the online process control to achieve these parameters is difficult.

2.3 In-Situ Techniques

2.3.1 Conventional Oxygen Sensor

Another method by which steelmakers examine the state of the system is the use of an *in-situ* probe called the conventional oxygen sensor[40] (figure 2.1). This oxygen probe consists of a reference metal/metal oxide mixture contained in an oxygen anion conducting electrolyte such as partially or fully stabilized zirconia. The device is immersed into the steel bath, and a potential is measured between the metal bath and the

reference oxide mixture. This potential can then be related to the oxygen activity in the metal via the Nernst equation (equation 2.1).

$$E = \frac{RT}{2F} \ln\left(\frac{a_{\underline{O}}}{K_{rxn} P_{O_2}^{1/2}}\right) \tag{2.1}$$

where E is the measured Nernst potential, $a_{\underline{O}}$ is the activity of oxygen in the melt, P_{O2} is the reference oxygen pressure, F is the faraday constant, and K_{rxn} is the equilibrium constant for the reaction: $\frac{1}{2}O_2(g) = \underline{O}_{Fe}(wt\%)$.

The activity of oxygen can be related to the PPM oxygen content by knowing the appropriate interaction coefficients for various alloying elements with respect to oxygen. The conventional oxygen sensor has been of invaluable use to steelmakers by allowing real-time measurements of the oxidation state of the metal product. Using the conventional oxygen sensor, metallurgists can determine if the metal is ready for the next processing step or if further additions or blowing operations are required. However, the oxygen sensor is somewhat limited as to the information that can be obtained. The measurement yields only thermodynamic information concerning the oxidation state of the metal phase. No information is gathered on either the buffering capacity of the system to a given oxidation state or on the oxidation state or influence of the slag phase. The buffering capacity is important because it is a measure of the resistance of the system to changes in the oxidation state.

2.3.2 Quik-Slag Sensor

During this thesis investigation, Heraeus Electro-Nite developed an *in-situ* measurement device for the slag phase called the Quik-Slag sensor[41] (figure 2.2). This sensor uses the same OCV technology utilized in the conventional oxygen sensor and attempts to measure the concentration of FeOx within the slag phase. During immersion into the steel, slag is captured at the base of the sensor. Measurement of the OCV, between the iron electrode immersed in the slag and a reference metal/metal oxide phase located within a zirconia oxygen anion conducting membrane, can be used to calculate the activity of FeO (a_{FeO}) within the slag according to equation 2.2.

$$E = \frac{RT}{2F} \ln\left(\frac{a_{FeO}}{K_{rxn} a_{Fe} P_{O_2}^{1/2}} \right) \tag{2.2}$$

where E is the measured potential, a_{FeO} is the activity of FeO in the slag, a_{Fe} is the activity of the iron electrode, P_{O2} is the reference oxygen pressure, and K_{rxn} is the equilibrium constant for the reaction: $FeO_{slag} = Fe + \frac{1}{2} O_2(g)$.

Equation 2.2 assumes that the slag is in equilibrium with the iron electrode of unit activity. Knowledge of the structure of the slag phase can then be used to estimate the concentration of FeOx within the slag from the a_{FeO}. While this device has been tested in industry, it makes the questionable assumption that the slag is in equilibrium with the Fe electrode – this is NOT necessarily a requirement of the system. Secondly, as with the conventional oxygen sensor, the measurement is limited to providing only thermodynamic information concerning the oxygen activity. Therefore, the measurement can yield no information on either the buffering capacity or the kinetics regarding the slag phase.

2.4 Amperometric Improvements

This thesis will describe the use of amperometric techniques to enhance the useful information obtained using conventional OCV measurements. By application of controlled DC potential step and impedance measurements, information concerning the kinetics as well as the thermodynamics of the system can be evaluated. The buffering capacity of the system to a given oxidation state can be revealed by examination of the response to the applied signal. This will be helpful to the steelmaker for determining the quantity of deoxidizer required or the processing time remaining to achieve the desired oxidation state. Furthermore, amperometric techniques allow the investigator to gather insight on the type of oxide material present within the melt. This information is above and beyond the simple oxidation state revealed by OCV measurements. Amperometric measurements do not attempt to replace conventional OCV measurements but are merely expected to enhance the information which can be obtained with these devices.

2.5 Summary

Metallurgists can examine the state of the steelmaking furnace in several ways. Sampling techniques can yield a fairly accurate description of the sampled material but are timely and are not always representative of what actually exists in the furnace. *In-situ* OCV devices yield the oxygen activity of either the slag or the metal phases but are limited to providing ONLY thermodynamic information. This thesis will demonstrate that the use of an amperometric techniques can be used to enhance the information

currently obtained with OCV sensors. Such information includes the knowledge of the concentration of dissociable oxide, type of dissociable oxide, and buffering capacity of the slag to changes in oxidation state. This information will be quite useful for determining the processing time remaining, deoxidizer quantity required, and/or limiting the yield loss of alloying additions to the slag phase.

Figure 2.1 Conventional Oxygen Sensor.

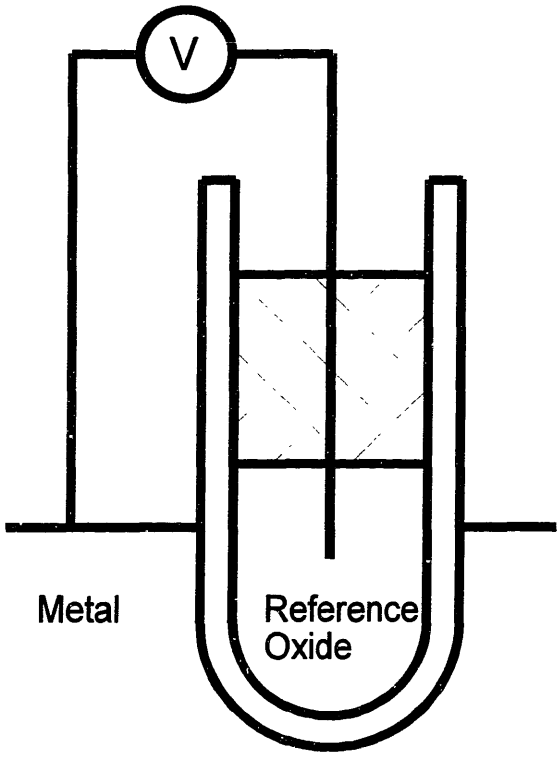

Figure 2.2. Heraeus Electro-Nite Quik-Slag Sensor.

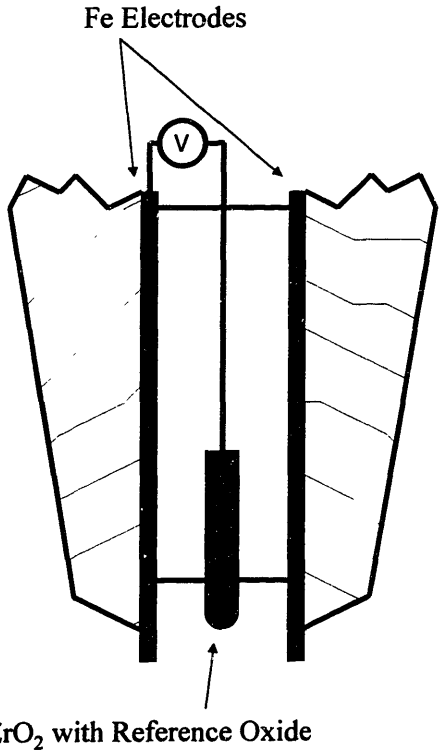

3 Materials Characterization

This thesis is concerned with the behavior and transport properties of two electrolyte materials; the liquid oxide slag electrolyte and the yttria stabilized zirconia solid electrolyte. The slag electrolyte is the phase under investigation. By carefully designing an electrochemical cell and measuring the open circuit voltage and the response to the application of applied potentials and impedance spectroscopy we hope to learn as much as possible about the concentration, structure, and properties of the slag electrolyte phase. The yttria stabilized zirconia solid electrolyte will act as a useful tool for undertaking this task. The zirconia will separate a known reference phase from the slag of interest, enable the removal of oxygen ions from the slag, prevent the passage of electrical current, and protect the anode from oxidation. Complete knowledge of the zirconia phase is therefore important in order to make proper use of this tool for slag phase investigation. In order to have a clear picture as to what the measured responses represent in terms of useful parameters commonly used to describe the slag phase, the slag characterization section will evaluate the important characteristics of oxide melts and provide literature values concerning the slags used in this thesis.

3.1 Zirconia

3.1.1 Introduction

Stabilized zirconia based electrolytes have been utilized for a variety devices and applications because of their unique oxygen ion conducting properties[42,43,44,45]. The following introduction will serve only as a brief summary of the important aspects of the zirconia electrolyte as it pertains to this investigation and should not be considered as an all encompassing summary of this large field of study. For this reason, this section will focus primarily on Y_2O_3 stabilized zirconia.

3.1.2 Background

Pure zirconia demonstrates three solid phase transitions during heating. The monoclinic structure is stable up to 1100°C, the tetragonal structure is stable to 2370°C, and the cubic phase is stable above 2370°C. Solid solutions of pure zirconia with oxide additions such as CaO, MgO, or Y_2O_3 lead to the stabilization of the high temperature cubic structure at lower temperatures. Zirconia containing enough oxide additions to stabilize the cubic structure at room temperature is called fully stabilized zirconia (FSZ). Partially stabilized zirconia (PSZ) contains a lower quantity of oxide additions and consists of tetragonal and/or monoclinic particles within the cubic matrix. PSZ is often used under conditions where thermal stresses or fracture toughness is required because the martensitic transformation of the metastable tetragonal phase to the less dense monoclinic phase helps to blunt crack tips and relieve tensile stresses within the material.

Figure 3.1 demonstrates the phase diagram for Y_2O_3 stabilized zirconia[46]. The addition of the stabilizing oxides also leads to an increase in the number of oxygen anion vacancies within the material as shown in Kroger-Vink notation for Y_2O_3 stabilized zirconia in equation 3.1.

$$Y_2O_3 \overset{ZrO_2}{\rightarrow} 2Y'_{Zr} + 3O_O^X + V_O^{\bullet\bullet} \tag{3.1}$$

The high concentration of oxygen vacancies in the fluorite crystal structure ensures that the oxygen vacancy is the predominant ionic charge carrier within the material. The total conductivity of the zirconia is related to all of its defect concentrations by the following equation 3.2.

$$\sigma_{tot} = \sum_i c_i q_i \mu_i + n q_e \mu_e + p q_h \mu_h = \sum_i \sigma_i + \sigma_e + \sigma_h \tag{3.2}$$

where σ_{tot} is the measured conductivity of the Zirconia (1/(Ω-cm)), c_i is the concentration of ionic defects such as interstitials or vacancies (mole/cm^3), p is the concentration of holes (mole/cm^3), n is the concentration of electrons (mole/cm^3), q is the charge of the species, μ is the mobility of the species within the material (cm^2/V-sec), σ_x is the partial conductivity of YSZ due to charge carrier x. The relative impact of each species on the overall conductivity is usually described by means of the transference number as defined in equation 3.3.

$$\sigma_x = t_x \sigma_{tot} \tag{3.3}$$

where t is the transference number and ranges from 0 to 1. Mainly because of their smaller mass, the mobility of electrons and holes is orders of magnitude greater than that of the ionic defects. However, when the zirconia structure is fully stabilized, the conductivity is determined mainly by the mobility of the oxygen ion vacancies because of

their overwhelming concentration over that of the mobile holes and electrons. Thus the transference number associated with the motion of oxygen vacancies is very close to one under most conditions.

Changes in the oxygen partial pressure can influence the concentration of electrons and holes within the zirconia thereby altering the predominant mode of conduction through the material. Most applications of stabilized zirconia rely upon the purely ionic conduction properties of the zirconia to function accurately and/or efficiently. A significant amount of conduction due to holes or electrons lead to problems in the application of zirconia for sensors and/or deoxidation processes. For this reason Patterson[47] has described the various conduction domains for solid electrolytes as defined by the parameters P_θ and σ_{ion}. At large oxygen pressures, atomic oxygen enters into the ZrO_2 lattice forming oxygen interstitials and holes via equation 3.4.

$$\tfrac{1}{2}O_2(g) = O_i'' + 2h^{\bullet} \tag{3.4}$$

The partial conductivity of the zirconia due to holes is expected to increase with the partial pressure of oxygen as shown in equation 3.5 assuming that the concentration of oxygen interstitials is independent of oxygen partial pressure.

$$\sigma_p = \sigma_p^0 P_{O_2}^{1/4} \tag{3.5}$$

At small oxygen pressures additional oxygen vacancies are created which are charge balanced by the formation of electrons as shown in equation 3.6.

$$O_O^X = \tfrac{1}{2}O_2(g) + V_O^{\bullet\bullet} + 2e' \tag{3.6}$$

The partial conductivity of the zirconia due to electrons is expected to increase with decreasing partial pressure of oxygen as shown in equation 3.7 assuming that the concentration of oxygen vacancies is independent of oxygen partial pressure.

$$\sigma_e = \sigma_e^0 P_{O_2}^{-1/4} \tag{3.7}$$

The increase in the concentration of electrons or holes without a significant increase in the concentration of oxygen vacancies leads to an increase in the overall conductivity of the material but a decrease in the transference number of oxygen vacancies. Therefore at both very high and very low oxygen partial pressures, the electrolyte may become an electronic or mixed conductor as opposed to a purely ionic conductor. The partial electronic conductivity is often characterized by the parameter P_Θ which is defined as the oxygen partial pressure at which the electronic and ionic partial conductivity's are identical ($t_{O2-}=t_e=0.5$). If P_θ and σ_{ion} are known, then the electronic conductivity can be defined at any oxygen partial pressure as shown by equation 3.8 and 3.9.

$$\sigma_{ion} = \sigma_e^0 P_\theta^{-1/4} \Rightarrow \sigma_e^0 = \sigma_{ion} P_\theta^{1/4} \tag{3.8}$$

$$\sigma_e = \sigma_{ion}\left(\frac{P_\theta}{P_{O_2}}\right)^{1/4} \tag{3.9}$$

3.1.3 Zirconia Thermodynamic Measurements

The predominantly oxygen anion conduction mechanism of stabilized zirconia makes it a useful material for measurement of oxygen activity using a galvanic cell. Wagner[48] derived equation 3.10 which describes the relationship between the open circuit potential (electromotive force) and the chemical potential at each electrode.

$$E = \frac{-1}{|n_i|F}\int_{\mu_i''}^{\mu_i'} t_{ion}\, d\mu_i \tag{3.10}$$

where i is the ion of interest, n is the valance, F is the faraday constant, t_{ion} is the total ionic transference number, and μ is the chemical potential at each electrode.

The above equation simplifies to the following Nernst equation when the ionic transference number (t_{ion}) approaches 1.

$$E = \frac{RT}{4F} \ln\left(\frac{P'_{O_2}}{P''_{O_2}}\right) \tag{3.11}$$

If there is mixed electronic and ionic conduction, Schmaltzried[49] demonstrated that the open circuit voltage would be given by equation 3.12.

$$E = \frac{RT}{F}\left[\ln\left(\frac{P_\theta^{1/4} + P_{//}^{1/4}}{P_\theta^{1/4} + P_{/}^{1/4}}\right) + \ln\left(\frac{P_{\theta_h}^{1/4} + P_{/}^{1/4}}{P_{\theta_h}^{1/4} + P_{//}^{1/4}}\right)\right] \tag{3.12}$$

where P_θ is the partial pressure of oxygen at which $\sigma_{ion}=\sigma_e$, P_{θ_h} is the partial pressure of oxygen at which $\sigma_{ion}=\sigma_{hole}$, $P_{/}$ is the partial pressure of oxygen at the reference electrode, $P_{//}$ is the partial pressure of oxygen at the working electrode.

3.1.4 Zirconia Characterization

A sound knowledge of the electronic properties of the zirconia electrolyte as a function of temperature and oxygen partial pressure are very important to the successful implementation of the electrochemical techniques described within this thesis. While literature data exists on the ionic conductivity and P_θ values for many different compositions of zirconia electrolytes[50,51,52], high temperature measurements are rare for the specific yttria PSZ composition used in this thesis and the scatter among investigators concerning the P_θ value is somewhat large[51]. The scatter is due to reasons ranging from

differences in material structure and composition to improper experimental measurement techniques[53]. Measurement of the ionic conductivity and P_θ values for the two zirconia electrolytes used within the thesis were measured and compared with other values found in the literature.

The zirconia utilized in this thesis consisted of Coors ZDY-4 and ZDY-9 8wt% (4mole%) yttria partially stabilized zirconia tubes. Both tubes contained the same concentration of stabilizer but the ZDY-4 was of lower overall purity (and lower cost). The following measurements were carried out to fully characterize both materials: 4 probe DC technique for determination of ionic conductivity, Swinkels Coulometric technique[54] for determination of P_θ, SEM microprobe analysis for grain size and structure, and XRD for zirconia phase determination.

3.1.4.1 Ionic Conductivity

3.1.4.1.1 Experimental

A four-probe DC technique[55] (figure 3.2) was used to determine the ionic conductivity of both the ZDY-4 and ZDY-9 compositions in air as a function of temperature. The four-probe technique is superior to a simple two electrode technique for the measurement of ionic conduction because the current carrying electrodes may polarize. Each of the four electrodes consisted of a 0.02" diameter Pt wire and were applied to the zirconia using Engelhard Platinum ink #6926. Using a 1287 Solartron potentiostat, a current was passed through the outer two electrodes (WE and CE) while the potential was measured between the inner two electrodes (RE2 and RE1). Applied

potential sweeps (RE2 vs RE1) were used instead of potential steps in order to ensure that the measured resistance was not a function of the applied current. The system temperature was monitored using an S-type T/C. Ionic conductivity measurements were taken at approximately 50°C increments from 1200 to 1700°C. The ionic conductivity was calculated using equation 3.13.

$$\sigma_i = \frac{i_{app}}{V_{meas}} \frac{d}{A} \tag{3.13}$$

where $A = \pi\left(r_{OD}^2 - r_{ID}^2\right)$ is the cross-sectional area of the zirconia tube, d is the distance between the RE2 and RE1 electrodes, V_{meas} is the voltage measured between the RE2 and RE1 electrodes, and i_{app} is the current applied between the WE and CE electrodes.

3.1.4.1.2 Results

The relationship between ionic conductivity and temperature for the ZDY-4 and ZDY-9 electrolytes is shown in figure 3.3 and was described by equation 3.14[56].

$$\sigma_i = \frac{C_i}{T} \exp\left(\frac{-E_i}{kT}\right) \tag{3.14}$$

ZDY-4 (1200-1500°C): $C_i = 1.27 \times 10^6$, $E_i = 1.066$ eV

ZDY-4 (1500-1700°C); $C_i = 2.25 \times 10^5$, $E_i = 0.8$ eV

ZDY-9 (1200-1700°C); $C_i = 8.95 \times 10^6$, $E_i = 1.002$ eV

where C_i and E_i are fitting coefficients with E_i representing the activation energy for ionic motion, k is the Boltzman constant, and T is the temperature in K. The conductivity of the ZDY-9 was consistently higher than the ZDY-4 over the entire temperature range. The ZDY-4 sample demonstrated a shift in the appropriate C_i and E_i values at a temperature of approximately 1773K. The ionic conductivity did not vary as a function

of applied current ensuring that no polarization or irregular current paths were influencing the measurement.

3.1.4.2 Electronic Conductivity

3.1.4.2.1 Experimental

A modified Swinkels coulometric titration technique[54] was utilized to determine the parameter P_θ for the ZDY-4 and ZDY-9 zirconia electrolytes. The Swinkels technique avoids many of the experimental complications realized in other techniques such as permeation, blocking electrode, or EMF methods with known gas compositions. The experimental setup is shown in figure 3.4 and consists of driving current though the following cell to reduce the partial pressure of oxygen in the Ag near the electrolyte to a very low value. Equation 3.15 describes the electrochemical cell.

$$Mo / Ag(\underline{O}) / ZrO_2 + 4wt\%Y_2O_3 / O_2(0.21atm), Pt \qquad (3.15)$$

The WE and RE2 electrodes were constructed of 0.02 inch diameter Mo wires and were dipped into the Ag prior to the measurement. The Ag was shielded with argon gas at a flow rate of 15 ml/min. Platinum WE and RE2 electrodes could not be used because of their rapid dissolution into the Ag melt. The CE and RE1 electrodes were made from 0.02 inch diameter platinum wires and were attached to the zirconia using Engelhard 6926 platinum ink and were located in a chamber containing air as a reversible reference electrode. The temperature was measured at the counter electrode using a type S thermocouple. Measurements for the P_θ value were taken at approximately 50°C increments from 1200°C to 1650°C. A Solartron 1287 potentiostat was used to apply a

potential sweep between the RE2 and RE1 electrodes by driving a current between the CE and WE electrodes until a current of approximately 1 ampere was achieved at which point the applied current was cut off. At this point the oxygen partial pressure in the silver near the zirconia was sufficiently low such that equation 3.16 was valid.

$$P_{O_2}(Ag) << P_\theta \tag{3.16}$$

The resulting open circuit potential between the CE and WE electrodes was recorded using a Tektronix digital oscilloscope at 100 microseconds after cut-off. The measured potential was corrected for the thermoelectromotive force between the Mo-Pt wires using data by Iwase[53] which was also confirmed by our own measurements to be given by equation 3.17.

$$E_t(Mo+, Pt-, mV) = -22.1 + 0.04T \tag{3.17}$$

The corrected potential was then related to the P_θ value using equation 3.18, a modified version of equation 3.12 which is valid only for very short times after the current cut-off.

$$E = \frac{RT}{F}\ln\left(\frac{P_\theta^{1/4}}{P_I^{1/4}}\right) \tag{3.18}$$

3.1.4.2.2 Results

The relationship between the P_θ value and temperature for the ZDY-4 and ZDY-9 samples is shown in figure 3.5. Linear regression analysis was used to fit the data to equation 3.19.

$$\log(P_\theta) = \frac{A}{T} + B \tag{3.19}$$

ZDY-4: A = -85400, B = 30.985

ZDY-9: A = -82800, B = 28.746

The ZDY-4 zirconia demonstrated slightly lower P_θ values than the ZDY-9 zirconia. Using the ionic conductivity data, the electronic conductivity can be determined as a function of temperature and partial pressure of oxygen using equation 3.9.

3.1.4.3 Microstructure Characterization

3.1.4.3.1 X-ray Characterization

The ZDY-4 and ZDY-9 electrolytes were examined using X-ray spectroscopy in order to determine the phases present at room temperature. PSZ would be expected to demonstrate tetragonal and cubic phases at room temperature. The existence of large quantities of monoclinic zirconia could lead to short circuit electronic conduction within the zirconia and would be undesirable. 4 mole% yttria PSZ has been examined previously using XRD[57] in order to determine the types of phases present at room temperature after various high temperature annealing processes. The XRD patterns for the ZDY samples are shown in figure 3.6 and have been smoothed using the appropriate correction procedures to eliminate background noise, Lorentz polarization, and absorption effects. The XRD patterns demonstrated the existence of cubic and tetragonal phases in the material while the presence of monoclinic zirconia was minimal.

3.1.4.3.2 SEM Microprobe Characterization

The ZDY-4 and ZDY-9 electrolytes were examined using a JOEL SEM microprobe to determine the composition of the binder, the grain size, and porosity. A portion of each of the tubes was sectioned, mounted in epoxy, and then carbon coated. SEM micrographs of the ZDY samples can be found in figures 3.7a-b. Table 1 describes

the range of grain size, porosity, and binder composition for each sample. The ZDY-9 sample did not contain a binder phase at the grain boundary and hence the approximate grain size was difficult to estimate without etching the grain boundaries. The binder phase of the ZDY-4 sample was analyzed using the SEM microprobe to be of the following composition: 20 wt%CaO, 25 wt%Al_2O_3, 45 wt%SiO_2, balance 10 wt%(ZrO_2+Y_2O_3). The melting point of this phase was estimated from the CaO-Al_2O_3-SiO_2 phase diagram to be approximately 1450-1500°C.

3.1.4.4 Summary and Conclusions

The ionic conductivity and P_θ values were determined for the 4 mole% (8wt%) Y_2O_3 PSZ ZDY-4 and ZDY-9 Coors samples used in this thesis. The values do not differ much from each other and correspond well with previously determined literature data. The main difference between the ZDY-4 and ZDY-9 is the existence of the CaO-Al_2O_3-SiO_2 binder phase. Grain boundary phases have been shown to influence the properties of bulk zirconia[58]. At high temperatures (>1500°C) the binder phase most likely becomes liquid causing a shift in the ionic conductivity curve for the ZDY-4 zirconia. Also, because the binder phase is a predominantly ionic conductor over all ranges of oxygen partial pressure, it might influence the measured P_θ values of the bulk material. If the binder phase is located in series with conduction in the zirconia electrolyte it would be expected to lower the effective P_θ value measured for the bulk material. This would explain the slightly lower P_θ values obtained for the ZDY-4 vs ZDY-9 samples.

Table 3.1 Results of SEM analysis of ZDY-4 and ZDY-9.

	Grain Size μm	Pore Size μm	Binder Composition wt%
ZDY-4	10-20	5	None
ZDY-9	10-30	5-10	20%CaO-25%Al_2O_3-45%SiO_2

Figure 3.1 Y_2O_3 stabilized ZrO_2 phase diagram[46].

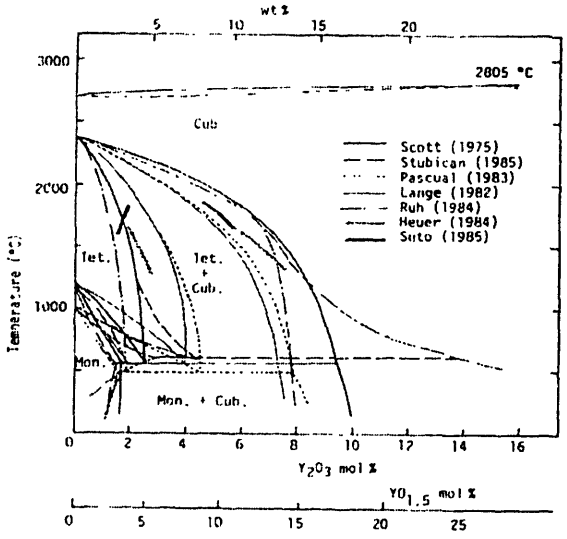

Figure 3.2 4-Probe DC technique[55] for ionic conductivity measurement. DC potential sweep applied to the outside leads and the potential is measured across the inside leads.

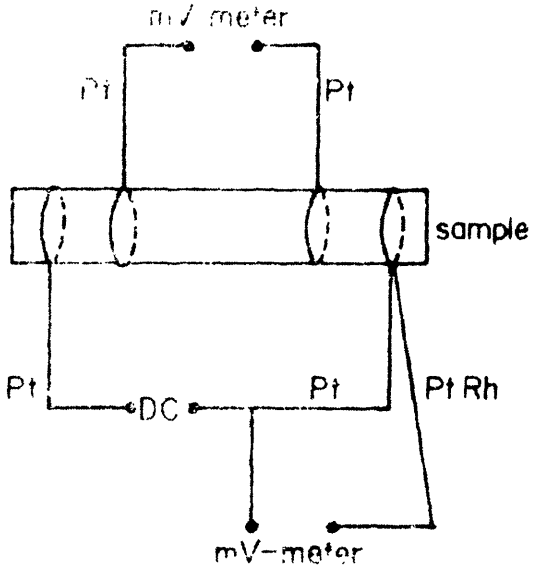

Figure 3.3 Results of the ionic conductivity experiments for the Coors ZDY-4 and ZDY-9 tubes used in this thesis.

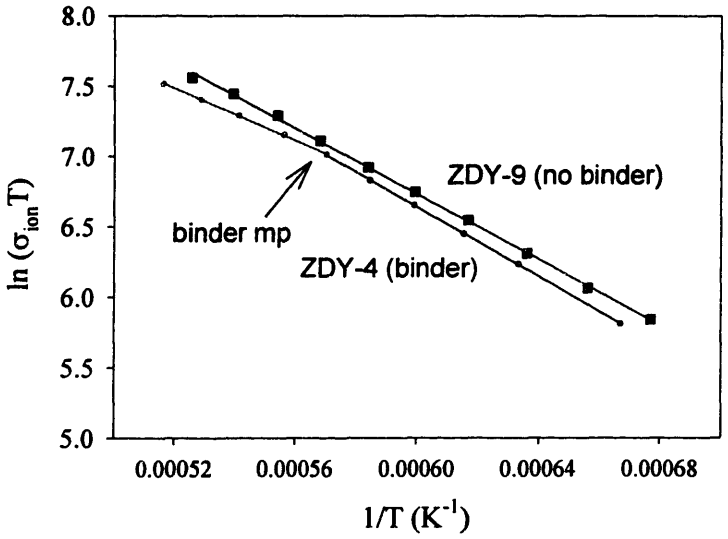

Figure 3.4 Experimental setup for the P_{Θ} measurements.

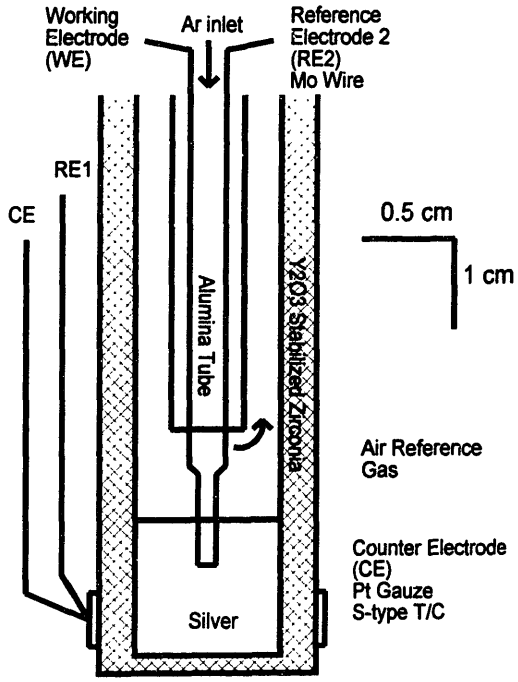

Figure 3.5 Results of the P_θ measurements for Coors ZDY-4 and ZDY-9 zirconia tubes.

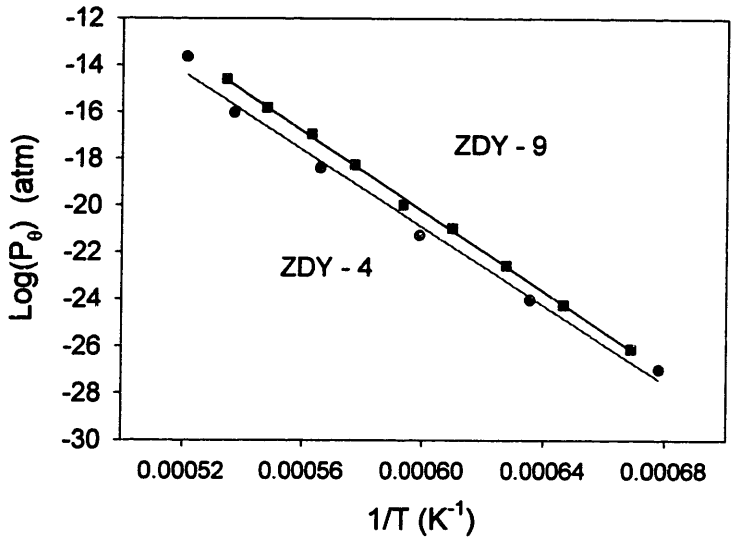

Figure 3.6 XRD pattern for the Coors ZDY-4 zirconia tube.

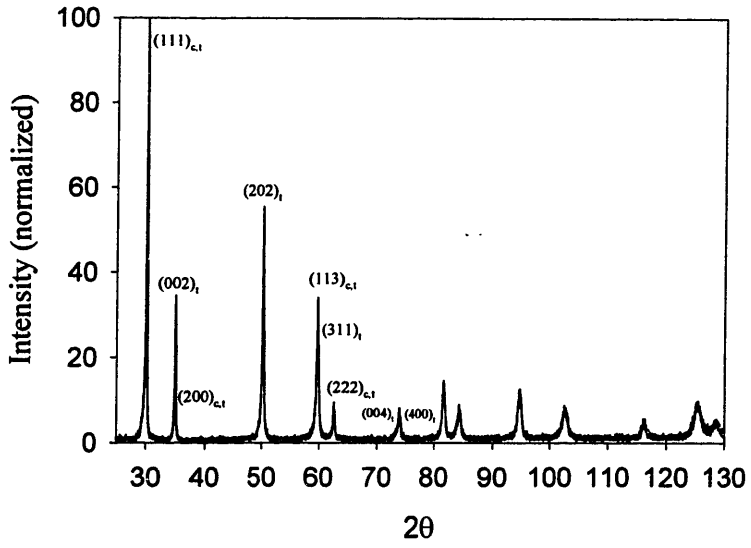

Figure 3.7a SEM photograph of Coors ZDY-4.

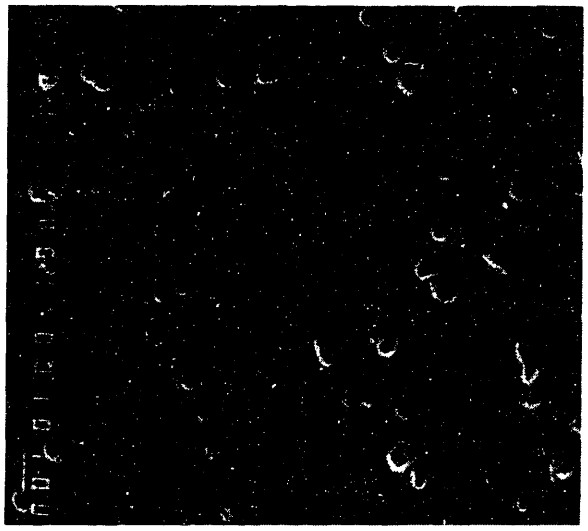

Figure 3.7b SEM photograph of Coors ZDY-9.

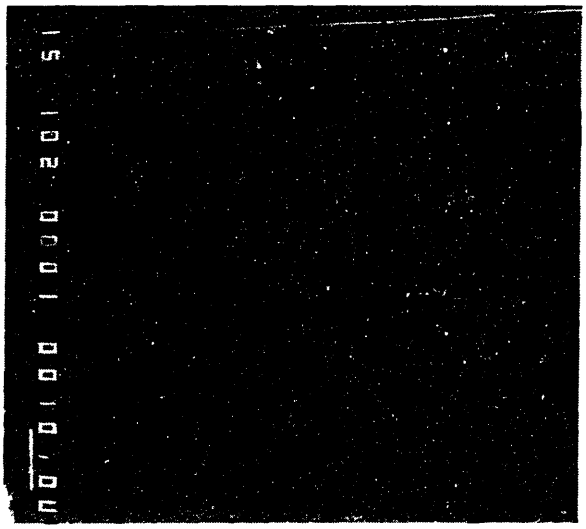

3.2 Slag

3.2.1 Introduction

A molten oxide slag is a very complex material that can demonstrate a wide range of properties depending upon its underlying composition. Knowledge of how the various properties of a slag phase are influenced by its composition will be important in evaluating the responses measured by the amperometric sensor. For this reason, the preparation and composition of the slags investigated in this thesis are described in the first section. Following sections then provide both a description and an estimation of the following important properties as they pertain to these slags: structure, conductivity, transport properties, and thermodynamics. Table 3.2 contains a complete summary of the values obtained for each of the slags.

3.2.2 Slags Investigated

3.2.2.1 Composition

The slag compositions were separated into two groups, those containing a high FeOx concentration (>10wt%) and those containing a low FeOx concentration (<10wt%). Within each group the CaO-Al_2O_3-SiO_2 ratios were held constant while the FeOx content was varied. The slag compositions are described in detail in equations 3.20-3.22.

High FeOx concentration:

Aus slags:

$$(0.37CaO - 0.63SiO_2)_{100-z}(Fe_2O_3)_z \qquad z = \{20,30,40\} \qquad (3.20)$$

Low FeOx concentration:

H slags:

$$(0.39CaO - 0.48SiO_2 - 0.13Al_2O_3)_{100-z}[Fe_2O_3]_z \qquad z = \{0,0.5,1,2,4\} \qquad (3.21)$$

L slags:

$$(0.48CaO - 0.39SiO_2 - 0.13Al_2O_3)_{100-z}[Fe_2O_3]_z \qquad z = \{0,1,2,4\} \qquad (3.22)$$

The phase diagrams representing the CaO-SiO_2-FeOx and Al_2O_3-CaO-SiO_2-FeOx slag systems[59,60,61] can be found in figures 3.8-3.10. The slag compositions were intentionally chosen such that the melting points were located below 1450°C. From literature data[62], the density of the H and L slags were estimated to be approximately 2.56 and 2.624 g/cm^3 respectively.

3.2.2.1.1 Preparation

Slags of the desired compositions were obtained by the following procedure. An oxide mixture of CaO (Alpha-Aesar 99%), SiO_2 (Alpha-Aesar 99.5%), Al_2O_3 (Alpha-Aesar 99.5%), and Fe_2O_3 (Alpha-Aesar 99%) powders was mixed in the applicable ratio for each slag composition. The SiO_2, Al_2O_3, and Fe_2O_3 powders were preheated at 200°C for two days in order to remove any absorbed water vapor. The CaO was pre-calcined at 1000°C for 6 hours in order to remove any $CaCO_3$. The oxide powders were thoroughly mixed for 24 hours on a ball mill using isopropyl alcohol and Al_2O_3 milling media. The mixture was dried under argon, pressed at 5000psi, sintered at 1000°C for 6 hours, and then recrushed to provide a feed material for the experiment.

3.2.3 Slag Structure

Molten slags consist of three types of oxides; basic, acidic, and amphoteric. Basic oxides (CaO, FeO, MgO etc.) donate O^{2-} to the oxide melt as well as free cationic species as given by equation 3.23.

$$CaO \rightarrow Ca^{2+}_{slag} + O^{2-}_{slag} \tag{3.23}$$

Free cationic species have been shown to be the main charge carriers in oxide melts as will be described in more detail in the conductivity section. Acidic oxides (SiO_2) consume O^{2-} from the melt and form complex anionic species as given by equation 3.24.

$$2O^{2-}_{slag} + SiO_2 \rightarrow SiO^{4-}_{4,slag} \tag{3.24}$$

Formation of complex anionic species increases the slag viscosity and reduces slag conductivity. Amphoteric oxides (Al_2O_3) behave as acidic oxides under basic conditions and as basic oxides under acidic conditions. Therefore, the impact of amphoteric oxides on slag properties will change depending upon the underlying slag structure. Depending upon the ratio of acidic and basic oxides, the slag will demonstrate very different properties. In order to compare the slags investigated in this thesis with results obtained by other investigators for similar slag structures, two measures of basicity commonly used in the literature[63] are shown in equations 3.25 and 3.26.

$$B = \frac{X_{CaO}}{X_{SiO_2}} \tag{3.25}$$

$$B_{Al_2O_3} = \frac{X_{CaO}}{X_{SiO_2} + X_{Al_2O_3}} \tag{3.26}$$

The basicity values for slags in this thesis ranged from 0.6 to 1.1 indicating significant anionic polymerization within the slag structure. Most slags for steelmaking are quite basic with low SiO_2 content demonstrating basicity values larger than 1. Acidic slags with low basicity values are investigated in this thesis in order to prevent rapid dissolution of the zirconia electrolyte.

The structure of polymeric melts is an extremely complex field and researchers are still not capable of fully understanding all of the phenomena involved with melts containing several oxide species. Further discussion on the structure of slags can be found in the following references and should be referred to for supplementary information[64,65,66,67].

3.2.4 Conductivity and Diffusivity Values

3.2.4.1 Background and Theory

The conductivity of any medium is a strong function of its underlying structure. Electric current in slags can be conducted by the migration of cations, anions, electrons, or holes contained within the melt. The overall slag conductivity is defined as a sum of the partial conductivities of each of the migrating species as shown in equation 3.27.

$$\sigma_{tot} = \sum_i \sigma_i^+ + \sum_i \sigma_i^- + \sigma_e + \sigma_h \tag{3.27}$$

The relative contribution of each of these species to the overall conductivity is described by its transference number (t_i).

$$t_i = \frac{\sigma_i}{\sigma_{tot}} \tag{3.28}$$

The transference number for electrons or holes is generally quite small except for slags containing large quantities of transition metals such as iron, nickel, copper, or zinc[68]. Therefore most slags are predominantly ionic conductors. Ionic conductivity is related to charge, mobility, and concentration.

$$\sigma_i = Fz_i u_i C_i \tag{3.29}$$

The transport number for anionic species in molten silicate slags is considered to be negligible because of the large radii associated with the covalently bonded anionic network. Therefore most slags are cationic conductors. The fast diffusivity values resulting from the relatively small size of basic cations (Fe^{2+}, Ca^{2+}, Mg^{2+}, etc.) largely determine the conductivity of the overall melt. The Nernst-Einstein equation attempts to describe this relationship between ionic self-diffusivity and partial conductivity.

$$\sigma_i = \frac{Ne^2 Z_i^2 C_i D_i}{kTf} \tag{3.30}$$

where D is the self diffusivity cm^2/sec, N is Avagadros number, e the electronic charge $1.6x10^{-19}$ A-sec, Z_i the valence, C_i the concentration (mol/cm^3), and f is the correlation factor.

Goto demonstrated that the complex silicate anion structure significantly lowers the value of the correlation factor[69,70] applicable for silicate melts. Note that for a given slag structure (f=constant) the transport number for cationic species within the melt can be estimated by knowing the relative concentrations and diffusivity values for each of the relevant ionic species.

$$t_i = \frac{c_i D_i}{\sum_j c_j D_j} \tag{3.31}$$

where j consists of Fe^{2+}, Fe^{3+}, and Ca^{2+} ions (the D value for Si^{4+}, Al^{3+}, or O^{2-} ions is assumed to be negligible).

However, diffusivity data for molten slags are not readily available and have typical experimental errors on the order of 20-30% or more. While typical values for acidic "cations" (Si^{4+}, Al^{3+}) are around $1x10^{-7}$ to $1x10^{-6}$ cm^2/sec, typical values for basic cation species range from $1x10^{-6}$ to $1x10^{-4}$ cm^2/sec depending upon the ion, slag structure, and temperature[66].

Because the mechanism of slag conductivity is related to the motion of ionic species it is expressed by an Arrhenius relationship:

$$\sigma = A\exp\left(\frac{-E_\sigma}{RT}\right) \tag{3.32}$$

where σ is the electrical conductivity in (Ω^{-1}-cm^{-1}), R is the gas constant 8.314 J/mole-K, E is the activation energy J/mole, and A is a constant.

For silicate melts the activation energy is only valid over small temperature ranges because the complex anionic structure is ionized with increasing temperature reducing slag viscosity and increasing the apparent conductivity and diffusivity.

3.2.4.2 Relevant Literature values

Measurements of the conductivity of a molten slag can be accomplished by utilizing electrochemical setups[71] found in figure 3.11 and by utilizing AC techniques to eliminate polarization effects. By properly standardizing the cell geometry accurate values for slag conductivity can be obtained. Conductivity values for a wide range of slag compositions are available in the literature[71]. The following sections focus on

conductivity and diffusivity values in the literature for slags containing FeOx in order to develop a background for the slags investigated in this thesis.

3.2.4.2.1 Conductivity of FeOx containing slags

The conductivity of slags containing FeOx will be dependent upon a number of different factors as described earlier. In general, the slag conductivity will increase with FeOx concentration, temperature, and slag basicity. Jiao and Themelis[72] have extensively reviewed the experimental literature on ferrous and nonferrous metallurgical slags and expressed the slag conductivity as an exponential function of the molar fractions of FeO, CaO, and MgO for a wide range of industrial slags. At 1500°C the following correlation was found:

$$\ln\sigma = -4.45 + 9.15X_{FeO} + 5.34\left(X_{CaO} + X_{MgO}\right) \tag{3.33}$$

and at 1400°C

$$\ln\sigma = -5.21 + 9.92X_{FeO} + 5.94\left(X_{CaO} + X_{MgO}\right) \tag{3.34}$$

Jiao and Themelis[72] also summarized the influence of FeOx on the relative transport number of electronic and ionic conduction mechanisms. As described earlier, the addition of transition metals to a slag may lead to predominant electronic conduction mechanisms. They found that slags containing less than 20wt% FeOx demonstrated negligible electronic conductivity whereas slags with greater iron oxide contents demonstrated electronic conduction which increased with the oxygen partial pressure or Fe^{3+}/Fe^{2+} ratio (figure 3.12)[72]. For FeOx concentrations between 10 and 30 wt% they found that the conductivity did not change dramatically over the Fe^{3+}/Fe_{Tot} range from 0 to 0.5. This would appear to indicate that the equivalent ionic transport number is

approximately identical for Fe^{2+} and Fe^{3+} species in this range. However, for slags containing lower total iron concentrations, Engell and Vygen observed a decrease in ionic conductivity with increasing oxygen partial pressure indicating Fe^{2+} species may be more mobile than Fe^{3+} species[73] (figure 3.13).

3.2.4.2.2 Tracer Diffusivity Values of Cationic Species

Limited tracer diffusivity values are available for different cationic species in the literature. However, disparities are often seen in the values of diffusion coefficients in independently carried out experiments. Tracer diffusivities in the literature for the same ion in identical slags may differ by almost one order of magnitude[74]. In agreement with equations 3.33 and 3.34, the tracer diffusivity of Ca^{2+} is smaller than Fe^{X+} indicating that the influence of Ca^{2+} on the total slag conductivity is not nearly as strong as that of Fe^{X+} per unit of concentration. Schwerdtfeger et al.[75,76] used both electrochemical and porous frit techniques to determine that the self diffusion coefficients of Fe^{2+} and Ca^{2+} at 1600°C for SiO_2 saturated slags were approximately 1-3x10^{-5} cm^2/sec and 1-2x10^{-6} cm^2/sec respectively. Schwerdtfeger also demonstrated that the diffusivities remained largely independent of composition up to approximately 15 wt%FeOx as might be expected because the overall slag structure should remain largely unchanged in the Henrian regime. Goto[77] found that the tracer diffusivity for Fe^{X+} (~3x10^{-5} cm^2/sec) was approximately 3 times greater than that for Ca^{2+} ions for 33CaO-27SiO_2-40Fe_2O_3 slags between 1300-1450°C. A review article by Nagata and Goto[78] compared the diffusivity values measured for a wide variety of blast furnace and steelmaking slags over the temperature range 1300-1600°C. The data can be found in figures 3.14 and 3.15 where

the diffusivity for Fe^{X+} appears centered near $1x10^{-5}$ cm^2/sec for acidic oxide melts near 1500°C.

The mechanism for the higher diffusivity of iron cations as compared with calcium cations is not clear – it cannot be simply explained by the difference in their respective radii (equations 3.35a and 3.35b) as others have assumed improperly in the literature[79] by using Waldens rule.

$$t_{Fe} = \frac{\alpha X_{FeO}}{\alpha X_{FeO} + X_{CaO}} \tag{3.35a}$$

$$\alpha = \frac{r_{Ca}}{r_{Fe}} = \frac{0.99}{0.74} = 1.34 \tag{3.35b}$$

Calculations of the respective diffusivity values obtained by using equation 3.35b would indicate that their diffusivities should differ by a factor of 1.34 as opposed to the 3-10 times reported from tracer diffusivity and conductivity experiments. Nowack[75] proposed that the 3d orbital of the Fe^{2+} ion allows it to achieve a transition state with the anionic network which Ca^{2+} is unable to form. However, a conclusive mechanism has not yet been established.

Another factor which may influence the diffusivity of Fe^{X+} species is the oxygen partial pressure. The influence of oxygen partial pressure on the self-diffusivity and conductivity of iron is somewhat misleading. While Engell and Vygen[73] observed a decrease in conductivity with increasing P_{O2}, Jiao and Themilis[72] did not observe any change, and Goto et al.[77] (figure 3.16) demonstrated that diffusivities of both Ca^{2+} and Fe^{x+} increased with oxygen partial pressure. The oxygen partial pressure would influence the ratio of Fe^{3+}/Fe^{2+} species in the slag. The most likely explanation is that the total iron concentration is important in providing an electronic short circuit that might assist ionic

transport. Since some Fe^{3+} species will likely be located in network forming tetrahedral sites[80], the calculated self-diffusivity of Fe^{3+} might be expected to be lower than for Fe^{2+} for FeOx containing melts simply because of the fraction of immobile ions associated with the network. However, because of the mixed valency of the Fe species in a slag, tracer diffusion data cannot easily determine the relative diffusivity values for each of the Fe species, and the apparent diffusivity of a Fe^{3+} species may be more mobile because of its semi-conductive properties.

In summary, values for the diffusivity of Fe in molten oxides vary widely with slag structure but are typically in the range of $1x10^{-5}$ cm^2/sec for acidic slags near 1500°C.

3.2.4.3 Estimating Values of Conductivity and Diffusivity

3.2.4.3.1 Low concentration slags (H, L)

Values of conductivity for the two 0 wt%FeOx slags, H0 and L0, are reported in the Slag Atlas[81]. Values for A and E in equation 3.32 are shown in equations 3.36a, b.

$$H0: \ A = 7943, E = 161950 \tag{3.36a}$$

$$L0: \ A = 4508, E = 147380 \tag{3.36b}$$

The conductivities for the H and L slags containing iron oxide were estimated using two different methods:

1. Jiao and Themilis regression data
2. Nernst-Einstein relation to transform self-diffusivity data into partial conductivity data.

3.2.4.3.1.1 Jiao and Themilis Method

Using Jiao and Themilis[72] regression data (equations 3.33 and 3.34) slag conductivities were estimated at 1400°C and 1500°C. Intermediate temperatures were then approximated by assuming the Arrenhius relationship in equation 3.32 between the two temperatures as follows shown in equations 3.37a, b.

$$E = \frac{\ln\left(\frac{\sigma_{1400C}}{\sigma_{1500C}}\right)}{\left(\frac{1}{R(1773)} - \frac{1}{R(1673)}\right)} \tag{3.37a}$$

$$A = \frac{\sigma_{1400C}}{\exp\left(\frac{-E}{R(1673)}\right)} \tag{3.37b}$$

The conductivity values derived from the Jiao and Themilis regression data agreed fairly well with the zero FeOx conductivity data reported in the slag atlas[81] (error approx. 10-20%). The use of values predicted by Jiao and Themilis are somewhat questionable for the H and L slag compositions because they lie outside the range of those measured in the original regression paper. However, their use can be justified because the relationship is fundamentally based upon the motion of the mobile cationic species.

The transport number for Fe cations for each slag composition can be estimated using equation 3.38 under the assumption that the slag conductivity for 0wt%Fe is entirely due to Ca^{2+} and that the addition of small quantities of FeOx does NOT dramatically change the underlying slag composition.

$$t_{Fe} = 1 - \frac{\sigma_{base}}{\sigma_{Fe}} \tag{3.38}$$

3.2.4.3.1.2 Estimation from Diffusivity data

From the above discussion the diffusivity of Fe^{2+} can be assumed to be approximately six times greater than the diffusivity of Ca^{2+}. Using this assumption the transference number for iron cations was computed from equation 3.39.

$$t_{Fe} = \frac{X_{Fe}D_{Fe}}{X_{Fe}D_{Fe} + X_{Ca}D_{Ca}} = \frac{X_{Fe}D_{ord}}{X_{Fe}D_{ord} + X_{Ca}} \tag{3.39}$$

where D_{ord} is the diffusion coefficient ratio (6) of Fe^{2+} to Ca^{2+}. The conductivity of the slag at various iron oxide compositions was then estimated by applying equation 3.38 using the 0 wt%Fe slag and the result from equation 3.39.

3.2.4.3.1.3 Summary: Low Concentration Slags

The estimated and literature values for the H and L slags described above are summarized in Table 3.2. In general the conductivity of the L slags are approximately twice that of the H slags for most temperatures. This corresponds well with the estimated slag viscosities for temperatures between 1400 and 1500°C (figures 3.17a,b)[82]. Assuming the validity of the Stokes-Einstein relationship (equation 3.40)

$$D_i = \frac{kT}{6\pi r_i \eta}\left(\frac{\delta \ln a_i}{\delta \ln c_i}\right) \approx \frac{kT}{6\pi r_i \eta} \tag{3.40}$$

the diffusion coefficient for a given ion should be inversely proportional to the slag viscosity.

$$D_1 = D_2 \frac{\eta_2}{\eta_1} \tag{3.41}$$

which in turn is proportional to the conductivity. The value of viscosity for the L slag is approximately 4 centipoise whereas the viscosity for the H slag is approximately 8 centipoise at 1500°C (figures 3.17a,b). Specific diffusivity values are expected to be on

the order of $1x10^{-5}cm^2/sec$ for the low FeOx slag systems compositions in agreement with the values typically found for metallurgical slag systems. The L slag should demonstrate diffusivity values approximately twice as large as the H slag.

Both the Jiao/Themilis and the diffusivity approaches demonstrate that increasing concentrations of Fe should result in increased values of slag conductivity. The values computed from the self-diffusivity approach were in close agreement with those computed using the Jiao and Themilis regression data. The estimated electronic conductivity for the low iron oxide containing slags is assumed to be negligible because the low concentration of semi-conducting species ensures that the tunneling distance required for electron electron hopping is large.

3.2.4.3.2 High concentration slags

The conductivity of the Aus compositions were determined using the regression data by Jiao and Themilis as described above. The regression data falls within the parameters of the regression model. Comparison with data from Martin and Derge[83] (figure 3.18) at 1500°C and using an activation energy of 155 kJ resulted in slightly higher conductivities than those approximated by the regression data as shown in Table 3.2.

Table 3.2 Predicted values from literature.

	Composition				Concentration [62]		Basicity		Conductivity (1/Ω-cm)					Transport Num Fe	
							eqn 3.26	eqn 3.25	[72] eqn 3.37	[81] eqn 3.36	eqn 3.36-37	[83]	[75-78] eqn 3.39	[72] eqn 3.37	[75-78] eqn 3.39
Slag name	wt% Al2O3	wt% CaO	wt% SiO2	wt% FeO1.5	Density (g/cm3)	CFe mol/cm3	Basicity	basicity	Cond (Jiao)	Cond (slag)	Jiao+ slagatlas	Cond (slag)	Cond (slag)	tFe	tFe
H0	13.0	39.0	48.0	0	2.56	0	0.751	0.871	0.1	0.111	0.111	NA	0.111	0	0
H1/2	12.9	38.8	47.8	0.5		0.00016	0.751	0.871	0.103	NA	0.114	NA	0.117	0.027	0.052
H1	12.9	38.6	47.5	1		0.00032	0.751	0.871	0.105	NA	0.117	NA	0.123	0.053	0.098
H2	12.7	38.2	47.0	2		0.00064	0.751	0.871	0.111	NA	0.124	NA	0.136	0.103	0.181
H4	12.5	37.4	46.1	4		0.00128	0.751	0.871	0.124	NA	0.138	NA	0.161	0.196	0.310
L0	13.0	48.0	39.0	0	2.624	0.00000	1.102	1.319	0.169	0.173	0.173	NA	0.173	0	0
L1	12.9	47.5	38.6	1		0.00033	1.102	1.319	0.178	NA	0.181	NA	0.188	0.049	0.081
L2	12.7	47.0	38.2	2		0.00066	1.102	1.319	0.187	NA	0.191	NA	0.204	0.095	0.152
L4	12.5	46.1	37.4	4		0.00131	1.102	1.319	0.206	NA	0.211	NA	0.236	0.182	0.268
Aus1	0.0	26.0	44.0	30	3	0.01127	0.633	0.633	0.448	0.238	NA	0.588	NA	NA	NA
Aus8	0.0	22.3	37.7	40	3.3	0.01653	0.633	0.633	0.855	NA	NA	0.923	NA	NA	NA
Aus9	0.0	29.7	50.3	20	2.8	0.00701	0.633	0.633	0.244	NA	NA	0.252	NA	NA	NA

Figure 3.8 $CaO\text{-}SiO_2\text{-}FeO$ Phase Diagram. Points A, B, and C represent Aus slags 20, 30, and 40 wt% FeOx respectively[59].

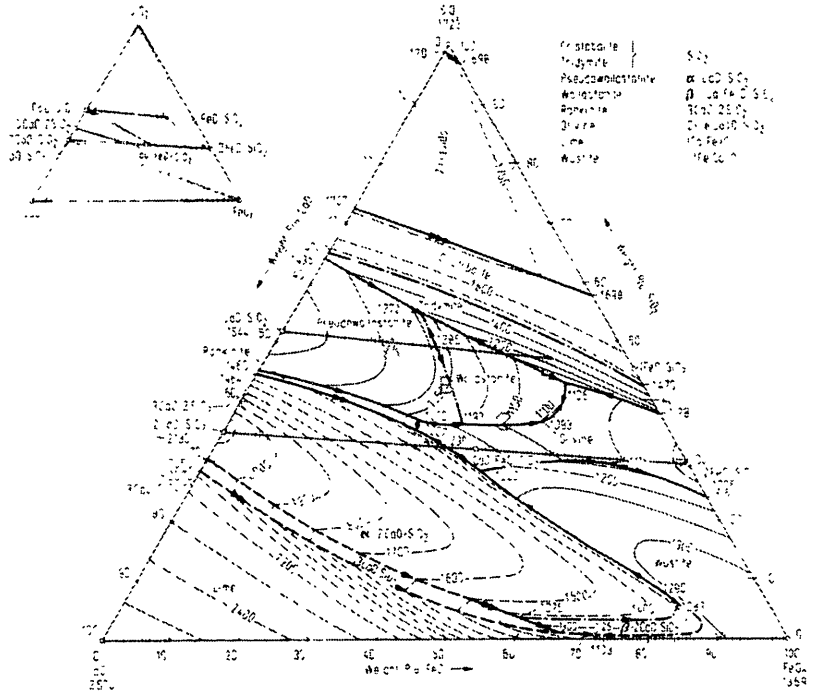

Figure 3.9 $CaO\text{-}SiO_2\text{-}Fe_2O_3$ phase diagram. Points A, B, and C represent Aus slags 20, 30, and 40 wt% Fe_2O_3 respectively[60].

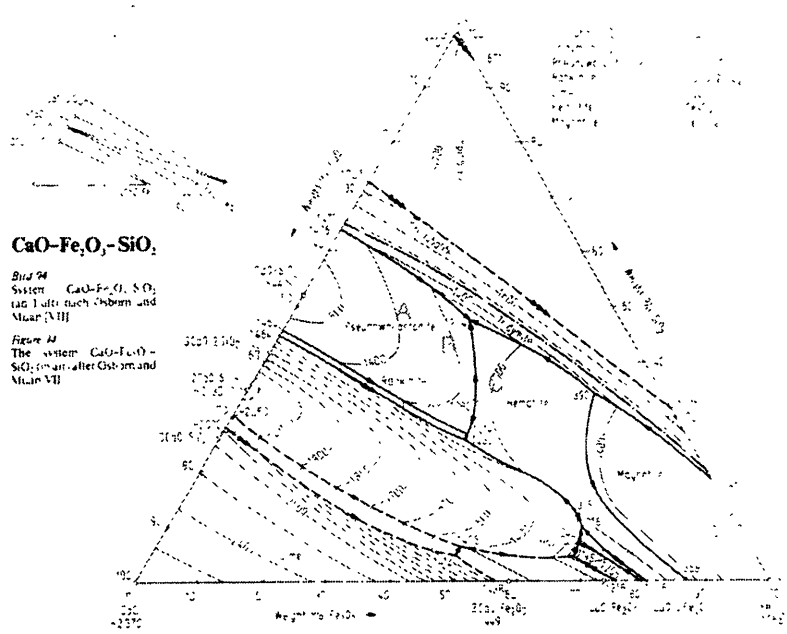

Figure 3.10 Al_2O_3-CaO-SiO_2 phase diagram. Points H and L represent 0wt%FeOx low concentration slags[61].

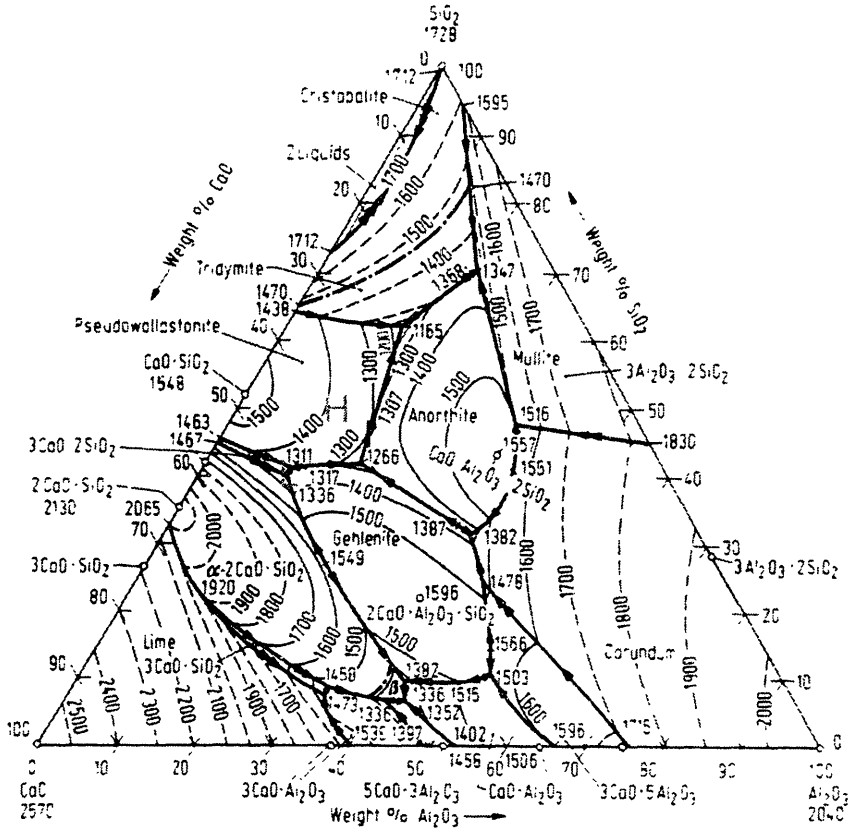

Figure 3.11 Electrochemical setups for measuring the conductivity of slags[71].

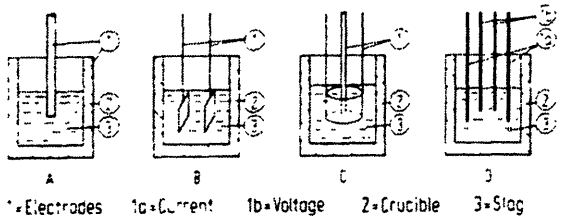

Figure 3.12 Conductivity data taken from Jiao and Themilis[72] demonstrating influence of Fe^{3+}/Fe_{tot} on conductivity.

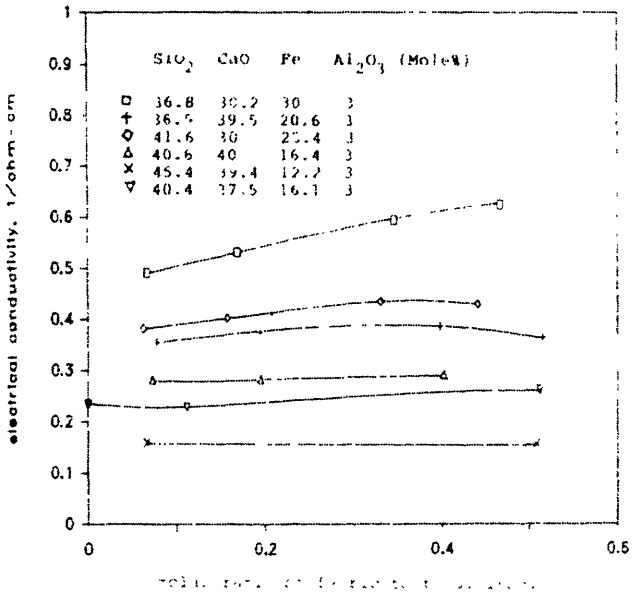

Figure 3.13 Conductivity data taken from Engell and Vygen[73] demonstrating lower conductivity with increased Fe^{3+}/Fe_{tot} ratio.

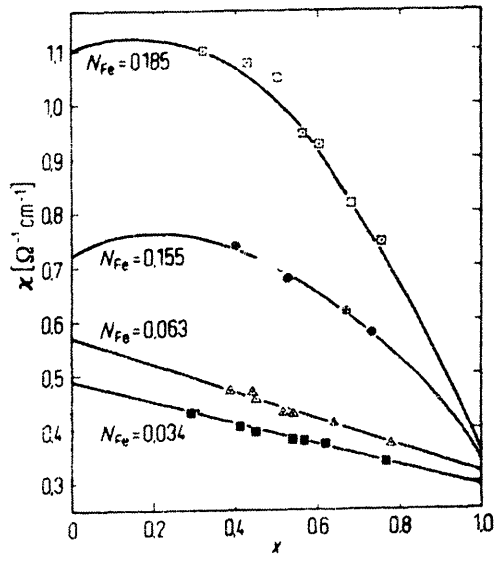

Figure 3.14 Tracer diffusivity data taken from Goto[78] on blast furnace slags.

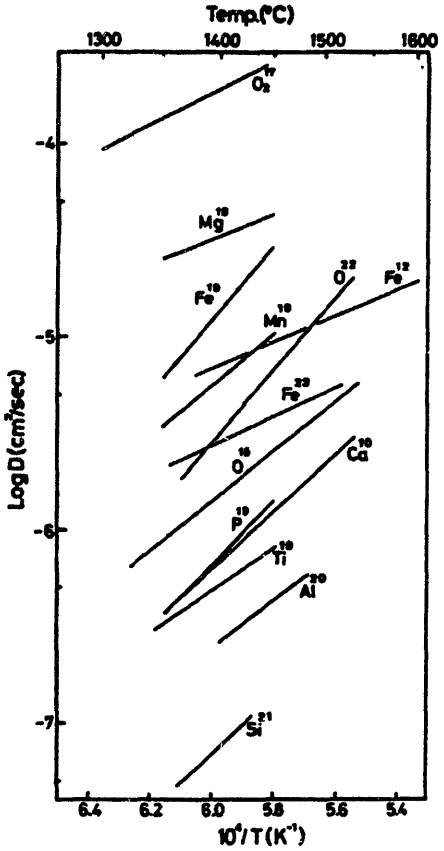

Figure 3.15 Self-diffusivity data taken from Goto[78] on steelmaking slags.

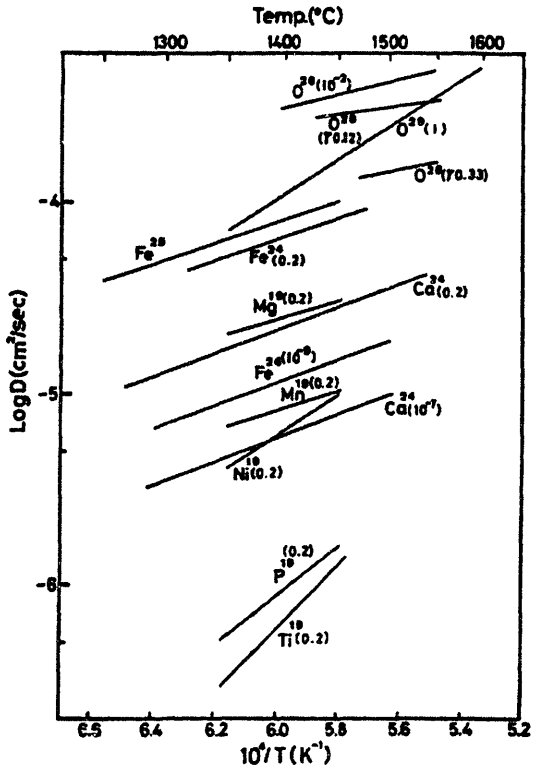

Figure 3.16 Diffusivity data taken from Goto et al.[77] demonstrating higher diffusivities for Fe and Ca with increased Fe^{3+}/Fe_{tot} ratio.

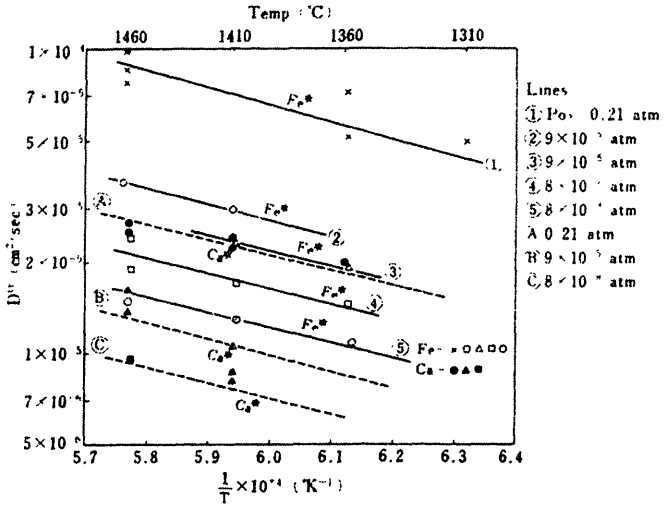

Figure 3.17a Viscosity data for Al_2O_3-CaO-SiO_2 slag system at 1500°C. Points H and L represent 0wt%FeOx low concentration slags[82].

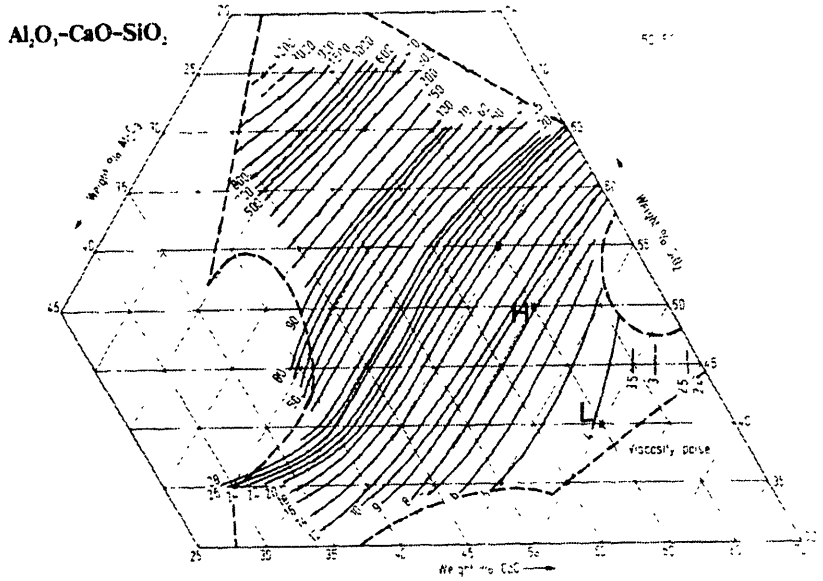

Figure 3.17b Viscosity data for Al_2O_3-CaO-SiO_2 slag system at 1400°C. Points H and L represent 0wt%FeOx low concentration slags[82].

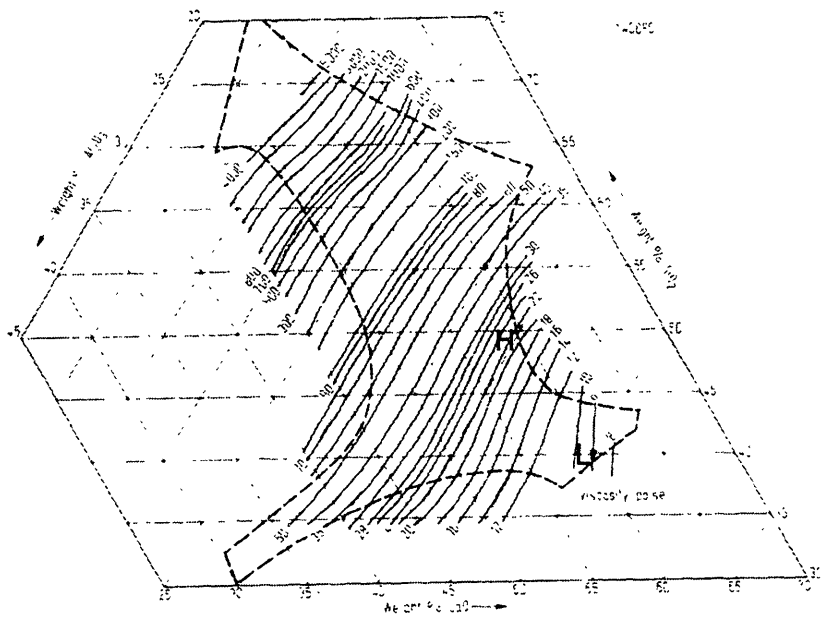

Figure 3.18 Conductivity data for CaO-FeO-SiO_2 slag system[83].

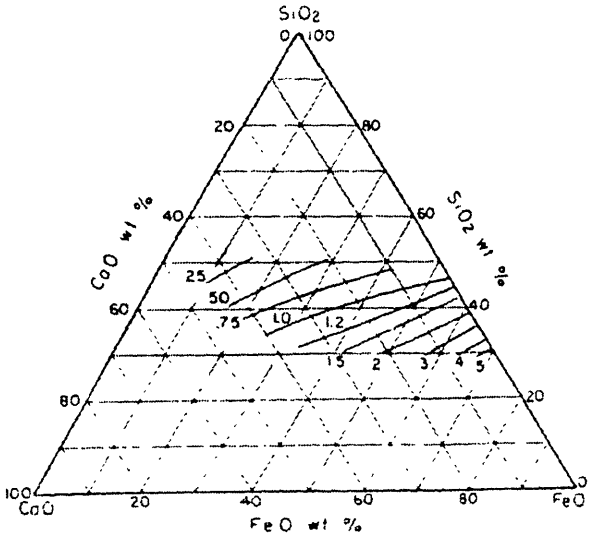

3.2.5 Thermodynamics and Redox Equilibrium

3.2.5.1 Introduction

Over the past 60 years a large thermodynamic database has been compiled on many of the subsystems of the Al-Ca-Mg-Si-Fe-P-O slag system. However, many compositions remain unexplored. Meanwhile, structure based thermodynamic models initially attempted by Masson[84] in 1965 have attempted to describe the slag structure from a theoretical viewpoint. Gaskell[85] summarized the classical work through 1980 on binary slag systems and recent work by Shim[86] and Selleby[87,88] have examined ternary oxide systems. Unfortunately, the complex polymeric nature of SiO_2 based oxide systems makes thermodynamic modeling of slag activities from first principles very difficult. Perhaps someday it will be possible to simply model the activity of a given species within a slag, but at present we must rely upon experimental data of similar slag structures and generally observed trends in order to determine the concentration-activity relationship of an oxide within the slag. The section below will describe the experimental relationships that exist between the concentration and activity of iron oxide species as they relate to temperature, slag structure, and oxygen activity.

3.2.5.2 Iron Oxide Redox Equilibrium

Unlike oxides such as alumina or calcia, iron oxide is a transition metal oxide that exhibits different valance states with changes in the oxygen partial pressure. Since the actual slag structure cannot be easily evaluated, several thermodynamic equations exist in the literature for describing the activity of redox species within a slag. According to

Turkdogan the general relationship between a transition metal oxide and oxygen partial pressure can be given by the following redox reaction equilibrium[89]:

$$M^{(m+n)+} + \frac{n}{2}O^{2-} = M^{m+} + \frac{n}{4}O_2 \tag{3.42}$$

where m is the valence of the reduced metal cation, and n is the valence change of the reaction with oxygen.

The equilibrium reaction for FeOx in $CaO\text{-}SiO_2\text{-}Al_2O_3\text{-}FeO_x$ slags would then be described by equation 3.43.

$$Fe^{3+} + \frac{1}{2}O^{2-} = Fe^{2+} + \frac{1}{4}O_2 \tag{3.43}$$

Yokokawa[90] has demonstrated that equation 3.44 is actually a better representation of the actual slag structure because with increasing basicity, or increased oxygen anion activity as defined by Temkin[91], ferric ions are found to be more stable than ferrous ions.

$$FeO_n^{(3-2n)+} = FeO_m^{(2-2m)+} + \tfrac{1}{2}(2n-2m-1)O^{2-} + \tfrac{1}{4}O_2 \tag{3.44}$$

The reader should note that use of equation 3.43 would predict the opposite response to basicity changes. Because of the complexities involved in properly defining the activity concentration relationship for the ionic species in equation 3.44 most literature data concerning the redox state of iron is reported using either equation 3.45 or equation 3.46 thereby intentionally neglecting the ionic nature of the slag[92,93].

$$FeO_{1.5} = FeO + \frac{1}{4}O_2 \tag{3.45}$$

$$\frac{1}{2}Fe_2O_3 = FeO + \frac{1}{4}O_2 \tag{3.46}$$

It should be stressed that the use of either of the above equations for determining thermodynamic information will predict identical results as long as all activity coefficients are properly defined. A thorough discussion of the relationships between the activity coefficients in the above equations can be found in Appendix A as an aid for comparing data from different literature sources. Equation 3.45 will be utilized during the remainder of this section for simplicity.

The equilibrium constant ($K_{3\text{-}2}$) for equation 3.45 is defined as:

$$K_{3-2} = \left(\frac{a_{FeO} P_{O_2}^{1/4}}{a_{FeO_{1.5}}} \right) \tag{3.47}$$

$K_{3\text{-}2}$ can be determined from thermodynamic data by Elliot for the Raoultian standard states of pure liquid FeO, pure solid Fe_2O_3, and pure oxygen at one atmosphere over the temperature range from 1665-1809K[94]:

$$\Delta G_{3-2}^{0} = 170200 - 76.5T = -RT \ln K_{3-2} = -nFE_0 \tag{3.48}$$

Where ΔG is the Gibbs free energy in J/mol.

Equation 3.47 can be rewritten to explicitly define the mole fraction ratio as a function of all equilibrium variables:

$$\log\left(\frac{X_{FeO_{1.5}}}{X_{FeO}} \right) = -\log(K_{3-2}) + \log\left(P_{O_2}^{1/4}\right) - \log\left(\frac{\gamma_{FeO_{1.5}}}{\gamma_{FeO}} \right) \tag{3.49}$$

Equation 3.49 demonstrates that the $FeO_{1.5}$/FeO concentration ratio (X_{rat}), defined by equation 3.50,

$$X_{rat} = \frac{X_{FeO_{1.5}}}{X_{FeO}} \tag{3.50}$$

increases with oxygen partial pressure and decreasing temperature. This has been verified by numerous investigators[90,92,93,95,96,97] in the literature. The influence of the activity coefficient ratio (γ_{rat}), defined by equation 3.51,

$$\gamma_{rat} = \frac{\gamma_{FeO_{1.5}}}{\gamma_{FeO}} \tag{3.51}$$

on X_{rat} has a complex relationship with the overall slag structure. In general, γ_{rat} demonstrates the following properties:

1. γ_{rat} increases with the addition of network forming oxides and decreases with the addition of network modifiers.
2. γ_{rat} is not strongly influenced by temperature[98].
3. γ_{rat} is not strongly influenced by the total iron content[96,98] especially in the Henrian regime.

A more thorough discussion of literature data concerning the CaO-SiO_2-Al_2O_3-FeOx slag system can be found in Appendix B.

3.2.5.3 Iron Oxide – Iron Melt Equilibrium

Slags in equilibrium with an iron electrode or iron containing melt are further constrained by the chemical reaction in equation 3.52 which influences the bulk concentration of FeOx (X_{FeOx}) within the slag.

$$FeO = Fe + \frac{1}{2}O_2 \tag{3.52}$$

The reaction rate constant ($K_{2\text{-}0}$) is defined as follows:

$$K_{2-0} = \frac{a_{FeO}}{a_{Fe} P_{O_2}^{1/2}} \tag{3.53}$$

where the Gibbs free energy[94] for pure liquid FeO in equilibrium with pure solid Fe_δ (1665-1809K) is given by equation 3.54:

$$\Delta G_{2-0} = -229800 + 43.87T = -RT \ln K_{2-0} \tag{3.54}$$

or for higher temperatures with pure liquid FeO in equilibrium with pure liquid Fe (1809-2000K) by equation 3.55:

$$\Delta G_{2-0} = -238400 + 49.53T = -RT \ln K_{2-0} \tag{3.55}$$

Equation 3.53 can be rewritten to explicitly define the mole fraction ratio as a function of all equilibrium variables:

$$\log(X_{FeO}) = \log(K_{2-0}) + \log(a_{Fe}) + \log\left(P_{O_2}^{1/2}\right) - \log(\gamma_{FeO}) \tag{3.56}$$

Equation 3.56 predicts that with increasing oxygen partial pressure and decreasing temperature the mole fraction of FeO in the oxide melt increases - this relationship has been demonstrated in the literature[95,96,99,100]. Equation 3.56 defines the equilibrium concentration of FeO within the slag in equilibrium with iron. It should be noted that for high temperature oxide systems ferrous and ferric species are both present at equilibrium and therefore the relationship defined in equation 3.49 is also valid. When the slag is in equilibrium with iron, equation 3.56 determines the total concentration of iron cations within the slag whereas equation 3.49 defines the X_{rat}.

Because the total iron content of the slag is often of greater interest than the mole fraction of Fe^{2+} it is common practice to recalculate all of the iron oxide to $X_{'FeO'}$. This approach simplifies quaternary phase diagrams to ternaries, and ternaries to binaries – with the known constraint that the phase diagram is in equilibrium with pure liquid or

solid iron and thus there exists a ratio of Fe^{3+} and Fe^{2+} species. The following equations are used for this conversion:

$$wt\%'FeO' = wt\%FeO + 0.9wt\%Fe_2O_3 \tag{3.57}$$

$$X_{'FeO'} \approx X_{FeO} + 2X_{Fe_2O_3} \tag{3.58}$$

$$X_{'FeO'} = \frac{\%'FeO'}{MW_{FeO}(N_{tot})} \tag{3.59}$$

$X_{'FeO'}$ is the mole fraction FeOx, %'FeO' is the wt% of iron units represented as FeO, MW_{FeO} is 71.85, and N_{tot} is the total number of oxide moles in the slag/cm^3 (approximately 1.6 for most steelmaking slags).

Several examples of the relationship between slag structure and activity of FeO from the literature data concerning the $CaO\text{-}SiO_2\text{-}Al_2O_3\text{-}FeOx$ system can be found in Appendix C.

3.2.5.4 Estimation of γ_{rat}

Section 3.2.5.2. and Appendix B developed the theory and literature data concerning γ_{rat}. By examining slag systems with similar structural composition as used in this thesis, γ_{rat} values were estimated for the H, L, and Aus slag systems.

Pargamin et. al.[101] investigated the Fe^{3+}/Fe^{2+} ratios of two $CaO\text{-}SiO_2\text{-}Al_2O_3\text{-}FeOx$ slag systems equilibrated in air at 1550°C using a Mossbauer spectrometer after quenching. The slag compositions examined by Pargamin et al can be described by equations 3.60 and 3.61.

Type I: $$\left[(0.35CaO - 0.65SiO_2)_{100-y}(Fe_2O_3)_y\right]_{100-z}[Al_2O_3]_z \tag{3.60}$$

Type II: $$\left[(0.55CaO-0.45SiO_2)_{100-y}(Fe_2O_3)_y\right]_{100-z}[Al_2O_3]_z \quad (3.61)$$

Where y = 10, 20, 30, 40 and z = 0, 10, 20.

The type I and type II slag systems were extremely similar to the slag compositions examined in this thesis. γ_{rat} values for the above slags were calculated using equation 3.49 using knowledge of the X_{rat} values in equilibrium with air at 1550°C. γ_{rat} was found to be approximately 1.6-3.1 for the type I slag and 1.05-1.3 for the type II slag at 10wt%FeOx. The γ_{rat} values obtained at 1550°C were assumed to be relevant at 1470°C because γ_{rat} values are not expected to change much with temperature[98]. In order to compare the type I and II slags with the H, L, and Aus slags in this thesis, basicity values were determined using equation 3.25 and can be found in table 3.2. The type I and type II slags demonstrated basicity values of 0.55 and 1.22 respectively.

γ_{rat} values for H, L, and Aus were then estimated by using basicity values as a guide. The L slag had an identical value of basicity as the type II slag and therefore the L slag was estimated to have a γ_{rat} value of approximately 1.2. The H slag had a basicity value half way between the type I and type II slags so γ_{rat} was estimated to be approximately 1.8. The Aus slag had a basicity value near the type I slag but contained more Fe_2O_3. Increased Fe contents in the Pargamin slag led to lower γ_{rat} values so the γ_{rat} value for the Aus slag was estimated to be near 1.5. The γ_{rat} values can be used to generate plots of Fe^{3+}/Fe_{Tot} as a function of the oxygen partial pressure for different temperatures. Figure 3.19 demonstrates the predicted Fe^{3+}/Fe_{Tot} curves for the H, L, and Aus slags at the operating temperature of 1470°C. Note that even γ_{rat} variation from 1.2 to 1.8 does not drastically shift the location of the Fe^{3+}/Fe_{tot} curve.

3.2.5.5 Estimation of γ_{FeO}

Section 3.2.5.3. and Appendix C developed the theory and literature data concerning γ_{FeO}. Figure 3.20[102] was used to estimate γ_{FeO} to be approximately 2.5 for the Aus containing slags at temperatures near 1550°C. γ_{FeO} values for the H and L slags were assumed to also be near 2.5 because data concerning γ_{FeO} for low FeOx containing slags is scarce.

Figure 3.19 Predicted Fe^{3+}/Fe_{tot} for γ_{rat}=1.2, 1.5, 1.8 representing L, Aus, H slags respectively at different applied potentials vs air reference at 1470°C.

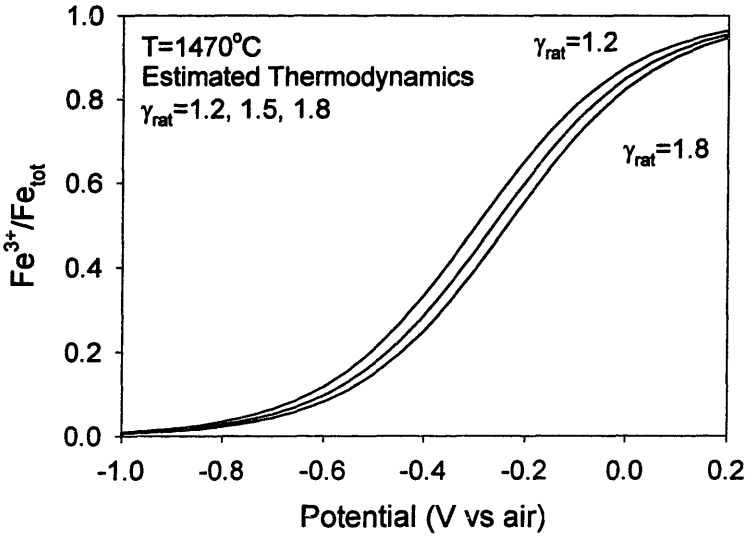

Figure 3.20 Activity of FeO(l) in CaO-FeO-SiO_2 melts in equilibrium with liquid iron at 1550°C[102].

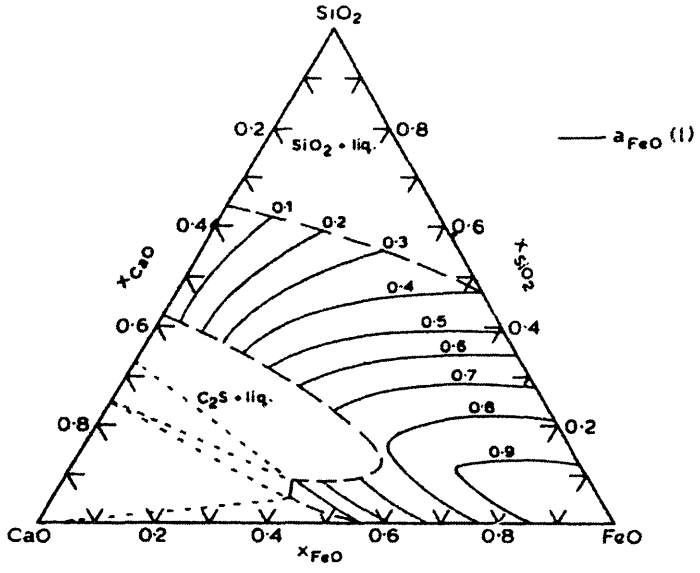

4 Ideal Electrode

Figure 4.1 demonstrates the sensor design anticipated during the original thesis proposal. This design is slightly different than the actual setups used within this thesis as will be described later. This section describes the initial attempts at achieving the sensor design of figure 4.1 and the reasons why these attempts were unsuccessful. The important aspects involved in developing a high temperature slag sensor are examined and discussed individually. The conclusions culminate in the design used for the experiments reported in this thesis.

4.1 Electrochemical Cell

In figure 4.1 the oxygen ion conducting PSZ separates the slag phase of interest from a reference gas phase. Oxygen is pumped from the slag phase across the zirconia into the gas phase by means of an applied potential between the counter electrode (CE) and the working electrode (WE). A reference electrode ensures that no polarization occurs at the counter electrode and provides a reference oxidation state using either the reference gas phase or a mixture of metal and metal oxide powders. The electrochemical cell would be described by equation 4.1.

$$Gas, CE \,/\, PSZ \,/ WE, Slag \tag{4.1}$$

The intimate contact between the CE, RE, and WE to the zirconia ensure that two three-phase interfaces exist in the system. Interface 1 is a gas-CE-ZrO2 three-phase interface, and interface 2 is a slag-WE-PSZ three-phase interface (figure 4.2). The electrolyte of importance to equation 4.1 is the PSZ which is a predominantly ionic conductor over a

wide range of oxygen partial pressures as demonstrated in the materials characterization section. The following reversible electrochemical reactions would be expected to occur at the 3-phase interfaces:

Interface I (CE-gas-ZrO2) (anode):

$$\tfrac{1}{2}O^{2-}_{ZrO_2} = \tfrac{1}{4}O_{2,gas} + e^-_{CE} \tag{4.2}$$

Interface II (WE-slag-ZrO2) (cathode):

$$\tfrac{1}{2}O^{2-}_{slag} + Fe^{3+}_{slag} + e^-_{WE} = Fe^{2+}_{slag} + \tfrac{1}{2}O^{2-}_{ZrO_2} \tag{4.3}$$

Note that the O^{2-} and Fe^{X+} species in the slag have been approximated by ionic forms in equation 4.3. In reality the slag structure is much more complex than equation 4.3 would indicate, as was discussed in the slag thermodynamics section. Equation 4.3 allows us to utilize the activity coefficients derived in the literature concerning the relative oxidation state of iron in slags with different overall structures.

The total cell reaction can be described by equation 4.4.

$$\tfrac{1}{2}O^{2-}_{slag} + Fe^{3+}_{slag} = Fe^{2+}_{slag} + \tfrac{1}{4}O_{2,gas} \tag{4.4}$$

Because the PSZ is primarily an oxygen anion conductor, the cell potential at equilibrium would be given by equation 4.5.

$$E = E_0 + \frac{RT}{F}\ln\frac{a_{FeO}P^{1/4}_{O_2}}{a_{FeO_{1.5}}} \tag{4.5}$$

Application of applied potentials would most likely result in a diffusion limited current of easily dissociable species to the WE 3-phase interface.

4.2 Selection of a Working Electrode

Significant time was spent determining the material and geometry required to generate a three-phase interface WE. In order for such a WE to operate properly in an amperometric measurement as described in the above analysis it must demonstrate the following properties: non-blocking, stable, reproducible surface area, adherent, and conductive. These characteristics will be discussed below in order of importance.

4.2.1 Non-blocking

A schematic of a blocking electrode to oxygen anions is shown in figure 4.3. A blocking electrode would convert the three-phase slag-WE-ZrO_2 interface into a simple WE-ZrO_2 interface. A WE-ZrO_2 interface will not yield ANY information concerning the slag phase because O^{2-} will not be removed from the slag during applied potential. This property of blocking electrodes is utilized by the Hebb-Wagner polarization method[103,104] in order to measure electronic transference numbers in electrolytes[105].

4.2.2 Stable

The WE must be composed of a material which does not chemically react with the slag phase. A reactive WE would alter the composition of the slag near the electrode thereby altering slag structure or viscosity and influencing the measured currents. Dissolution of easily dissociable metallic oxides might also provide an additional source

of current. In order to investigate a variety of slag conditions it would be desirable to have an inert WE over a wide range of reducing and oxidizing conditions. A reactive electrode would also have a problem with maintaining a reproducible surface area as described in the next section.

4.2.3 Reproducible Surface Area and Morphology

Because of the amperometric nature of the sensor, it is imperative that the surface area and morphology are either strictly controlled, calibrated, or measured prior to use. As will be described in the electrochemical methods section, any diffusion limited currents generated during use will be strictly proportional to the apparent surface area. Factors which might alter the effective surface area include: chemical reaction with slag, loss of adherence to ZrO_2, surface tension effects at the three-electrode interface, thickness of cermet coating, pore size in electrode coating, etc.

4.2.4 Adherence to ZrO2

In order to maintain the three-phase interface area the WE must remain adherent to the ZrO_2. The loss of electrode adherence would result in the formation of two 2-phase interfaces and an additional electrolyte phase in the electrochemical cell as shown in figure 4.4 and equation 4.6.

$$Slag,WE\,/\,Slag\,/\,ZrO2\,/\,CE,gas \qquad (4.6)$$

Partial adherence of the WE would add complexity as both electrochemical cells, equation 4.6 and 4.3, would operate in parallel. Loss of adherence will also affect the 3-phase surface area reproducibility.

4.2.5 Conductive

The WE must be conductive such that iR drops within the electrode do not generate a significant potential in comparison with the total applied cell potential. Significant electrode iR drops would result in concentration gradients along the electrode surface. Equations 4.7 and 4.8 describe the maximum current density allowed in order to ensure that the potential drop across the electrode surface is less than 1% (Appendix D). Equation 4.7 describes the required condition for a planar electrode.

$$\frac{i}{A} = \frac{0.02tV_0\sigma}{L^2} \tag{4.7}$$

Where i is the current (A), A is the surface area (cm^2), t is the thickness (cm), V_0 is the applied potential (V), and σ is the electronic conductivity of the electrode ($1/\Omega$-cm).

Equation 4.8 describes the required condition for a wire electrode.

$$\frac{i}{A} \leq \frac{0.01\sigma rV_0}{L^2} \tag{4.8}$$

Where r is the radius of the electrode (cm).

4.3 Searching for the Ideal Working Electrode

Several electrode materials and structures were examined during the first 1.5 years of the thesis with the hopes of fulfilling the above criterion for the ideal working

electrode. The following electrodes were evaluated for use as the WE: Metal-PSZ cermets, Molten Ag, $LaCrO_3$, and a variety of Pt products.

4.3.1 Mo/ZrO_2 Cermet

Zirconia based cermets were initially thought to provide the best solution for the ideal working electrode. Cermets have been utilized in order to provide metal-zirconia-gas electrodes for molten metal deoxidation[106] and fuel cells[107]. A cermet is made by mixing and sintering metallic and zirconia powders in order to create a two phased structure exhibiting both ionic and electronic conduction properties. Although several different cermet compositions and preparation techniques were examined (Appendix E), adherence of the cermet to the zirconia in the presence of slag could not be obtained. A typical result after immersion into the slag is demonstrated in figure 4.5. The electrode demonstrates a lack of adherence – effectively resulting in two two-phase interfaces and an additional electrolyte phase as in equation 4.6. Despite the experimental difficulties associated with achieving perfect adherence of the cermet a number of additional theoretical problems existed as well and are described below.

As described earlier amperometric measurements will be directly proportional to the effective surface area of the WE. The effective 3-phase interface area of a cermet will be a strong function of its sintering history, particle size, wetting angle with the slag, and the conductivity of the slag. This presents a problem for WE surface area standardization. In addition there may be competition between current paths based upon 3-phase and 2-phase electrochemical cells (equations 4.3 and 4.8) in the same system.

This would result in an effective electrode surface area that would change with the slag conductivity.

Another problem is the reactivity of Mo with the slag phase. Assuming unit activities for Mo and MoO_2, Mo would be expected to oxidize even in relatively reducing environments. For effective electrode conduction, stable electrode surface area, and stable slag composition, the slag must be quite reducing. The slags investigated in this thesis focused on higher oxidation states and therefore use of a Molybdenum was judged to be inappropriate.

4.3.2 Other Cermets

Cermets based on other metals were also considered to be inappropriate.

Fe based cermets were rejected because of the possibility of iron oxidation prior to the sensor measurement. Jahanshahi and Wright[108] suspected that partial oxidation of iron electrodes in an electrolysis experiment by Arato et al.[109] may have influenced overall results during electrochemical measurements of slags containing low quantities of FeOx. The use of iron electrodes in the current investigation was not explored.

Pt based cermets were rejected because of the large expense required for testing and producing a useable cermet material.

4.3.3 Molten Ag

A molten silver based electrode was utilized by Iwase et al. in order to provide a three phase interface for potentiometric slag analysis[110]. Ag and Fe are completely

immiscible over a wide range of temperatures (figure 4.6)[111] and hence the activity of Fe deposited within the Ag can be assumed to be effectively 1. Also, Ag is stable over a much wider range of oxygen partial pressures than is Mo. A similar approach was attempted for the amperometric slag sensor (figure 4.7). Several problems were encountered during operation. The large Ag/ZrO_2 two phase interface may act as a large blocking electrode resulting in a relatively large fraction of electronic current even at low applied potentials. Also, oxygen dissolved within the bulk Ag demonstrated an ionic signal independent of the oxygen removed from the slag phase. The Mo electrode immersed in the Ag resulted in a MoO_2 signal during potential sweeps. Use of a Pt lead was unsuccessful because it rapidly dissolved into the Ag causing problems with maintaining WE contact. The large two-phase interface area likely dominated over the small three-phase interface area. In addition, the strange geometry ill-suited for two-phase area measurements would cause difficulties in determining the true effective surface area of the working electrode.

This system was judged to be too complex for accurate sensing me ods because of the variety of experimental noise which would be created by problems ranging from dissolved oxygen in the silver and unknown effective WE surface areas to potentially large electronic current at the Ag-ZrO2 two phase interface.

4.3.4 $LaSrCrO_3$ and TiO_2 Doped ZrO_2

Mixed conducting oxide materials such as $LaSrCrO_3$ and TiO_2 doped ZrO_2 have been suggested for use as electrodes for high temperature environments because of their stability in oxidative environments while maintaining relatively high conductivity. Such

materials would avoid the problems associated with three-phase interfaces in cermets because they are a homogenous phase providing both electronic and ionic conduction paths. As described in Appendix E both materials appeared to sinter intimately with the zirconia, however, no tests were run placing the electrode materials in contact with a slag phase. These materials were not tested in the slag phase because of the following concerns: inadequate conductivity (Appendix D), slag reactivity, and difficulty in attaching electrode leads. Appendix D demonstrates the problems associated with inadequate conductivity of the $LaSrCrO_3$ electrode under normal operating conditions. For current densities larger than $1x10^{-5}$ A/cm^2 significant potential drops will occur along the WE resulting in concentration gradients within the slag phase.

4.3.5 Pt Ink, Wire, Gauze

Use of platinum products to develop reproducible 3-phase interfacial electrode area was unsuccessful. Pt wire, gauze, or foil would not produce an intimate three phase interface unless ZrO_2 was pressed onto the Platinum as shown in figure 4.8. Under such conditions the electrode consisted of a Pt/ZrO_2 blocking electrode of unknown area, a small region of unknown three-phase interface area, and a complex geometry two-phase interface area. The electrode structure of Pt ink based electrodes was found to change with time – especially when the ink was in contact with slags containing large quantities of FeOx. Even for low FeOx containing slags corrosion of the zirconia and sintering conditions altered the structure of the platinum ink as shown in figure 4.9.

4.4 Solution to the 3-Phase Interface Problem

After significant exploration for a WE exhibiting the three-phase interfacial design described in the thesis proposal the search was abandoned. The lack of previous research or literature in designing electrodes which demonstrated the list of required properties in section 4.2 precluded that the thesis either focus entirely on developing proper techniques for the attainment of such an electrode OR focus on the utilization of a more manageable experimental setup. The remainder of the thesis will focus on the general electrochemical cell represented by equation 4.6 and shown in figure 5.1. Instead of an oxygen porous WE intimately in contact with the zirconia electrolyte, a platinum wire electrode of known diameter is immersed a known distance into the slag. The new WE demonstrated chemical stability, reproducible surface area and no longer required adherence to the zirconia or control of a three-phase interfacial area.

Figure 4.1 "Ideal" Sensor Design (not achieved).

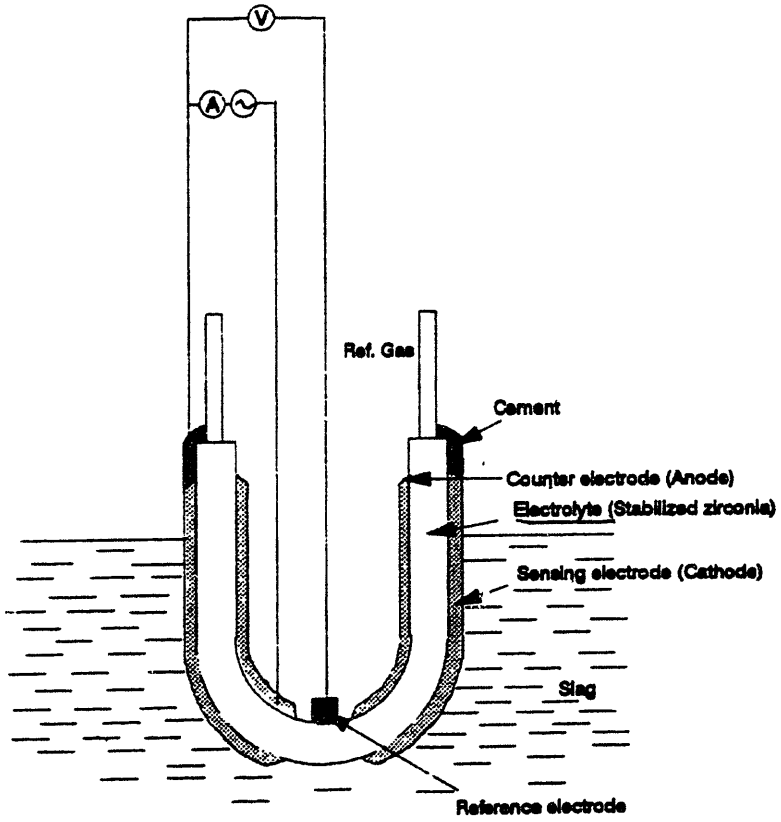

Figure 4.2 Example of a three-phase interface.

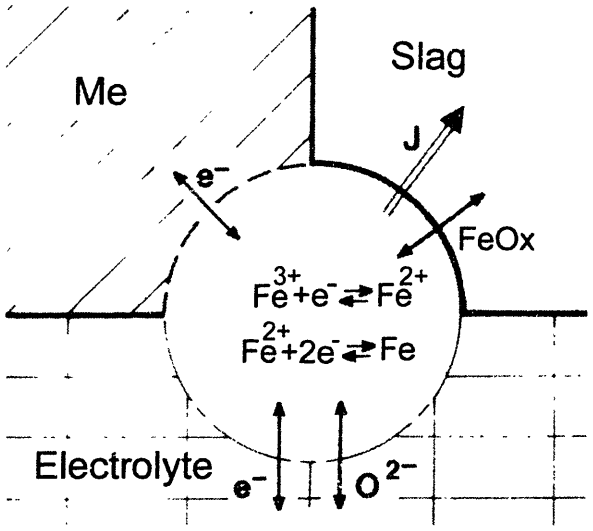

Figure 4.3 Blocking Electrode. A blocking electrode would prevent any useful information from being obtained from the slag phase. Blocking electrodes can be used to determine the electronic transport properties of mixed electrolytes.

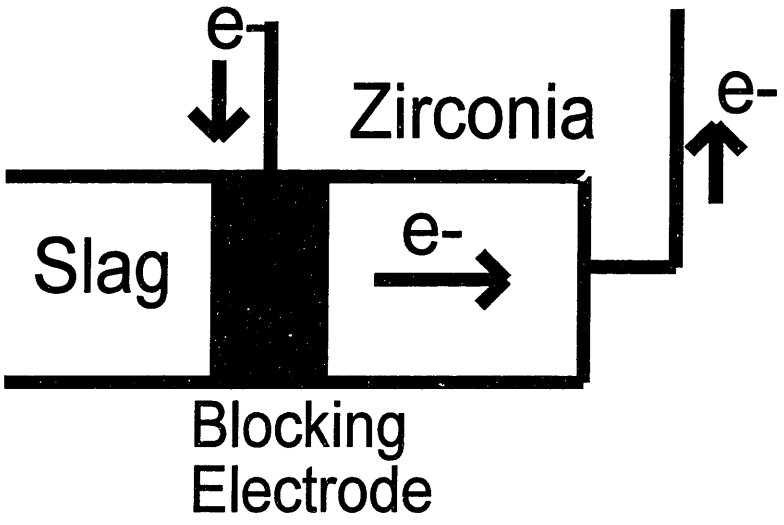

Figure 4.4 Example of a cell with two 2-phase interfaces.

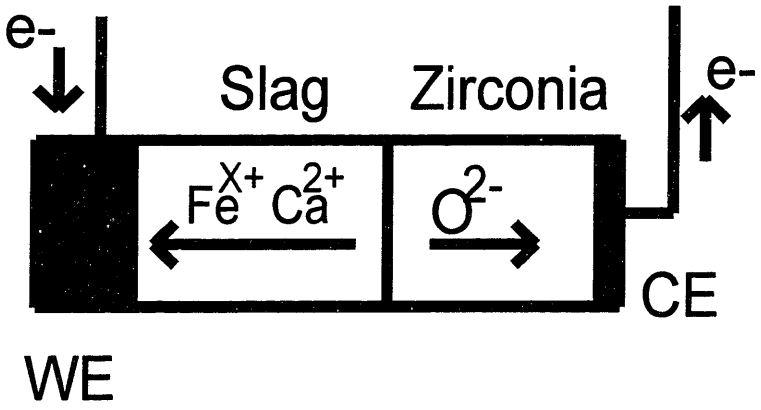

Figure 4.5 SEM Photograph of cermet exposed to slag.

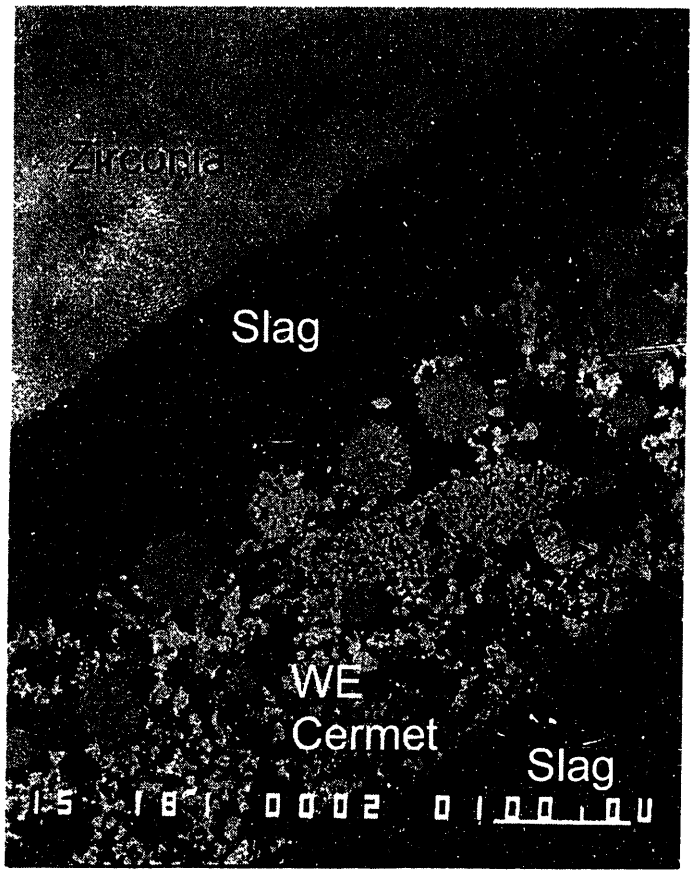

Figure 4.6 Ag/Fe Phase Diagram. Ag and Fe are completely immiscible over a wide range of temperatures[111].

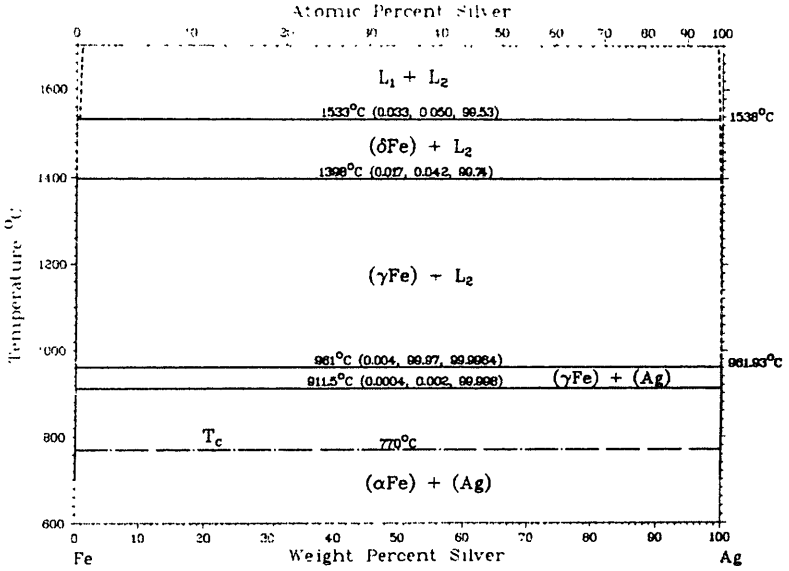

Figure 4.7 Ag based slag sensor.

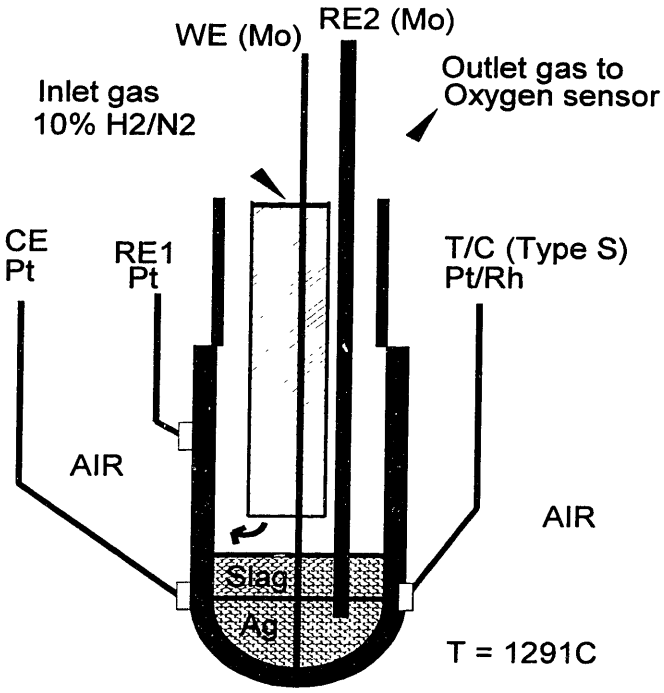

Figure 4.8 SEM photograph of zirconia pressed against a Pt foil electrode.

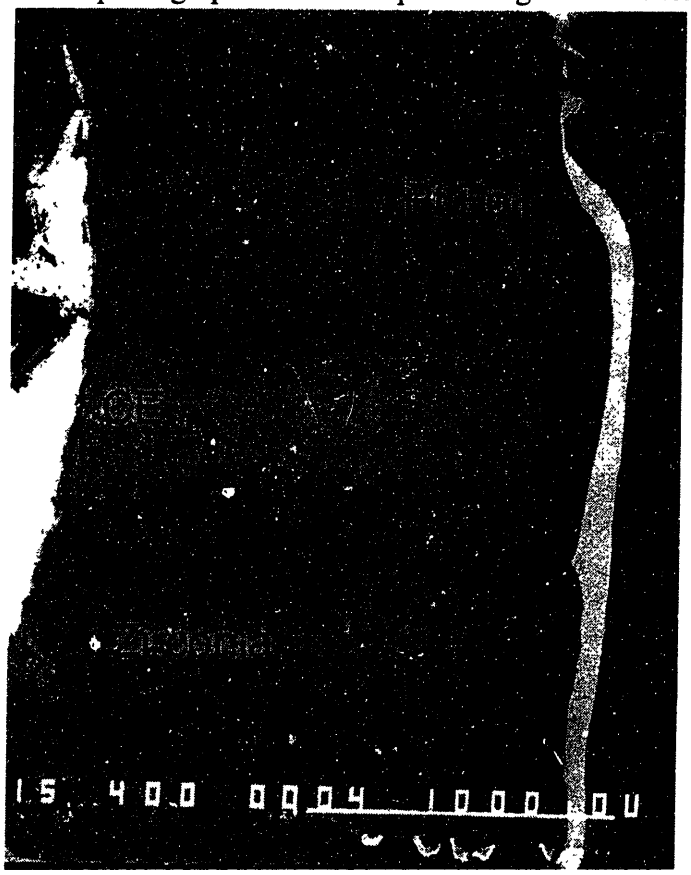

Figure 4.9 SEM photograph of the platinum ink / zirconia interface.

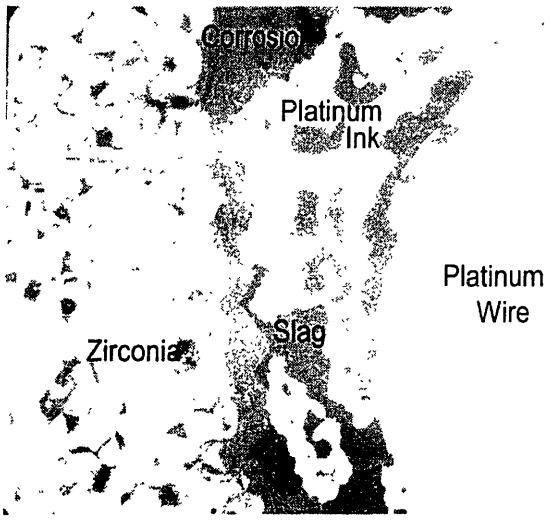

5 Experimental – Low FeOx

This chapter will describe the amperometric measurements applied to slags containing low quantities of FeOx (<5wt%). The amperometric techniques utilized were; applied DC potential steps and impedance frequency sweeps at applied DC potentials. The chapter consists of the following sections: First the experimental setup will be described. Then the appropriate theory will be introduced for the different measurement techniques. Finally, the results will be reported and compared with information from conventional open circuit measurements.

5.1 Experimental Setup

This section describes the experimental setup and procedures used for investigating the low FeOx containing slags with OCV, potential step, and impedance methods.

5.1.1 Experimental Cell

Figure 5.1a-c demonstrates the three different setup types (A, B, C) used during the low concentration measurements. The setups differ only in the surface area of immersed electrode and the use of a physically discrete primary reference electrode (RE1) in contact with the reference gas phase. Therefore, the minor differences associated with the different setups are not expected to significantly impact the final results. In all cases the zirconia solid electrolyte separates the reference gas phase

consisting of air from the slag phase to be measured. An inert Argon gas (BOC gasses – Grade V) is flowed through the system in order to prevent any slag/gas reactions from occurring during experimentation. The counter electrode (CE) consisted of a platinum gauze (mesh size, 5mm ht x ZrO_2 OD) sintered to the zirconia tube outer diameter (OD) using platinum ink (Engelhard #6926). Two lead wires were connected to the CE in order to provide an S-type thermocouple (T/C) for temperature measurement. For the type A setup the Pt/10%Rh wire was utilized as the CE and the Pt wire was utilized only for T/C measurements. For the type A and B measurements the Pt wire was utilized as RE1 and the Pt/10%Rh electrode was utilized as the CE. An additional electrode was utilized in the gas phase for the type A measurements consisting of another T/C where the Pt electrode was used as RE1. RE1 consisted of a 0.01 inch diameter wire sintered to the zirconia with Engelhard Pt ink and was located 2mm above the CE with a surface area of (2mm x ZrO_2 OD). The working electrode (WE) and secondary reference electrode (RE2) were composed of 0.02 inch diameter Pt and Pt/10%Rh wires (Engelhard standard grade) respectively. The wires were carefully immersed 0.55cm (+/- 0.05cm) into the slag in order to control the surface area of the WE. The wires were insulated using a double-bore alumina tube in order to prevent inadvertent contact between the WE, RE2, and ZrO_2. In type C measurements the weld bead of the Pt/10%Rh wire was located above the slag surface and only a single wire was immersed into the slag. This helped better standardize conductivity measurements of the cell and is discussed further in Appendix F.

Two different zirconia tubes were used throughout the measurements. The majority of experiments utilized the ZDY-4 zirconia tube while some measurements

utilized the ZDY-9 zirconia tube. The ZDY-4 tube was a lower quality tube containing a binder material. Both of the tubes contained 4 mol%Y_2O_3 and have been characterized in the zirconia characterization section. The experimental differences between the two types of tubes in the current setup are expected to be negligible except for geometrical variation caused by differing OD and ID values. In general, ZDY-9 tubes tended to have a smaller ID and OD than the ZDY-4 tubes.

Slag compositions ranging from 0-4 wt%FeOx in CaO-Al_2O_3-SiO_2-FeOx containing slags were examined for two different CaO/SiO_2 ratios denoted H and L for high and low viscosity. Specific concentrations for the two types of slags are described in equations 5.1 and 5.2.

H slags:

$$\left(0.39CaO - 0.48SiO_2 - 0.13Al_2O_3\right)_{100-z}\left[Fe_2O_3\right]_z \qquad z = \{0,0.5,1,2,4\} \qquad (5.1)$$

L slags:

$$\left(0.48CaO - 0.39SiO_2 - 0.13Al_2O_3\right)_{100-z}\left[Fe_2O_3\right]_z \qquad z = \{0,1,2,4\} \qquad (5.2)$$

The preparation techniques and theoretical properties for each of the compositions was previously described in the slag characterization section. A proper amount of slag sinter was charged into the sensor at room temperature such that the slag height would be approximately 1.5cm from the tube bottom when molten at operating temperature (1470°C). This generally varied between 1.1g and 1.6g depending upon the ID of the zirconia tube.

Table 5.1 completely describes the experimental cell parameters used in each of the low FeOx experiments described above.

5.1.2 Equipment

Figure 5.2 describes the general experimental setup surrounding the electrochemical cell. A $MoSi_2$ resistance furnace was utilized to heat the cell assembly. In order to prevent thermal shock to the zirconia tube the cell was heated at a rate of 4°/min to the operating temperature. All experiments were conducted at temperatures near 1470°C and the electrode cell was positioned in the same location in the furnace for each experiment in order to ensure that any temperature gradients were identical for all cases. Grade V Argon gas was flowed through the system using an Aalborg gas flowmeter in order to maintain a constant flow rate of 15 ml/min which provided a gas shield for the slag phase. The exit gas from the system was measured using a zirconia-based oxygen sensor constructed in our lab and described in Appendix G. Electrochemical measurements were taken using a Solartron 1287 potentiostat and either a Solartron 1260 (mostly H slags) or Solartron 1250 (mostly L slags) impedance analyzer. The electrochemical equipment was controlled and the data collected using a GPIB connection to a 486 computer running Corrware, Z60, and/or Zplot2 software developed by Scribner Associates. Measurements were analyzed using a Tektronix digital oscilloscope in order to ensure that proper waveforms were applied to the system. The oscilloscope was also used to determine when slag/metal contact occurred during lowering of the WE into the slag. A Hydra data acquisition system was utilized to constantly measure various cell potentials throughout the system at one second intervals in order to provide a "histogram" of the entire experiment including the oxygen sensor and thermocouples.

5.1.3 Measurement Procedure

The following steps describe the procedure followed for a typical experimental measurement on a given low FeOx slag.

1. At room temperature the cell is fabricated as shown in figure 5.1a-c and the slag sinter is charged into the sensor. The WE tip is positioned 5.5cm above the slag surface and argon is flowed through the system at 15 ml/min. The furnace is then programmed to heat to 1470°C at a rate of 4°/min. The hydra data acquisition system is turned on and begins recording data.
2. When the furnace reaches a temperature of 1470°C the system is allowed to equilibrate for at least 15 minutes. The WE is lowered slowly until contact with the slag is established. The oscilloscope is used to determine when contact with the slag has been achieved. After immersion into the slag, a high frequency (HF) impedance sweep measurement from 100kHz to 10kHz is performed on the system. HF impedance sweep measurements are performed at 0.1cm increments during lowering of the electrode in the slag until the electrode depth is 0.55cm. The HF impedance sweeps during lowering of the electrode are used to assist calibration of surface area and conductivity measurements as will be described in the results section.
3. At a depth of 0.55cm (1470°C) a complete impedance sweep from 100kHz to 10Hz is run. After the impedance measurement the OCV is measured for approximately five minutes or until the system appears relatively stable. This OCV measurement is used to approximate the signal obtained using a conventional OCV measurement device.

4. Amperometric measurements are then conducted in the following manner. An applied potential step of -0.2V (RE2 vs RE1) is applied for 120 seconds using the potentiostat. After 120 seconds an impedance frequency sweep from 100kHz to 10Hz is run on top of the DC potential step. An OCV recovery is then measured for 5 minutes in order to allow the cell to recover.
5. Step 4 is then repeated for several different DC potential steps (-0.4V, -0.6V, -0.8V, -1V, -1.1V, -1.2V etc.) This data provides the basis of the amperometric measurements reported in this thesis.
6. After all amperometric measurements are completed the furnace is turned off and the cell is quenched to room temperature.

The quenched cell is sectioned and examined using visual inspection, SEM, and/or chemical techniques.

Table 5.1 Cell parameters for low FeOx containing slags.

Experiment Name	Low/High Viscosity	wt%FeOx unless noted	g slag charged	System Temp C	Setup Type	Zirconia Type	ZrO2 ID (cm)	ZrO2 OD (cm)
pap2	Low	1	1.613	1460	A	ZDY-4	0.72	1
pap5	Low	2	1.611	1465	A	ZDY-4	0.72	0.99
pap6	Low	4	1.63	1463	A	ZDY-4	0.72	1.01
pap7	Low	4	1.5	1466	A	ZDY-4	0.69	0.975
pap8	High	1	1.38	1467	A	ZDY-4	0.675	1
pap9	Low	1 wt%CuOx	1.27	1470	A	ZDY-4	0.64	1.01
pap10	High	2	1.315	1465	B	ZDY-4	0.645	0.965
pap12	High	0	1.5	1465	B	ZDY-4	0.685	1.015
pap13	High	2	1.61	1468	C	ZDY-4	0.715	0.99
pap14	High	4	1.21	1465	B	ZDY-9	0.6	0.93
pap15	High	0.5	1.1	1467	C	ZDY-9	0.595	0.87

Figure 5.1a Type A experimental cell design. (two WE, separate RE1)

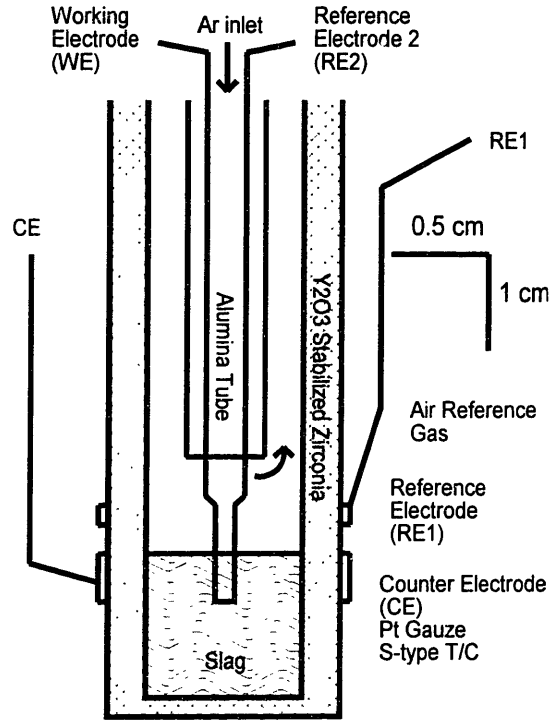

Figure 5.1b Type B experimental cell design. (two WE, single RE1)

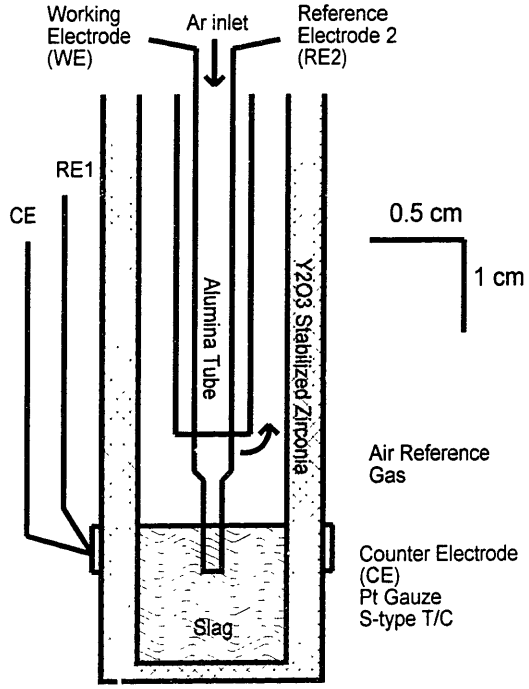

Figure 5.1c Type C experimental cell design. (single WE, single CE/RE1)

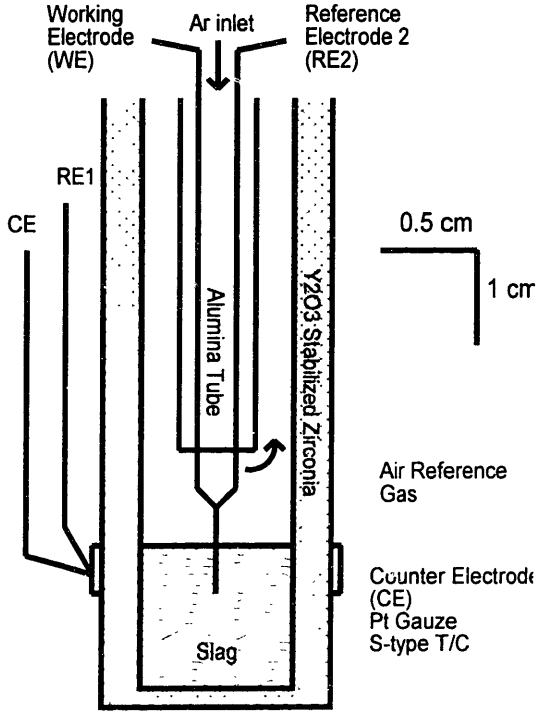

Figure 5.2 General experimental setup.

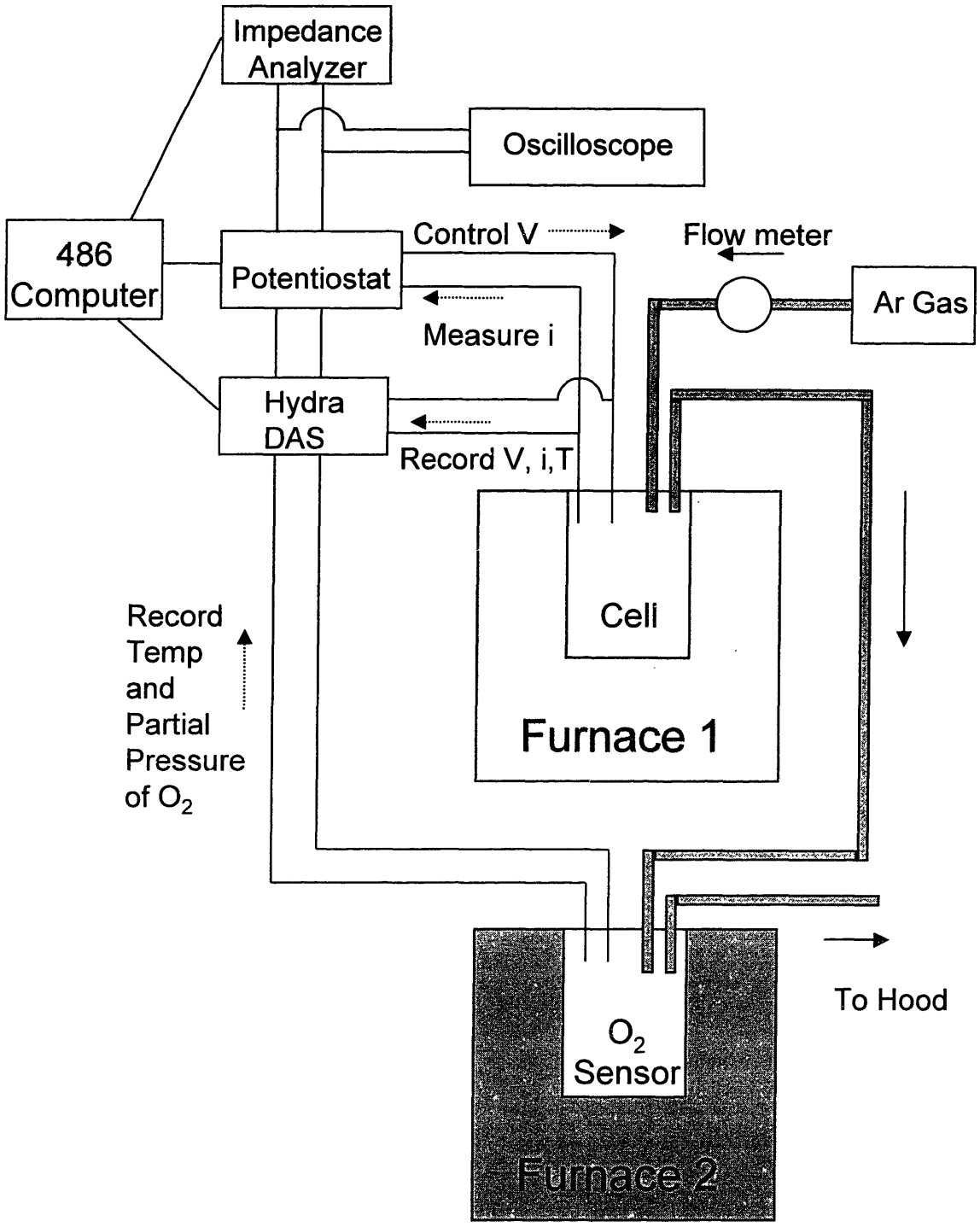

5.2 Experimental Theory

The Experimental Theory section describes the theory behind the three types of measurements investigated in this thesis. First, the reversible cell potential is established and the relationship between the open circuit potential and redox equilibrium is discussed. Next, the three major time regimes of the current response to an applied DC potential step are evaluated. Finally, the fundamentals of impedance are developed and applied to the analysis of an appropriate equivalent circuit describing the electrochemical cell. The theory and equations derived within this section will be of invaluable use to the analysis of the experimental results in the Results and Discussion section.

5.2.1 Reversible Cell Potential

5.2.1.1 Electrochemical Reactions

The electrochemical cell primarily investigated in this thesis consisted of oxidized slags containing small quantities of FeOx (figure 5.3) and can be described by equation 5.3.

$$\underset{WE}{Pt_{(s)}} \mid \underset{slag}{Fe^{3+}, Fe^{2+}, O^{2-}} \mid \underset{ZrO_2}{O^{2-}} \mid \underset{air}{O_2}, \underset{CE,RE}{Pt_{(s)}} \tag{5.3}$$

Equations 5.4 to 5.6 describe the reactions which occur at each cell interface during the application of current for low FeOx containing slags. At the platinum WE, ferric cations are reduced to ferrous cations as described by equation 5.4.

$$Fe^{3+}_{slag,WE} + e^{-}_{Pt,WE} \rightarrow Fe^{2+}_{slag,WE} \tag{5.4}$$

At the slag-electrolyte junction oxygen anions are stripped from the slag to provide a mechanism for conduction within the zirconia electrolyte.

$$\tfrac{1}{2}O^{2-}_{slag/ZrO_2} \rightarrow \tfrac{1}{2}O^{2-}_{ZrO_2} \tag{5.5}$$

This will give rise to a Donnan or membrane potential at this interface because of the difference in the oxygen activity between the two phases. Although written as free oxygen anions in the slag phase, equation 5.5 should be interpreted more generically and may represent the removal of oxygen species from more complex anionic species. At the CE and RE the following anodic reaction occurs resulting in oxygen evolution:

$$\tfrac{1}{2}O^{2-}_{ZrO_2} \rightarrow \tfrac{1}{4}O^{air}_2 + e^-_{Pt\,II} \tag{5.6}$$

The overall transformation during small applied potentials can be described by the cell reaction equation 5.7.

$$Fe^{3+}_{slag/WE} + \tfrac{1}{2}O^{2-}_{slag,ZrO_2} \rightarrow \tfrac{1}{4}O^{air}_2 + Fe^{2+}_{slag/WE} \tag{5.7}$$

The free energy for equation 5.7 is described by equation 5.8.

$$\Delta G = \Delta G^0 + RT\ln\left(\frac{a_{Fe^{2+}_{slag/WE}} P^{1/4}_{O^{air}_2}}{a_{Fe^{3+}_{slag/WE}} a^{1/2}_{O^{2-}_{slag/ZrO_2}}}\right) \tag{5.8}$$

5.2.1.2 Developing the reversible cell potential

For the limiting case when the applied current approaches zero, equation 5.9 becomes valid.

$$\Delta G = -nFE_{rev} \tag{5.9}$$

Therefore, for open circuit potential (OCV) measurements, the Nernst equation for the cell (equation 5.10) describes the relationship between the measured potential and the relative activities of each of the redox couple species as well as the slag basicity.

$$E_{OCV} = E_0 - \frac{RT}{F}\ln\left(\frac{a_{Fe^{2+}_{slag/WE}} P^{1/4}_{O_2^{air}}}{a_{Fe^{3+}_{slag/WE}} a^{1/2}_{O^{2-}_{slag/ZrO_2}}}\right) \tag{5.10}$$

E_0 is defined as the measured potential when all of the activities are at their standard state (a=1).

If the slag is relatively homogenous, the oxygen activity at the slag-zirconia interface would be identical to the oxygen activity at the slag-WE interface.

$$a^{slag/ZrO_2}_{O^{2-}} = a^{slag/WE}_{O^{2-}} \tag{5.11}$$

This allows us to relate equation 5.10 with the thermodynamic data as discussed in the Slag Characterization section as follows.

$$E_{OCV} = E_0 - \frac{RT}{F}\ln\left(\frac{a_{Fe^{2+}_{slag/WE}} P^{1/4}_{O_2^{air}}}{a_{Fe^{3+}_{slag/WE}} a^{1/2}_{O^{2-}_{slag/WE}}}\right) = E_0 - \frac{RT}{F}\ln\left(\frac{a^{WE}_{FeO} P^{1/4}_{O_2^{air}}}{a^{WE}_{FeO_{1.5}}}\right) = E_0 + \frac{RT}{F}\ln(K_4) \tag{5.12}$$

Since the reference electrode is in equilibrium with air and not pure oxygen equation 5.10 should be rewritten for the specific cell conditions.

$$E_{OCV} = E^0_{air} + \frac{RT}{F}\ln\left(\frac{a^{WE}_{FeO_{1.5}}}{a^{WE}_{FeO}}\right) \tag{5.13}$$

$$E^0_{air} = E_0 - \frac{RT}{F}\ln(P^{1/4}_{O_2,air}) = E_0 + 3.37x10^{-5}T \tag{5.14}$$

Use of the sensor in different environments might require the use of a different reference phase. Appendix H discusses the different possible gases and materials that could provide a suitable reference state and their deviation from the air reference. Appendix H

will be useful to the reader by providing a quick method for relating the potentials described within this thesis to other measurements available in the literature.

Equation 5.13 can be rewritten in order to relate the measured potential to the relative concentrations of each redox species.

$$E_{OCV} = E_{air}^{0'} + \frac{RT}{F}\ln\left(\frac{X_{FeO_{1.5}}^{WE}}{X_{FeO}^{WE}}\right) = E_{air}^{0'} + \frac{RT}{F}\ln(X_{rat}) \tag{5.15}$$

$E_{air}^{0'}$ is defined as the formal cell potential (equation 5.16).

$$E_{air}^{0'} = E_{air}^{0} + \frac{RT}{F}\ln\left(\frac{\gamma_{FeO_{1.5}}^{WE}}{\gamma_{FeO}^{WE}}\right) = E_{air}^{0} + \frac{RT}{F}\ln(\gamma_{rat}) \tag{5.16}$$

The formal cell potential will vary for different slag structures because γ_{rat} is heavily dependent on the underlying slag structure and electrolyte composition. If the γ_{rat} value for a given slag is known or can be estimated, equation 5.15 becomes a very powerful tool because the measured cell potential can then be directly related to the ratio of redox species within the slag.

Slags containing redox species other than FeOx would demonstrate the following generic reduction at the WE:

$$M^{x+} + ne^{-} = M^{(x-n)+} \tag{5.17}$$

Equations 5.18 and 5.19 describe the relationship between the measured cell potential and concentration ratio for slags containing a generic oxide species.

$$E_{OCV} = E_{air}^{0'} + \frac{RT}{F}\ln\left(\frac{X_{MO_{\left(\frac{x}{2}\right)}}^{WE}}{X_{MO_{\left(\frac{x-n}{2}\right)}}^{WE}}\right) \tag{5.18}$$

$E_{air}^{0'}$ is defined as the formal cell potential and is dependent upon the number of electrons transferred (n) in equation 5.17.

$$E_{air}^{0'} = E_{air}^{0} + \frac{RT}{F}\ln\left(\frac{\gamma_{MO_{\left(\frac{x}{2}\right)}}^{WE}}{\gamma_{MO_{\left(\frac{x-n}{2}\right)}}^{WE}}\right) = E_0 + 3.57x10^{-5}nT + \frac{RT}{F}\ln\left(\frac{\gamma_{MO_{\left(\frac{x}{2}\right)}}^{WE}}{\gamma_{MO_{\left(\frac{x-n}{2}\right)}}^{WE}}\right) \tag{5.19}$$

γ_{rat} values must be independently determined for each dissolved oxide species and is an empirically derived constant sensitive to the overall slag structure and basicity.

Under strongly reducing conditions metal oxide species such as Fe^{2+} or Si^{4+} may be reduced to their respective metallic form at the WE.

$$M^{n+} + ne^{-} = M^{0} \tag{5.20}$$

Equations 5.21 and 5.22 describe the appropriate relationship between the measured cell potential and metal oxide activity when the deposited metal demonstrates unit activity.

$$E_{OCV} = E_{air}^{0'} + \frac{RT}{F}\ln\left(X_{MO_{\left(\frac{n}{2}\right)}}^{WE}\right) \tag{5.21}$$

Under this condition, $E_{air}^{0'}$ is defined as the formal cell potential and is dependent upon the number of electrons transferred in equation 5.21 (n):

$$E_{air}^{0'} = E_{air}^{0} + \frac{RT}{F}\ln\left(\gamma_{MO_{\left(\frac{n}{2}\right)}}^{WE}\right) = E_0 + 3.57x10^{-5}nT + \frac{RT}{F}\ln\left(\gamma_{MO_{\left(\frac{n}{2}\right)}}^{WE}\right) \tag{5.22}$$

Note that under conditions where a pure metallic species is deposited at the working electrode there is a direct correlation between the measured cell potential and the activity of the oxide species in the slag (as opposed to a ratio of oxide species as in equation 5.18). As described in the Thesis Motivation section, this aspect has been utilized by the Quik-Slag sensor in order to develop an OCV technique for the detection of FeOx concentration under steelmaking conditions.

Figure 5.3 Electrochemical cell: Blow up of the WE region.

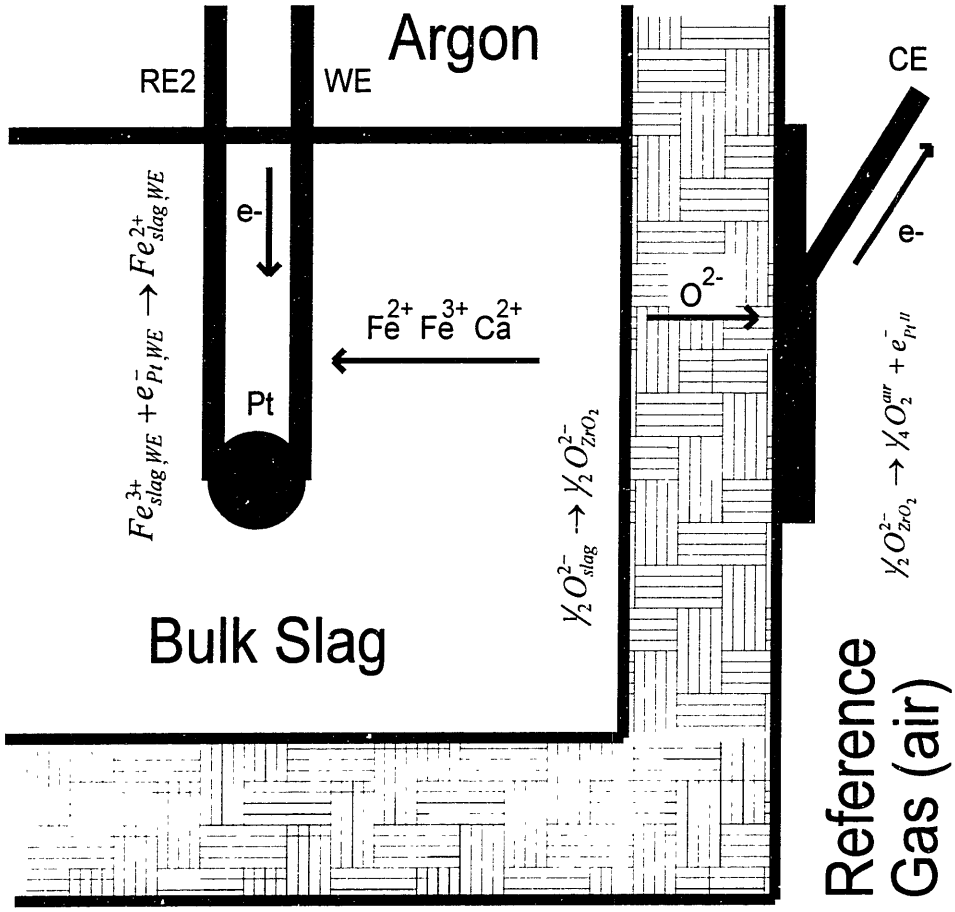

$$Pt_{(s)}\ |\ Fe^{3+}, Fe^{2+}, O^{2-}\ |\ O^{2-}\ |\ O_2, Pt_{(s)}$$
$$WE \qquad slag \qquad ZrO_2 \qquad air \qquad CE,RE$$

5.2.2 Applied DC Potential Step

This section describes the experimental theory behind the use of applied potential step techniques. The application of a potential step to an electrochemical cell can yield a wide variety of information on different cell properties depending upon the time scale under examination. Figure 5.4 demonstrates a generalized current response to an applied potential step as a function of time. Notice that the shape of the response differs over several different time regimes. At very small times (μsec), after the potential step is applied, the current is limited by capacitive charging of the double-layer at the slag/WE interface. At somewhat larger times (msec) the current will be predominantly limited by sluggish (irreversible) reaction kinetics. Finally, at long times (sec) the current will be limited by the transport of electro-active species to the interface by diffusional processes (reversible). Every electrochemical cell will demonstrate these three regimes. However, the appropriate time scales and degree of overlap between regimes will differ for each system. Each of the three regimes will be described in the following sections but greater focus should be given to the diffusional regime. Many textbooks have been written on this subject and can be referred to for a supplemental description[112,113].

5.2.2.1 Non-Faradaic: Double-Layer Capacitance

At very short times, the current response of an applied potential step is limited by the capacitive charging of the double-layer at the slag/WE interface. This regime can be described by equation 5.23.

$$i_{dl} = \frac{E_{app} - E_{ocv}}{R_{sol}} \exp\left(\frac{-t}{\tau_{dl}}\right) \tag{5.23}$$

E_{app} = Applied potential (V), E_{ocv} = initial cell potential, t = time after applied potential (sec), R_{sol} = solution resistance of the cell (Ω), i_{dl} = double-layer charging current (A), and τ_{dl} = time constant for double-layer charging (sec).

$$\tau_{dl} = R_{sol} C_{dl} \tag{5.24}$$

C_{dl} = double layer capacitance (F/cm^2)

Using equation 5.23 at small time scales, investigators[114] have found that the C_{dl} for slag systems is often significantly greater than the 10-40μF/cm² found in aqueous chemistry. Double-layer capacities greater than 100μF/cm² have been reported[115] in many slag systems and CaO-SiO_2 based systems[116] have been found to range from 150-300uF/cm² over the intermediate redox potential range of oxidation states (-0.8V to 0.2V relative to air). Even larger capacitances have been observed during the reduction of Si and the oxidation of O_2 gas[116].

After approximately 2 to 4 double-layer time constants (τ_{dl}) the charging current most likely becomes negligible compared with the current limited by charge-transfer kinetics which are described in the following section. The time constant (τ_{dl}) expected for the investigated cell is approximately 80 microseconds assuming R_{sol} of 5 Ω, C_{dl} of 200 uF/cm², and a surface area of 0.08 cm². Therefore, the time scale relevant for double-layer charging is expected to be considerably smaller than the 1-120 seconds examined in this thesis and can therefore be ignored for the DC applied potential experiments.

5.2.2.2 Faradaic Limitations

Charge transfer and diffusional limitations both rely on faradaic processes and are linked by an overall equation describing the influence of both factors as a function of the cell overpotential (η).

$$i = i_0\left[\frac{C_O}{C_O^{bulk}}\exp(-\alpha n f\eta) - \frac{C_R}{C_R^{bulk}}\exp((1-\alpha)nf\eta)\right] \tag{5.25a}$$

$$f = \frac{F}{RT} \tag{5.25b}$$

for the cell reaction:

$$O + ne^- \Leftrightarrow R \tag{5.25c}$$

Where: i_0 = exchange current density (A/cm^2), α = transfer coefficient, n = electrons in reaction, η = overpotential, C_R = concentration of reductant at the surface and bulk ($moles/cm^3$), C_O = concentration of oxidant at the surface and bulk.

The exchange current density (i_0) and the exponential terms describe the rate kinetics whereas the interfacial concentration terms describe the influence of diffusion on the faradaic current. Equation 5.25 is often split into three regimes for simplicity; charge transfer limited, mixed limitation, and diffusion limited. These three regimes are now discussed.

5.2.2.2.1 Charge Transfer Limitation

For very short time regimes the rate kinetics associated with the interfacial reaction will be significantly less than processes associated with transport of the species

to the interface. Under such conditions the measured current can be described by the Butler-Volmer equation:

$$i = i_0[\exp(-\alpha n f \eta) - \exp((1-\alpha) n f \eta)] \tag{5.26}$$

Equation 5.26 accurately describes the system until the current is approximately 10% of the diffusion-limited current[117]. The exchange current density (i_0) can be related to the reaction rate coefficient k by equation 5.27.

$$i_0 = nFk_R C_O^{(1-\alpha)} C_R^{\alpha} \tag{5.27}$$

Typically, a value for the exchange current density (i_0) can be determined by sampling the measured current for several different overpotentials and then extrapolating the results on a Tafel plot[113].

The exchange currents for metal-slag reactions at elevated temperatures have been found to be very rapid. Values range from 30-130 mA/cm^2 for CaO-SiO_2 slags at 1500-1600°C[116] to 140-650 mA/cm^2 for CaO-SiO_2-Al_2O_3 slags at 1350-1550°C[118] for the oxygen reaction shown in equation 5.28.

$$2O^{2-} = O_2^{2-} + 2e \tag{5.28}$$

Values ranged from 2-10A/cm^2 for low FeOx containing slags[119] in a CaF_2 melt at 1450°C for the iron reduction shown in equation 5.29.

$$Fe^{2+} + 2e^- = Fe \tag{5.29}$$

The reaction of the redox couple Fe^{3+}/Fe^{2+} is also expected to be quite rapid because of the high temperatures (1470°C) utilized in this thesis. Because of the rapidity of the charge transfer limitation, previous researchers found difficulty resolving exchange current data from both double-layer and diffusional responses[116,120].

5.2.2.2.2 Mixed Limitation

When both charge transfer and diffusion limitations must both be considered, equation 5.25 becomes quite complex but has been solved in Vetter[121] for an applied potential step to an electrode with planar geometry as follows:

$$i = i(0)\exp\left[\lambda^2 t\right] erfc\left[\lambda\sqrt{t}\right] \tag{5.30}$$

$$\lambda = \frac{i_0}{zF}\left(\frac{1}{C_R^{bulk}\sqrt{D_R}}\exp\left(\frac{\alpha zF}{RT}\eta\right) + \frac{1}{C_O^{bulk}\sqrt{D_O}}\exp\left(\frac{-(1-\alpha)zF}{RT}\eta\right)\right) \tag{5.31}$$

$$i(0) = i_0\left(\exp\left(\frac{\alpha zF}{RT}\eta\right) + \exp\left(\frac{-(1-\alpha)zF}{RT}\eta\right)\right) \tag{5.32}$$

where:

$$O + ne^- = R \tag{5.32a}$$

Emi et al.[116] found that the measured current was primarily diffusion limited as early as 100ms. Similar time scales are expected for the current investigation and therefore further discussion of the utilization of equations 5.30-5.32 for extracting relevant data is not pursued in this thesis.

5.2.2.2.3 Diffusion Limitation

At significantly long times, i_0 is significantly larger than the total current and equation 5.25 can be rewritten as equation 5.33.

$$E = E^{0'} + \frac{RT}{nF}\ln\left(\frac{C_O^{app}}{C_R^{app}}\right) \tag{5.33}$$

The electrode potential and the surface concentrations of O and R are then linked by an equation of Nernst form. The current flowing under this condition is no longer

determined directly from equation 5.25 (or 5.33) but is determined by the diffusive motion of faradaic species from the bulk to the surface. Equation 5.34 describes the diffusional response to an applied potential step of a system consisting of a generic redox reaction. The derivation of equation 5.34 may be found in Appendix I.

$$i(t) = \frac{(n_O - n_R)FA\left(C_O^{bulk} - \theta C_R^{bulk}\right)}{(1+\xi\theta)}\sqrt{\frac{D_O}{t\pi}} \tag{5.34a}$$

$$\theta = \frac{C_O^{app}}{C_R^{app}} = \exp\left(\frac{nF}{RT}\left(E_{app} - E_0\right)\right) \tag{5.34b}$$

$$\xi = \sqrt{\frac{D_O}{D_R}} \tag{5.34c}$$

Note that both the diffusion of oxidant towards the electrode and diffusion of reductant away from the electrode may act to limit the measured cell current. The measured current magnitude will be a function of the diffusion coefficients, the type of oxide present, the initial oxidation state, and the applied potential.

Figure 5.4 Generalized current response to an applied DC potential Step.

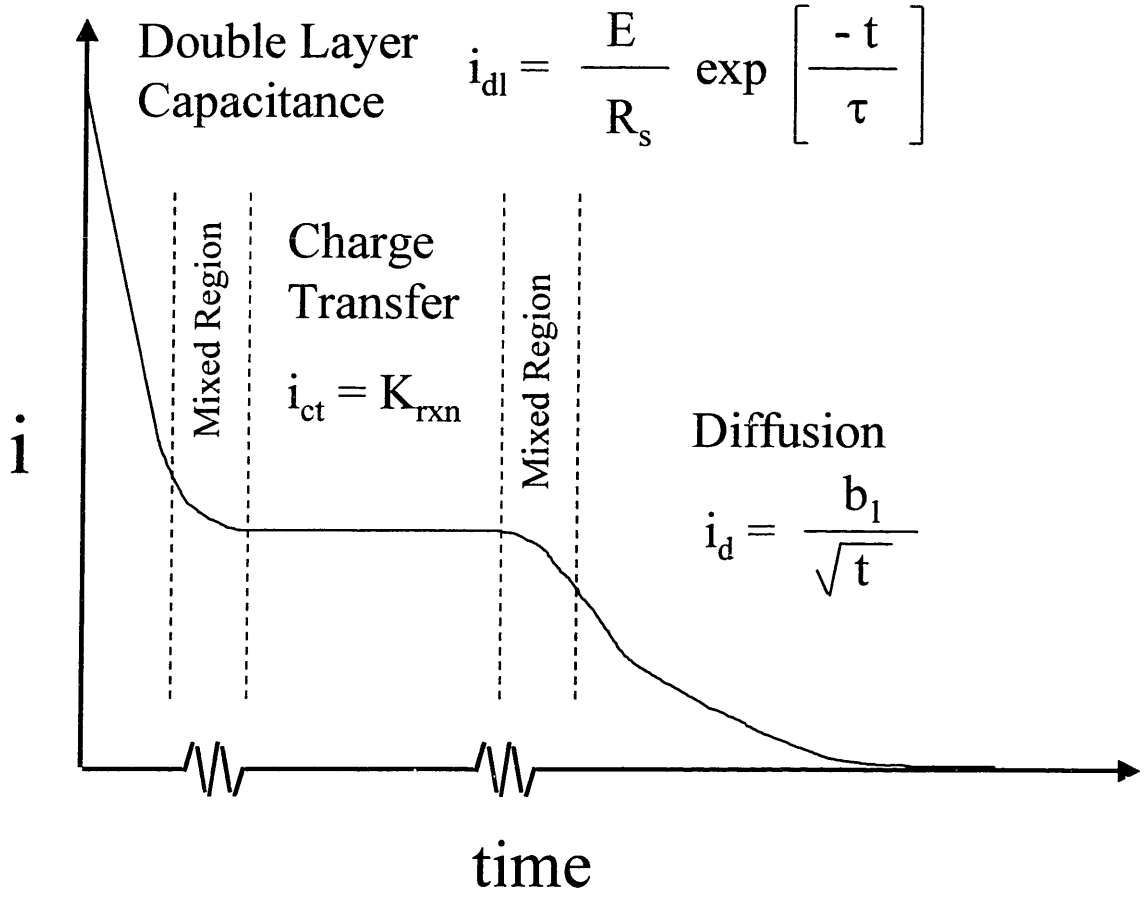

5.2.3 Impedance

Experimental techniques involving impedance provide a useful means for determining many important properties of an electrochemical cell. Impedance measurements rely upon the development of a stable steady state condition as opposed to the violent transient established during an applied potential step measurement. This allows the investigator more precise control over the operating environment. For example, by superimposing an AC waveform on top of a stable DC applied potential (controlled by a potentiostat) the concentration ratio of redox species can be established at the WE/slag interface as described by equation 5.33 (shown in 5.35).

$$E = E^{0'} + \frac{RT}{nF}\ln\left(\frac{C_O^{app}}{C_R^{app}}\right) \tag{5.35}$$

In this manner several different slag conditions can be examined without running additional experiments. Impedance measurements are often characterized by the use of an equivalent circuit which attempts to describe the underlying reactions occurring within the electrochemical cell as linear (albeit sometimes frequency dependent) elements. Quantification of these elements is then obtained by applying complex non-linear least squared fitting analysis (CNLS) of the raw data to the proposed equivalent circuit.

The following sections will describe the fundamentals behind the use of impedance, develop an appropriate equivalent circuit for the electrochemical cell used in the thesis, and describe the expected frequency regimes which may be encountered during application.

5.2.3.1 Fundamentals of Impedance

Impedance techniques rely upon the relationship between the application (equation 5.36) and steady-state response (equation 5.38) of an alternating signal applied to the electrochemical cell.

$$v(t) = V_m \sin(\omega t) \tag{5.36}$$

$$f = \frac{\omega}{2\pi} \tag{5.37}$$

f = frequency (Hz), ω = angular frequency (rad-Hz), V_m = AC peak voltage (V), and v(t) = AC signal (V).

$$i(t) = I_m \sin(\omega t - \theta) \tag{5.38}$$

θ = phase angle of offset (radians), I_m = AC peak current (A), i(t) = AC signal (A).

Under steady state conditions equations 5.36 and 5.38 are related by the impedance (Z), a frequency dependent parameter.

$$Z(\omega) = \frac{v(t)}{i(t)} \tag{5.39}$$

In order to ensure linearity and the viability of equation 5.39, Macdonald[122] has shown that the amplitude of the AC potential waveform must be less than the thermal voltage of the cell.

$$V_m < \frac{RT}{F} \tag{5.40}$$

The V_m value of 10mV used in this thesis is well below the threshold established in equation 5.40 and therefore linearity is realized in the cell. After steady state is achieved, the frequency (ω) of the current and voltage portions of the impedance will be identical.

The impedance can then be rewritten as a simple complex vector in rectangular coordinates.

$$Z = Z' + jZ'' \tag{5.41}$$

$$Z' = |Z|\cos(\theta) \tag{5.42}$$

$$Z'' = |Z|\sin(\theta) \tag{5.43}$$

$$|Z| = \left((Z')^2 + (Z'')^2\right)^{1/2} \tag{5.44}$$

$$\theta = \tan^{-1}\left(\frac{Z''}{Z'}\right) \tag{5.45}$$

Z' = Real impedance (Ω), Z'' = Complex impedance (Ω), $|Z|$ = Magnitude of the impedance (Ω), and θ = phase angle (radians).

This can be translated into polar coordinate notation (equation 5.46) by using the Euler relation (equation 5.47).

$$Z(\omega) = |Z|\exp(j\theta) \tag{5.46}$$

$$\exp(j\theta) = \cos(\theta) + j\sin(\theta) \tag{5.47}$$

Using equations 5.46 and 5.47, equation 5.38 can be rewritten as equation 5.48.

$$i(t) = \frac{V_m}{|Z|}\sin(\omega t - \theta) \tag{5.48}$$

By examining how the impedance magnitude and phase angle of the resulting current vary with applied frequency for various cell conditions, a large quantity of information concerning different properties of the cell can be obtained by comparison with an appropriate equivalent circuit. The next section will develop such a circuit and describe the different frequency regimes that might be expected.

5.2.3.2 Equivalent Circuit

Figure 5.5 represents the proposed equivalent circuit for the complete electrochemical cell. The impedance associated with many of the circuit components in figure 5.5 is expected to be quite small because of surface area considerations, therefore figure 5.6 represents a simplified equivalent circuit focused on the WE/slag interface where the majority of the impedance is expected to occur. R_{sol} represents the bulk resistance of the slag electrolyte, C_{dl} represents the double-layer capacitance at the working electrode, R_{ct} represents the charge transfer resistance of the reaction, and R_W and C_W represent the influence of diffusion limitation to the working electrode and are frequency dependent elements. The overall impedance of the circuit found in figure 5.6 can be described by equation 5.49.

$$Z(s) = R_{sol} + \frac{\left(R_{CT} + R_W + 1/C_{W} s\right) 1/C_{DL} s}{1/C_{DL} s + R_{CT} + R_W + 1/C_{W} s} \tag{5.49}$$

The Warburg[123] impedance elements R_W and C_W are frequency dependent elements and are associated with the semi-infinite steady-state diffusional flow of redox species at the WE surface under oscillating conditions. This Warburg impedance can be described by the following constant phase element equation:

$$Z_W = \sigma_W (1 - j)\omega^{-1/2} = R_W - \frac{j}{\omega C_W} \tag{5.50}$$

$$\sigma_W = \frac{RT}{n^2 F^2 A\sqrt{2}} \left(\frac{1}{D_O^{1/2} C_O^{WE}} + \frac{1}{D_R^{1/2} C_R^{WE}} \right) \tag{5.51}$$

$$O + ne^- = R \tag{5.52}$$

A complete derivation of the Warburg impedance equation can be found in Bard and Faulkner[124].

R_W and C_W defined in equations 5.53 and 5.54.

$$R_W = \frac{\sigma}{\omega^{1/2}} \tag{5.53}$$

$$C_W = \frac{1}{\sigma\omega^{1/2}} \tag{5.54}$$

Manipulating equations 5.49, 5.53, and 5.54 the real and imaginary parts of the overall impedance are defined in equations 5.55 and 5.56.

$$Z' = R_{sol} + \frac{R_{CT} + \sigma\omega^{-1/2}}{\left(1 + C_{DL}\sigma\omega^{1/2}\right)^2 + \omega^2 C_{DL}^2\left(R_{CT} + \sigma\omega^{-1/2}\right)^2} \tag{5.55}$$

$$Z'' = \frac{\omega C_{DL}\left(R_{CT} + \sigma\omega^{-1/2}\right)^2 + \sigma\omega^{-1/2}\left(1 + C_{DL}\sigma\omega^{1/2}\right)}{\left(1 + C_{DL}\sigma\omega^{1/2}\right)^2 + \omega^2 C_{DL}^2\left(R_{CT} + \sigma\omega^{-1/2}\right)^2} \tag{5.56}$$

At high frequencies the real portion of the impedance associated with the WE structure will approach zero as the double-layer acts as a short circuit. Equation 5.55 can then be simplified to equation 5.57.

$$Z'_{HF} = R_{sol} \tag{5.57}$$

A Nyquist impedance plot demonstrating the behavior of equation 5.57 is shown in figure 5.7 and consists only of a point on the real axis representing R_{sol}. High frequency (HF) measurements can be used to determine the resistance of the electrolyte between the RE and WE. If the current path within the system is known then the conductivity of the slag electrolyte phase can be calculated. This approach will be utilized in order to estimate the conductivity of the slag phase and compare it with literature data. The methods for doing this are discussed in greater detail in Appendix F.

For very low frequencies the real and imaginary portions of the impedance will be dominated by the Warburg diffusional processes occurring at the WE/slag interface as shown by equations 5.58 and 5.59.

$$Z'_{LF} = R_{sol} + R_{CT} + \sigma\omega^{-1/2} \tag{5.58}$$

$$Z''_{LF} = 2\sigma^2 C_{DL} + \sigma\omega^{-1/2} \tag{5.59}$$

Therefore, σ_W can be quickly estimated by plotting the slope of Z' or Z'' against $\omega^{-1/2}$ as shown in equation 5.60.

$$\frac{dZ''_{LF}}{d\omega^{-1/2}} = \frac{dZ'_{LF}}{d\omega^{-1/2}} = \sigma \tag{5.60}$$

A Warburg diffusional response would generate a constant phase element (CPE) with unit slope in a Nyquist plot as shown in figure 5.8.

At intermediate frequencies the real and imaginary portions of the impedance may be dominated completely or partially by the charge transfer reaction as shown in equations 5.61 and 5.62.

$$Z'_{CT} = R_{sol} + \frac{R_{CT}}{\left(1 + \omega^2 C_{DL}^2 R_{CT}^2\right)} \tag{5.61}$$

$$Z''_{CT} = \frac{\omega C_{DL} R_{CT}^2}{\left(1 + \omega^2 C_{DL}^2 R_{CT}^2\right)} \tag{5.62}$$

This response would generate a semi-circle in a Nyquist plot (figure 5.9) which can be used to define both R_{ct} and C_{dl} values.

By sweeping the frequency and measuring the resulting changes in the magnitude and phase of the current, important information concerning different properties of the slag phase can be obtained from the different frequency regimes as described above. Furthermore, by superimposing a DC applied potential on top of the AC signal the

relative concentrations of redox species can be altered thereby influencing the magnitude of the Warburg impedance (equation 5.51). Although a rough approximation of each of the cell parameters can be computed as described above, more exact data can be recovered by utilizing complex non-linear least squared (CNLS) fitting techniques. Further discussion of the CNLS fitting technique and the methods employed in this thesis is described in more detail in Appendix J.

The reader should note that the different frequency regimes occurring for the impedance measurement correspond closely with the different time regimes described in the DC applied potential step technique. This is quite convenient from an experimental viewpoint because the two techniques complement each other very well. Impedance techniques require the achievement of steady-state conditions for a proper measurement following the approach described above. Measurements conducted at long times in the purely diffusional regime during a potential step measurement would be very difficult to achieve a proper steady-state-impedance measurement due to the low frequencies required. Conversely, DC techniques rely on real-time measurements which increase the difficulty of taking measurements on a short time scale. For this reason, impedance methods were utilized to characterize the response for short times (<1sec) whereas the DC methods were used to characterize the phenomena at long times (>1sec).

Figure 5.5 Proposed equivalent circuit describing the entire electrochemical cell.

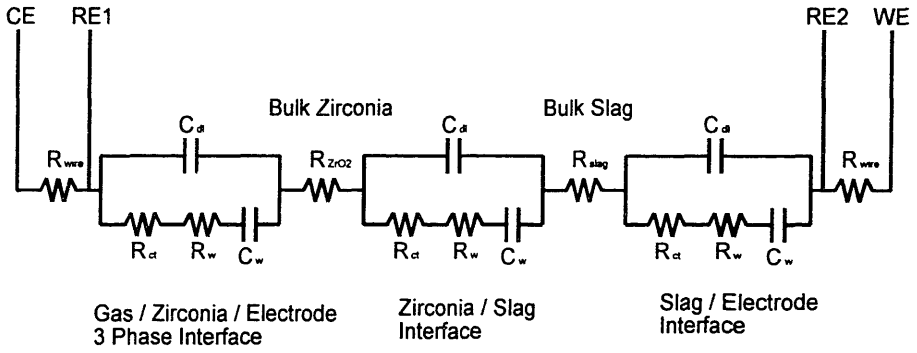

Figure 5.6 Proposed equivalent circuit describing the relevant elements of the electrochemical cell.

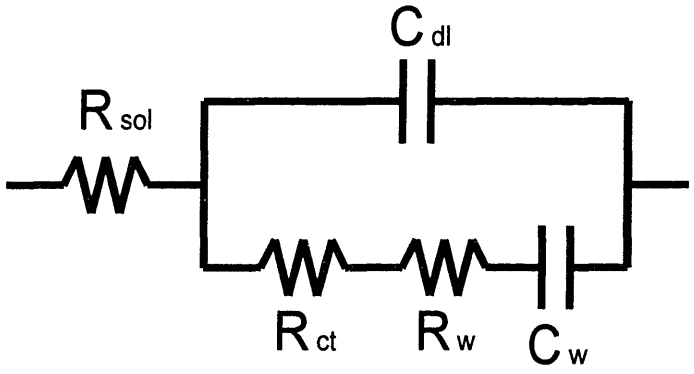

Figure 5.7 Nyquist Plot – Rsol (HF).

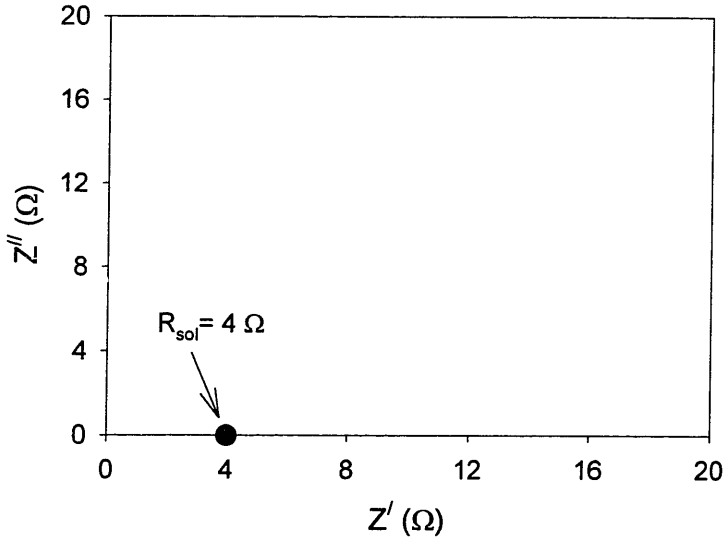

Figure 5.8 Nyquist Plot – Warburg element (LF).

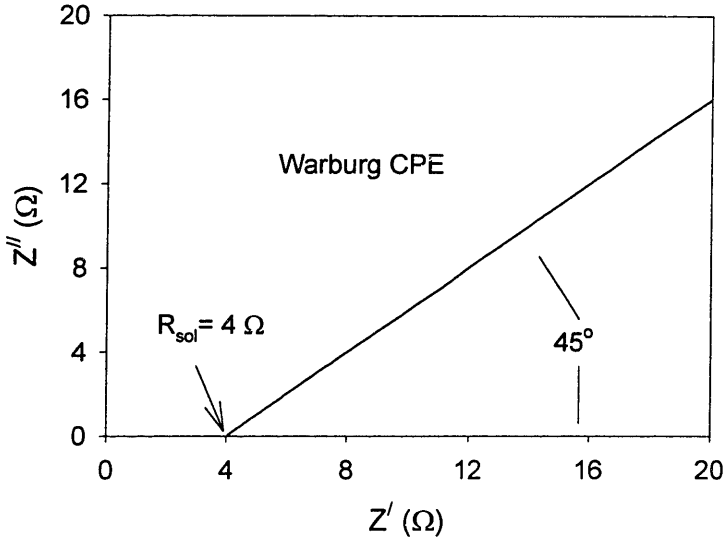

Figure 5.9 Nyquist Plot – R_{ct}, C_{dl} (intermediate).

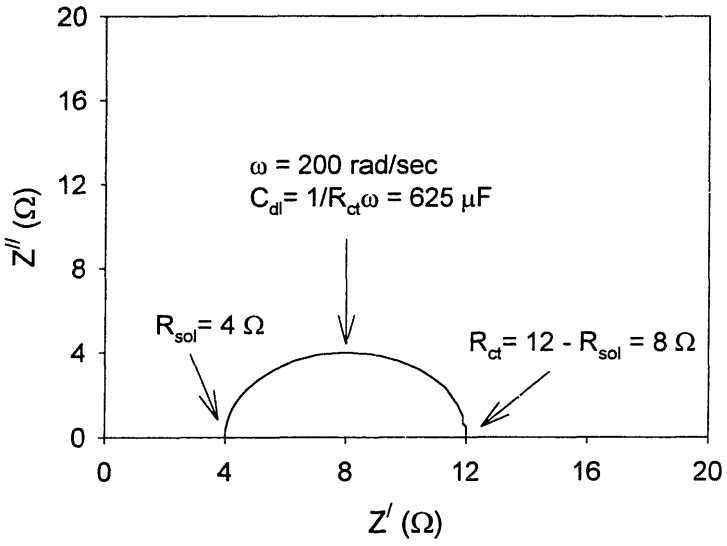

5.3 Results and Discussion

The following results and discussion section describes the results obtained using the experimental setup (figure 5.1) for low FeOx containing slags. The data analysis flow chart (figure 5.10) describes an outline for the analysis and utilization of data measured in this thesis. The same flow chart can be used by investigators interested in utilizing similar devices for measuring data in industrial or academic settings. For a known slag composition and temperature, raw data was obtained from the sensor in the following forms: open circuit potential (OCV), DC potential step, and impedance frequency sweep with applied DC potential.

Thermodynamic modeling of OCV measurements was used to obtain the oxygen activity of the slag. This measurement was used to simulate data which might be recorded using a conventional oxygen sensor or other open circuit measurement device.

Thermodynamic and kinetic modeling of the current time response for a DC potential step was used to obtain information sensitive to the concentration and transport properties of dissociable solute oxides within the slag.

Equivalent circuit modeling of impedance frequency sweep data was used to yield meaningful electrochemical cell parameters such as the cell resistance, double layer capacitance, charge-transfer resistance, and diffusional impedance. Appropriate modeling was then utilized to link these parameters to information concerning the concentration and transport properties of dissociable solute oxides within the slag.

The purpose of this thesis was to demonstrate the benefits which might be obtained by utilizing amperometric methods. Therefore, the following subsections examine various parameters of the slag such as solute oxide concentration, solute oxide

type, solvent viscosity, and transport estimation and then discuss how additional information was gained by using amperometric techniques.

5.3.1 Concentration Influence

5.3.1.1 Introduction

The ability to measure a parameter which is directly sensitive to the concentration of solute oxide is one of the main goals of this thesis. OCV measurements do not provide a direct method for measuring concentration because they are only sensitive to the oxygen activity. The following subsections examine how amperometric methods such as potential step and impedance provide parameters which are sensitive to FeOx concentration under conditions which the OCV technique may be inadequate.

5.3.1.2 Open Circuit Potential (OCV)

Figure 5.11 demonstrates the influence of concentration on the initial OCV for the high viscosity slags ranging from 0 to 4 wt%FeOx. Notice that the OCV appears to be relatively independent of the total FeOx concentration. The OCV measurement simulates the results which might be obtained by using a conventional oxygen sensor. The measurement is purely thermodynamic in nature and only provides information concerning the oxygen activity of the slag phase as described by the Nernst equation:

$$E_{OCV} = \frac{-RT}{F} \ln \left(\frac{P_{O_2^{air}}^{1/4}}{P_{O_2^{slag}}^{1/4}} \right) \tag{5.63}$$

Equation 5.63 can be rewritten as described in the experimental theory section as follows:

$$E_{OCV} = E^0_{air} - \frac{RT}{F}\ln\left(\frac{X^{WE}_{FeO}}{X^{WE}_{FeO_{1.5}}}\right) - \frac{RT}{F}\ln\left(\frac{\gamma^{WE}_{FeO}}{\gamma^{WE}_{FeO_{1.5}}}\right) = E^0_{air} + \frac{RT}{F}\ln(X_{rat}) + \frac{RT}{F}\ln(\gamma_{rat}) \quad (5.64)$$

Notice that the open circuit potential is sensitive to the relative concentrations of each half of the redox couple but NOT directly sensitive to the total concentration of FeOx within the slag. This explains the apparent independence of OCV and total FeOx concentration in figure 5.11. In theory, the slag structure could be influenced by FeOx concentration which would alter the γ_{rat} value in equation 5.64. However, this influence is NOT expected to be significant in this investigation because FeOx is a relatively minor constituent of the overall slag structure[125].

The slags examined in this thesis were intentionally prepared in an identical manner as described in the slag characterization section in order that they display similar oxygen activities. Unfortunately, the OCV measurements for the lower FeOx containing slags (0 and 0.5 wt%FeOx) demonstrated slightly lower OCV values. This is likely due to degassing of oxygen from the slag to the Argon gas phase. Slags containing lower concentrations of FeOx would display a lower buffering capacity to a given oxidation state and hence be more sensitive to degassing of oxygen.

The slags investigated in this thesis intentionally contained similar oxygen activities in order to demonstrate the inherent deficiency associated with a conventional oxygen sensor. Because the conventional oxygen sensor yields results which are only thermodynamic in nature it does not yield information concerning the concentration of various oxide species or the buffering capacity of the slag to a given oxidation state. In future sections, use of amperometric techniques such as applied DC potential and

impedance frequency sweeps will demonstrate sensitivity of these techniques to the concentration of FeOx in addition to the oxygen activity thereby providing more information concerning the slag phase.

5.3.1.3 DC Potential Step

5.3.1.3.1 Raw data

Figure 5.12 demonstrates the current-time response behavior of applied potential steps for 2 wt%FeOx containing slag. Similar responses were obtained for other wt%FeOx concentrations for the high viscosity slag compositions. The data demonstrate a linear relationship to $t^{-1/2}$ which is indicative of a diffusion limited response as discussed in the experimental theory section. The current-time response at any given applied potential can be completely characterized by equation 5.65:

$$i_{tot} = b_0 + b_1/\sqrt{t} \tag{5.65}$$

b_0 = steady state current (long times)

b_1 = diffusional current (ficks' second law)

Table 5.2 records the calculated b_0 and b_1 values for each of the DC potential step experiments for high viscosity slags in this thesis. These two parameters completely describe the results obtained during such measurements.

5.3.1.3.2 Significance of b0

The parameter b_0 is related to the steady-state current at long times and can be described by equation 5.66:

$$b_0 = b_{cyl} + b_{rxn} + b_{bl} \tag{5.66}$$

b_{cyl} = apparent steady-state current due to cylindrical coordinate geometry

b_{rxn} = steady-state current due to a constant reaction at the electrode surface

b_{bl} = steady-state current due to diffusion across a boundary layer

These three topics (b_{bl}, b_{cyl}, b_{rxn}) are considered in more detail in Appendix L. However, because b_0 is sensitive to parameters which involve cell geometry, gas composition, and boundary layer thickness, b_0 is not reliable for use as a general sensing parameter for FeOx concentration and is therefore not discussed further in this thesis.

5.3.1.3.3 Significance of b1

As described in the experimental theory section, b_1 is directly sensitive to the diffusive parameters of the cell:

$$i(t) = \frac{b_1}{\sqrt{t}} = \frac{FA\left(C^B_{Fe^{3+}} - \theta_{app} C^B_{Fe^{2+}}\right)}{\left(1 + \xi\theta_{app}\right)} \sqrt{\frac{D_{Fe^{3+}}}{t\pi}} \tag{5.67a}$$

where:

$$\theta_{app} = \frac{C^{surface}_{Fe^{3+}}}{C^{surface}_{Fe^{2+}}} = \exp\left(\frac{nF}{RT}\left(E_{app} - E_0'\right)\right) = X_{rat,app} \tag{5.67b}$$

$$\xi = \sqrt{\frac{D_{Fe^{3+}}}{D_{Fe^{2+}}}} \tag{5.67c}$$

Equation 5.67a can be rewritten as follows:

$$i(t) = \frac{b_1}{\sqrt{t}} = \frac{FA(\theta_{ocv} - \theta_{app})C_{Fe_{tot}}}{(1+\xi\theta_{app})(1+\theta_{ocv})}\sqrt{\frac{D_{Fe^{3+}}}{t\pi}} \tag{5.68a}$$

$$\theta_{ocv} = \frac{C^{bulk}_{Fe^{3+}}}{C^{bulk}_{Fe^{2+}}} = \exp\left(\frac{nF}{RT}\left(E_{ocv} - E_0'\right)\right) = X_{rat,ocv} \tag{5.68b}$$

Equation 5.68a demonstrates that b_1 will be sensitive to a wide number of different parameters including the diffusion coefficient of each redox species (D_{Fe3+}, D_{Fe2+}), the initial and final redox concentration ratio (θ_{ocv}, θ_{app}), and the total concentration of FeOx in the slag (C_{Fetot}). The concentration influence section investigates the ability of b_1 to act as a sensing parameter for the total concentration of FeOx in the slag. In order to demonstrate this sensitivity, the other parameters of equation 5.67a were intentionally held constant. The D_{Fe3+} and D_{Fe2+} values remained unchanged with variation in FeOx content because the slag structure was not significantly altered by minute changes in FeOx concentration[125]. The final redox concentration ratio, $X_{rat,app}$, is defined by the applied DC potential which was held constant for each of the slag compositions (-0.2V, -0.4V, -0.6V, -0.8V). The initial concentration ratio, $X_{rat,ocv}$, is defined by the initial OCV which was approximately the same value (prior to any given applied potential) for each slag composition.

Figures 5.13a-d demonstrate the experimentally determined linearity between the area standardized b_1 values and the total FeOx concentration in the slag. Whereas a conventional oxygen sensor was incapable of determining any difference between the five different slag compositions because of their identical oxygen activity, use of a DC potential step clearly identified differences in the FeOx composition. The difference in slope between figures 5.13a-d was caused by differences in the initial OCV and the applied DC potential. As described above, these values control the initial and final

surface concentration ratios of Fe^{3+}/Fe^{2+}, X_{rat}, in equation 5.68a. If the slag concentration and thermodynamics is well known, the transport properties of Fe^{3+} and Fe^{2+} in the slag structure can be estimated. This will be described in further detail in the determination of transport properties section of the thesis.

5.3.1.4 Impedance

5.3.1.4.1 Raw data

Figure 5.14 demonstrates a Nyquist plot of a typical impedance frequency sweep at an applied DC potential for a high viscosity low FeOx containing slag. Using CNLS fitting techniques described in Appendix J, values for R_{sol}, C_{dl}, R_{ct}, and σ_W were determined for each impedance frequency sweep and can be found in Table 5.3. Each of the four parameters are sensitive to the concentration of FeOx and will be evaluated independently in the following sections for use as possible sensing parameter.

5.3.1.4.2 Solution Resistance

As described in the experimental theory section, at high frequencies the real part of the impedance would be expected to approach the solution resistance of the cell:

$$Z' = R_{sol} \tag{5.69}$$

Equation 5.70 was derived in Appendix F for the cell geometry used in this thesis and relates R_{sol} to the slag conductivity:

$$R_{sol} = R_{ZrO_2} + R_{Slag} = \frac{X_{wire}}{2\pi h_{wire}}\left(\frac{\ln\left(\frac{r_{ID}}{r_{wire}}\right)}{\sigma_{slag}} + \frac{\ln\left(\frac{r_{OD}}{r_{ID}}\right)}{\sigma_{ZrO_2}}\right) \tag{5.70}$$

Where: r_{wire} is the WE Pt wire radius (cm), r_{ID} is the ID of the ZrO_2 tube (see table 5.1) (cm), r_{OD} is the OD of the ZrO_2 tube (see table 5.1) (cm), σ_{slag} is the slag conductivity (Ω^{-1}-cm^{-1}), σ_{ZrO2} is the Zirconia conductivity (Ω^{-1}-cm^{-1}), h_{wire} is the immersion depth of the wire (cm), X_{wire} is a coefficient related to the number of wires immersed into the slag, R_{sol} is the solution resistance (Ω), R_{ZrO_2} is the resistance due ZrO_2 (Ω), and R_{slag} is the resistance due slag phase (Ω).

As was described in the slag characterization section, slag conductivity should be sensitive to the FeOx concentration because iron cations act as mobile charge carriers in an ionic melt:

$$\sigma_{tot} = \sum_i \sigma_i \tag{5.71a}$$

$$\sigma_{Fe} = 2F\mu_{Fe^{2+}}C_{Fe^{2+}} + 3F\mu_{Fe^{3+}}C_{Fe^{3+}} \tag{5.71b}$$

In general, increases in the FeOx concentration should lead to increases in slag conductivity.

Figure 5.15 compares the measured slag conductivities calculated using equation 5.70 with predicted values from the literature as described in the slag characterization section[126,127]. The measured values were consistently larger than the predicted values which can be attributed to imperfect centering of the WE and end-effects at the WE tip. These errors are described in more detail in Appendix F and might be expected because the sensor was not designed specifically for conductivity measurements. A slight increase in slag conductivity was measured with increasing FeOx concentration. However, the relative sensitivity of slag conductivity to the concentration of FeOx is minor over the concentration range investigated as shown in equation 5.72.

$$Sensitivity = \frac{\left(\frac{d\sigma}{dwt\%}\right)}{\sigma_{(2wt\%)}} = \frac{0.006153}{0.12709} = 0.0484 \qquad (5.72)$$

Where: Sensitivity is in units of 1/wt%, σ is the conductivity at 2wt% (regression line), and dσ/dwt% is the change in conductivity with wt%.

The low sensitivity of the conduction parameter to the FeOx concentration in this concentration range causes difficulty in resolving concentration effects from geometry induced error effects present in the cell design. For example, the standard deviation of the data from the regression line was calculated to be 0.00579, which is of the same magnitude as the $\left(\frac{d\sigma}{dwt\%}\right)$ term.

Although slag conductivity was shown to be sensitive to the FeOx concentration, the sensitivity of this parameter to FeOx concentration is relatively small. Therefore, errors associated with cell geometry uncertainties will likely overwhelm this relationship. This would be especially problematic under industrial settings. For this reason slag conductivity is not considered a realistic sensing parameter for changes in low FeOx concentrations for oxide melts. A more detailed description of the sensitivity of concentration to different parameters can be found in Appendix K.

5.3.1.4.3 Double-Layer Capacitance

Values of double-layer capacitance in slag systems have been found to be relatively large as compared with those found in aqueous chemistry. Previous investigators have found that the double-layer capacitance increases with increasing FeOx concentration because iron cations adsorb on the slag side of the double-layer[128,129] decreasing the multilayer thickness[130]. Takahashi et al.[131] showed that the

C_{dl} at platinum-slag interfaces is considerably larger than the C_{dl} found at an iron electrode. The literature has demonstrated that significant variation of C_{dl} can occur with concentration, slag structure, oxygen potential, and electrode material.

Analysis of the data recovered in this thesis did not show any conclusive relationship between C_{dl} and FeOx concentration. This may be due to geometrical variations between each of the experiments and emphasizes the difficulty in using C_{dl} as a sensing parameter.

5.3.1.4.4 Charge-Transfer Resistance

The charge transfer resistance would be expected to be a function of the concentration of the species undergoing the electrochemical reaction as shown by the equation 5.73:

$$i_0 = nFk_r C_{Fe^{3+}}^{(1-\alpha)} C_{Fe^{2+}}^{\alpha} \tag{5.73}$$

However, at the high temperatures investigated in this thesis the charge transfer resistance was found to be relatively minor in comparison with polarization due to the diffusional impedance (table 5.2). The small values measured for R_{ct}, and the overlap of R_{ct} with C_{dl} and σ_W data at high frequencies made accurate resolution rather difficult. Other researchers have had similar problems obtaining accurate results for this parameter because of the low values of R_{ct} under similar conditions[130]. In this thesis, the charge transfer resistance was found to be approximately 0.5 ohms and not very sensitive to FeOx concentration or applied potential. The error associated with determining R_{ct} using CNLS fitting was rather large emphasizing the difficulty in determining this parameter.

5.3.1.4.5 Diffusional Impedance

As described in the experimental theory section, σ_W describes the diffusional impedance of the cell assuming a Warburg impedance element of the form:

$$Z_W = \sigma_W (1 - j)\omega^{-1/2} \tag{5.74}$$

$$\sigma_W = \frac{RT}{n^2 F^2 A\sqrt{2}}\left(\frac{1}{D_{Fe^{3+}}^{1/2} C_{Fe^{3+}}^{WE}} + \frac{1}{D_{Fe^{2+}}^{1/2} C_{Fe^{2+}}^{WE}}\right) \tag{5.75}$$

As can be seen from equation 5.74 the Warburg impedance would be expected to dominate at low frequencies. However, because of the low value of R_{ct}, σ_W dominates even at relatively large frequencies.

Figure 5.16 demonstrates the relationship between σ_W and the applied potential (E_{app}) for a given FeOx concentration. For all slags containing FeOx a U shaped graph was obtained. The applied DC potential determines the FeOx redox equilibrium at the WE interface is described by equation 5.76:

$$E_{App} = E_{air}^{0'} - \frac{RT}{F}\ln\left(\frac{X_{FeO}^{WE}}{X_{FeO_{1.5}}^{WE}}\right) \tag{5.76}$$

Low applied potentials result in a low concentration of Fe^{2+} which yields a large σ_W value as predicted by equation 5.75. Similarly, large applied potentials result in a low concentration of Fe^{3+} which again yields a large σ_W value. A σ_W minima will be located at intermediate potentials. The modeled curve in figure 5.16 was constructed in the Estimating Transport Properties section by assigning appropriate values to the diffusion coefficients and combining equations 5.75 and 5.76. The value for σ_W deviates from the model at very large applied potentials (>-0.8V) because the equivalent circuit proposed in the experimental theory section (figure 5.6) is no longer appropriate. At large potentials,

other competing reactions involving the reduction of Fe^{2+} and Si^{4+} compete with the redox reaction of FeOx. Further discussion of this phenomena can be found in the Solvent influence section.

Equation 5.77 predicts that σ_W will be inversely proportional to the total concentration of FeOx if the slag structure and transport properties are held constant.

$$\sigma_W = \frac{RT}{n^2F^2A\sqrt{2D_{Fe^{3+}}}C_{FeO_X}}\left(2+\frac{1}{\xi\theta}+\xi\theta\right) \tag{5.77a}$$

$$\theta = \frac{C_{Fe^{3+}}}{C_{Fe^{2+}}} = \exp\left(\frac{nF}{RT}(E_{DC}-E_0)\right) \tag{5.77b}$$

$$\xi = \sqrt{\frac{D_{Fe^{3+}}}{D_{Fe^{2+}}}} \tag{5.77c}$$

Figures 5.17a-d demonstrate the experimentally determined linearity between the area standardized σ_W values and the inverse of the total FeOx concentration at several different applied potentials. Therefore, σ_W can be used as a sensing parameter for FeOx concentration if the slag structure and transport properties are well known.

5.3.1.5 Summary

Figures 5.11, 5.13b, 5.15, and 5.17c summarize the results obtained in the concentration influence section. Figure 5.11 demonstrates the inability of conventional OCV technique to determine the difference between the five different FeOx containing slags. This is because the slags had very similar oxygen activities. Figure 5.15 demonstrates that conductivity measurements using high frequency impedance are slightly better than OCV measurements for detecting FeOx concentration differences.

However, the sensitivity of conductivity to low FeOx concentrations is relatively small and can be easily be overshadowed by geometrical uncertainties. Figures 5.13b and 5.17c demonstrate the strong correlation between the b_l and σ_W parameters using potential step and impedance techniques and the total concentration of FeOx with the slag. The above results conclusively show that amperometric methods can yield improvements over information obtained using the OCV technique alone. Further discussion of the implementation of such techniques for industrial settings can be found in the future work and applications section.

Table 5.2 Results of DC applied potential step.

Name	Hi/Low viscosity	wt%FeOx	Area	DC applied potential	OCV	b0	b1
pap15	H	0.5	0.087776	-0.2	-0.0899	-2.49E-05	-3.21E-04
				-0.4	-0.114	-9.23E-05	-1.28E-03
				-0.6	-0.2019	-2.00E-04	-1.83E-03
				-0.8	-0.2374	-3.43E-04	-2.64E-03
pap14	H	4	0.175552	-0.2	-0.0514	-3.00E-04	-6.44E-03
				-0.4	-0.096	-7.77E-04	-0.01652
				-0.6	-0.154	-1.41E-03	-0.0282
				-0.8	-0.2572	-2.78E-03	-0.03685
				-1	-0.3447	-4.96E-03	-0.039575
pap13	H	2	0.087776	-0.2	-0.027	-7.72E-05	-1.77E-03
				-0.4	-0.0768	-2.14E-04	-4.86E-03
				-0.6	-0.19	-4.42E-04	-7.18E-03
				-0.8	-0.2965	-7.05E-04	-8.15E-03
				-1	-0.3654	-2.03E-03	-9.72E-03
pap12	H	0	0.175552	-0.2	-0.1561	-1.28E-05	-5.25E-05
				-0.4	-0.1591	-6.68E-05	-3.86E-04
				-0.6	-0.18	-1.39E-04	-7.57E-04
				-0.8	-0.2169	-3.03E-04	-1.34E-03
				-1	-0.2955	-7.42E-03	-4.48E-03
pap10	H	2	0.175552	-0.2	-0.0444	-1.46E-04	-2.81E-03
				-0.4	-0.0934	-3.82E-04	-8.21E-03
				-0.6	-0.1894	-8.12E-04	-0.0136
				-0.8	-0.2963	-1.40E-03	-0.0166
				-1	-0.3783	-2.64E-03	-0.0212
pap8	H	1	0.143634	-0.2	-0.091	-6.11E-05	-0.000958
				-0.4	-0.0865	-2.12E-04	-0.004232
				-0.6	-0.1921	-4.35E-04	-0.006553
				-0.8	-0.2846	-7.42E-04	-0.007729
				-1	-0.3836	-4.64E-03	-0.0355
pap7	L	4	0.175552	-0.8	-0.0918	-3.46E-03	-0.04876
				-1	-0.3049	-5.07E-03	-0.0544
pap6	L	4	0.143634	-0.2	-0.0988	-2.32E-04	-0.003945
				-0.4	-0.1289	-9.67E-04	-0.01314
				-0.6	-0.1801	-1.76E-03	-0.0223
				-0.8	-0.2435	-2.88E-03	-0.0299
				-1	-0.3087	-4.20E-03	-0.0373
pap5	L	2	0.175552	-0.2	-0.0919	-9.14E-05	-0.002056
				-0.4	-0.1178	-0.000486	-0.00751
				-0.6	-0.1613	-0.0011	-0.0125
				-0.8	-2.10E-01	-0.001599	-0.0168
				-1	-2.66E-01	-0.00222	-0.02365
pap2	L	1	0.175552	-0.2	-0.1025	-0.000088	-0.001
				-0.4	-0.1197	-0.00039	-0.0044
				-0.6	-0.1841	-0.00086	-0.0078
				-0.8	-0.3321	-0.0017	-0.01
				-1	-0.3813	-0.002	-0.014

Table 5.3 Results of CNLS fitting procedure for impedance frequency sweeps.

Name	Hi/Low viscosity	wt%FeOx	Area	DC applied potential	R_{sol}	R_{ct}	C_{dl}	σ_W
pap15	H	0.5	0.087776	-0.0876	6.452	0.401	32.75	150.77
				-0.2	6.511	0.436	41.71	97.73
				-0.4	6.604	0.49	54.56	61.49
				-0.6	6.639	1.783	37.77	187.56
				-0.8	6.56	0.498	86.2	83.58
				-1	6.401	0.1509	450	1.77
pap14	H	4	0.175552	-0.0518	3.92	0.55	54	11.86
				-0.2	3.905	0.546	65.7	9.18
				-0.4	3.873	0.599	64.52	7.07
				-0.6	3.832	0.633	64.64	6.81
				-0.8	3.748	0.725	55.5	10.49
				-1	3.65	0.597	46	16.84
pap13	H	2	0.087776	-0.0306	5.839	0.6995	79.7	48.77
				-0.2	5.859	0.627	116	30.09
				-0.4	5.863	0.5819	158	20.20
				-0.6	5.906	0.728	108	33.35
				-0.8	5.917	1.763	98.98	87.62
				-1	5.83	0.358	292	6.55
pap12	H	0	0.175552	-0.1561	5.023	0	3.70E-05	312.00
				-0.2	5.023	0	3.20E-05	272.00
				-0.4	5.061	0.998	2.97E-05	172.00
				-0.6	5.075	0	2.88E-05	278.00
				-0.8	5.032	0.587	1.03E-04	44.20
pap10	H	2	0.175552	-0.0386	4.169	0.56	92	28.86
				-0.2	4.166	0.516	108	22.29
				-0.4	4.149	0.469	132	15.13
				-0.6	4.101	0.4975	110	18.16
				-0.8	4.11	0.6193	97.17	39.08
				-1	4.069	0.4194	204	8.94
pap8	H	1	0.143634	-0.088	5.022	0.436	94.55	50.87
				-0.2	5.044	0.377	115	38.43
				-0.4	5.079	0.248	167	21.08
				-0.6	5.088	0.4274	105	37.22
				-0.8	5.07	0.5038	127	67.34
				-1	4.971	0.09	766	1.34
pap7	L	4	0.175552	-0.0788	2.098	0.139	537	9.94
				-0.814	2.194	0.145	456	9.25
				-1.02	2.288	0.1427	372	18.07
pap6	L	4	0.143634	-0.0873	3.237	0.296	189	13.22
				-0.2	3.36	0.262	237	9.65
				-0.4	3.564	0.256	291	7.82
				-0.6	3.812	0.279	298	7.96
				-0.8	4.06	0.359	240	10.98
pap5	L	2	0.175552	-0.0875	3.445	0.2813	109	26.72
				-0.2	3.581	0.2321	133	17.68
				-0.4	3.734	0.2165	174	11.73
				-0.6	3.993	0.32578	159	15.41
				-0.8	4.336	1	110	37.41
				-1	4.535	0.409	191	21.79
pap2	L	1	0.175552	-0.0963	3.069	0.33677	95	3.07
				-0.4	3.439	0.2683	177	3.44
				-0.6	3.593	0.4215	141	3.59
				-0.8	3.91	1.192	102	3.91
				-1	4.207	0.4275	250	4.21

Figure 5.10 Data analysis flow chart. Slags with different compositions are examined using three different measurement techniques, OCV, DC applied potential step, and impedance frequency sweep at an applied DC potential. The raw data obtained using the three techniques are modeled using appropriate thermodynamic and kinetic models in order to gain information on the oxygen activity, MOx concentration, MOx type, and transport property information.

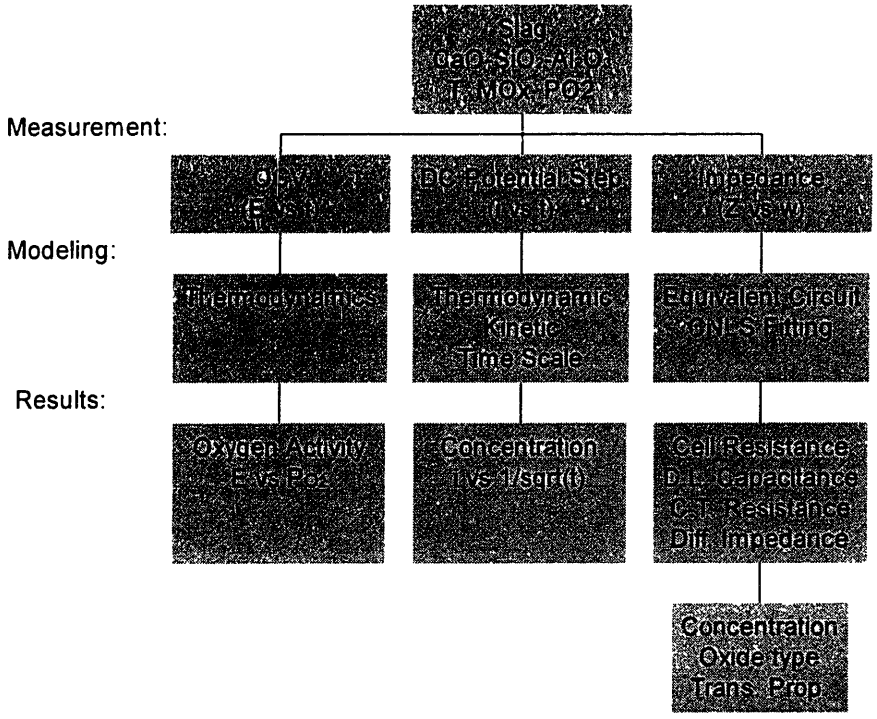

Figure 5.11 OCV vs wt%FeOx. H slags at 1470°C. No correlation was obtained between the measured OCV and the wt%FeOx.

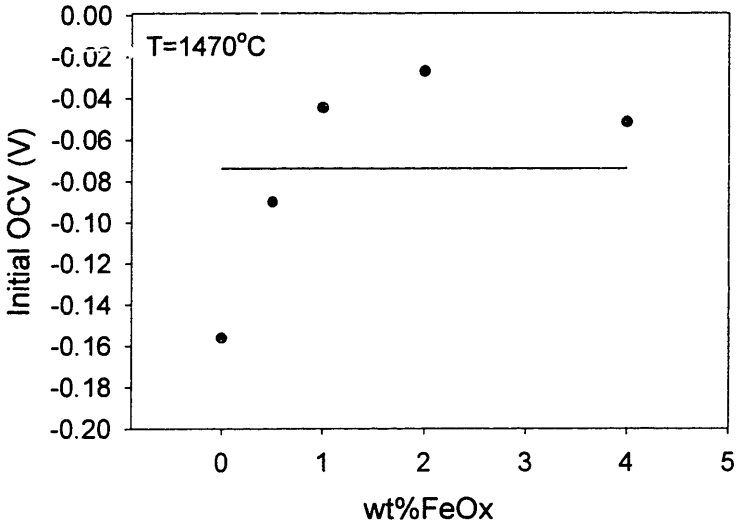

Figure 5.12 i-V response for DC applied potential steps for 2wt% FeOx H type slag. The response demonstrated decreasing currents with time and appeared diffusional in nature.

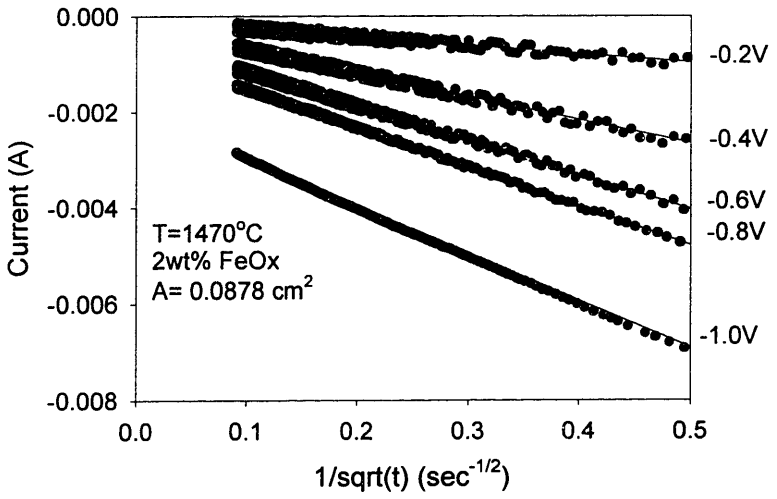

Figure 5.13a -0.2V DC potential step b_1/A vs wt%FeOx H type slags. The parameter b_1/A demonstrated sensitivity to the wt%FeOx in H type slags.

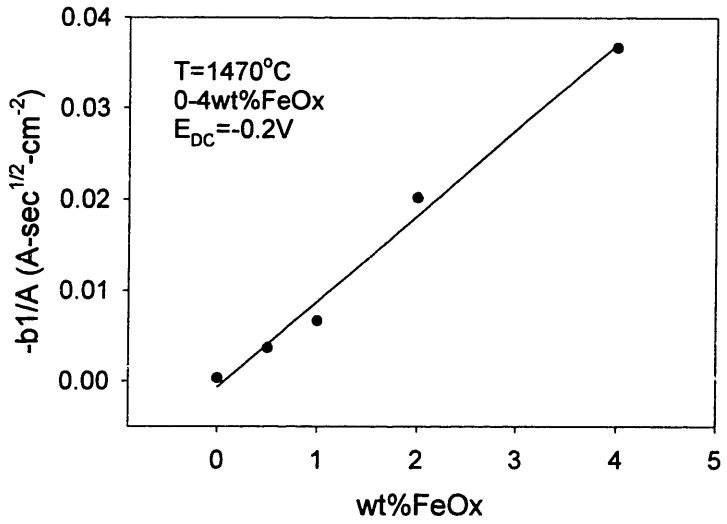

Figure 5.13b -0.4V DC potential step b_1/A vs wt%FeOx H type slags. The parameter b_1/A demonstrated sensitivity to the wt%FeOx in H type slags.

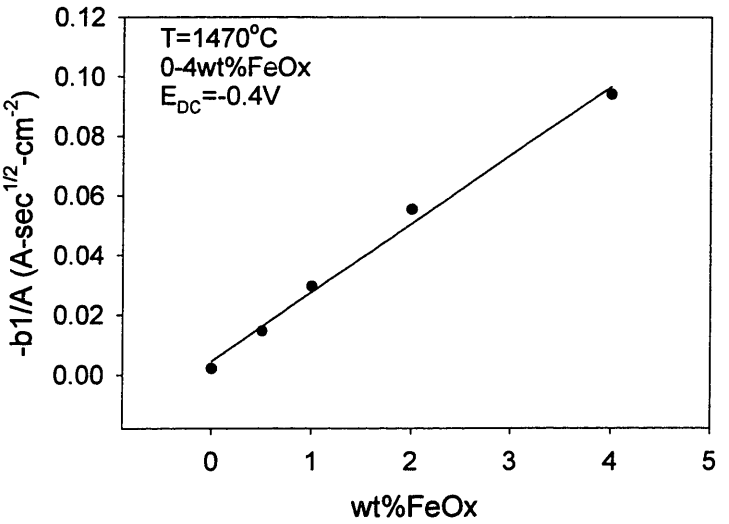

Figure 5.13c -0.6V potential step b_1/A vs wt%FeOx for H type slags. The parameter b_1/A demonstrated sensitivity to the wt%FeOx in H type slags.

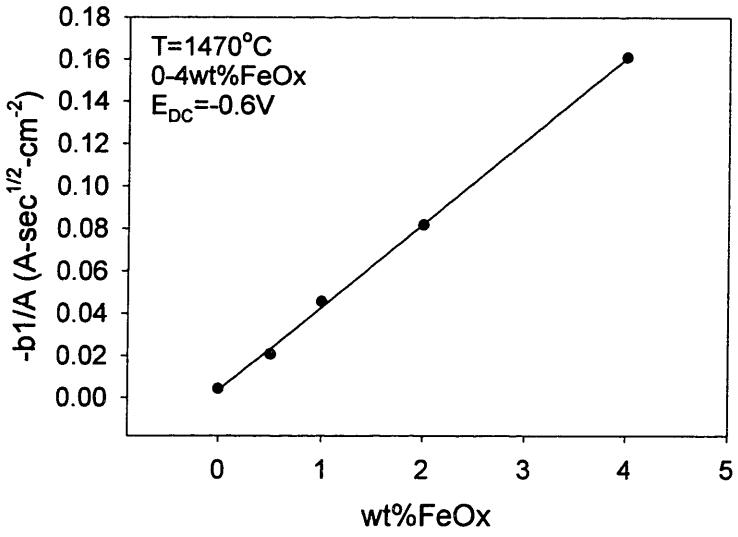

Figure 5.13d -0.8V DC potential step b_1/A vs wt%FeOx H type slags. The parameter b_1/A demonstrated sensitivity to the wt%FeOx in H type slags.

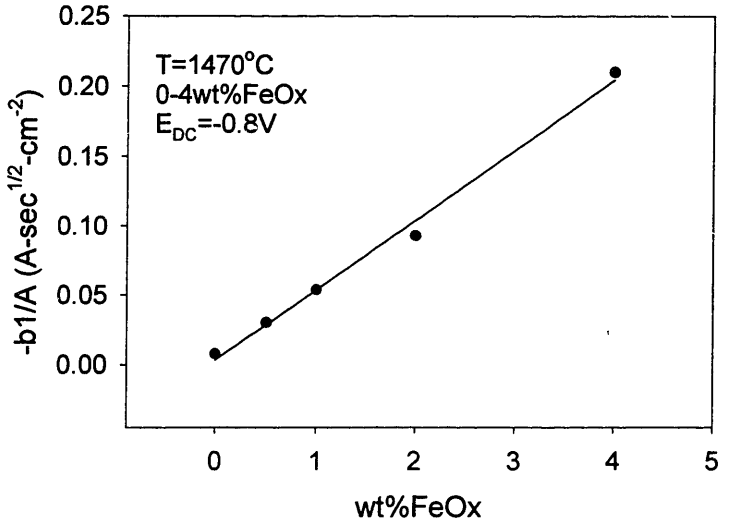

Figure 5.14 Impedance Frequency Sweep (Nyquist Plot), 2wt%FeOx H type slag. Using CNLS fitting routines and the equivalent circuit found in figure 5.6 the raw data was converted to useful cell parameters such as R_{sol}, C_{dl}, R_{ct}, and σ_W.

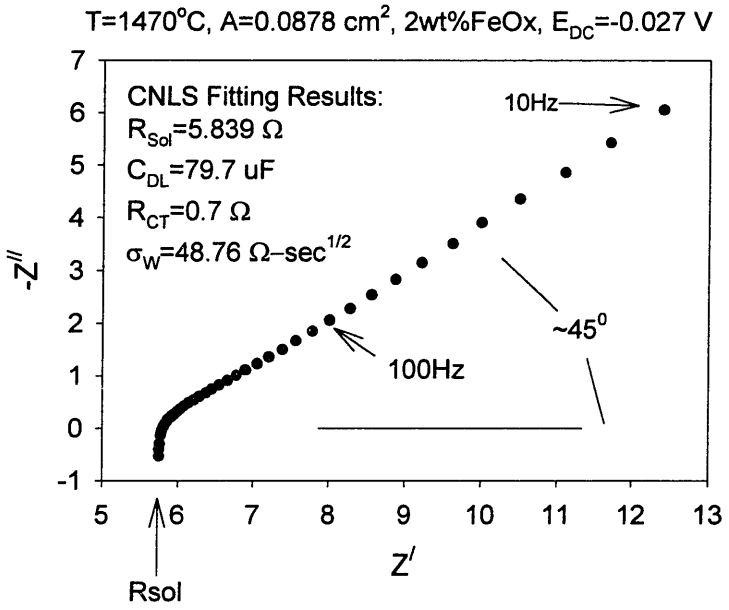

Figure 5.15 Slag conductivity vs wt%FeOx H type slags. Slag conductivity demonstrated only slight sensitivity to the wt%FeOx in the slag. The conductivity measurements for the slags in this thesis compared well with estimated data from the literature[126,127].

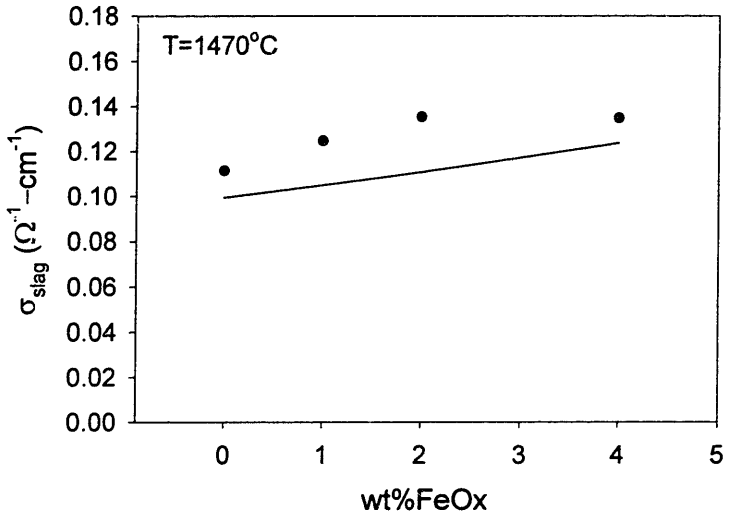

Figure 5.16 σ_W vs Eapp for 2wt% FeOx H type slag. The σ_W data demonstrated a U-shaped behavior with applied DC potential. This corresponded well with the model generated in transport properties determination section.

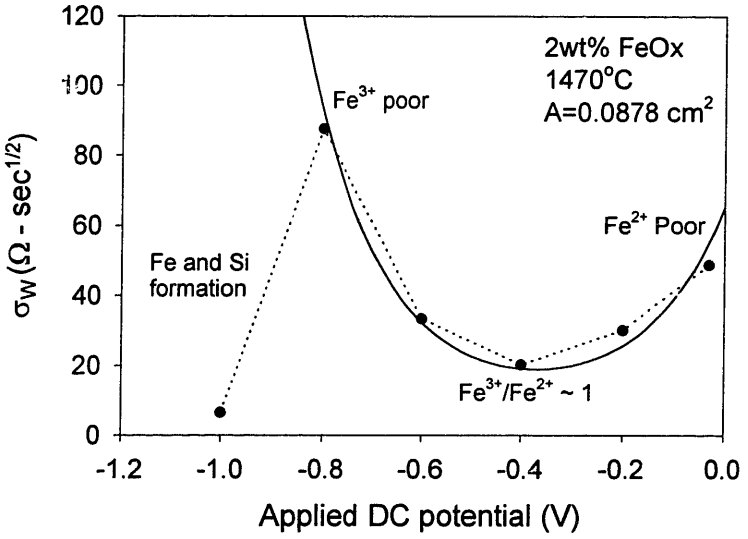

Figure 5.17a $\sigma_W A$ vs wt%FeOx at OCV for H type slags. The parameter $\sigma_W A$ demonstrated sensitivity to the wt%FeOx in H type slags.

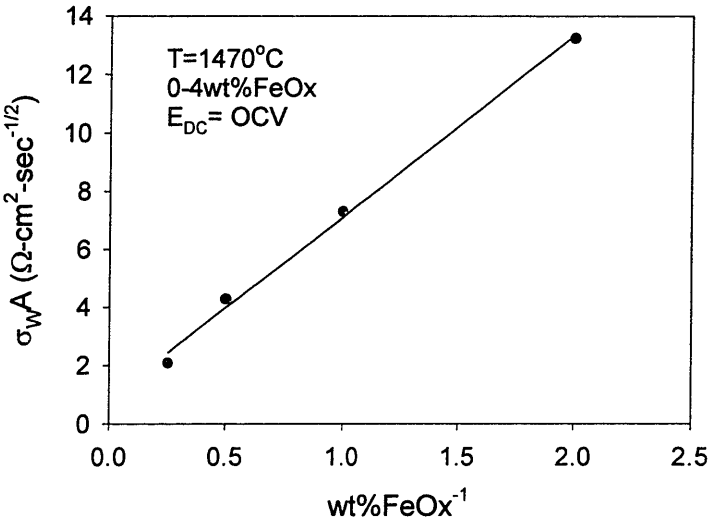

Figure 5.17b $\sigma_W A$ vs FeOx at -0.2V for H type slags. The parameter $\sigma_W A$ demonstrated sensitivity to the wt%FeOx in H type slags.

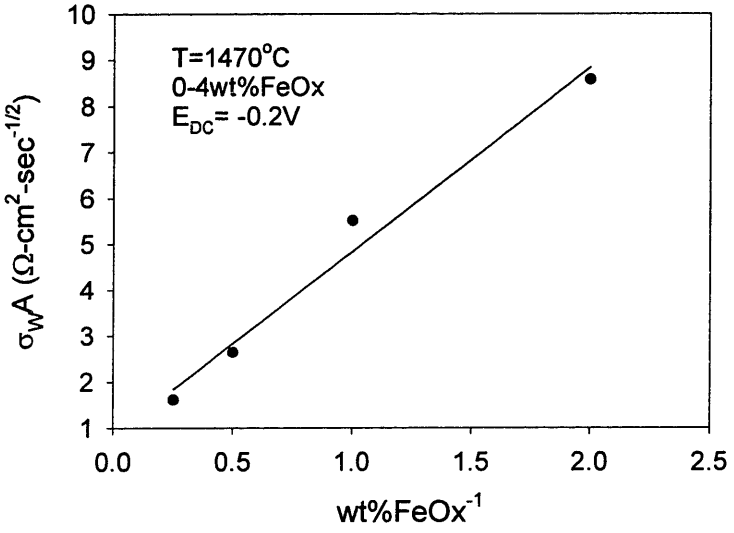

Figure 5.17c $\sigma_W A$ vs FeOx at -0.4V for H type slags. The parameter $\sigma_W A$ demonstrated sensitivity to the wt%FeOx in H type slags.

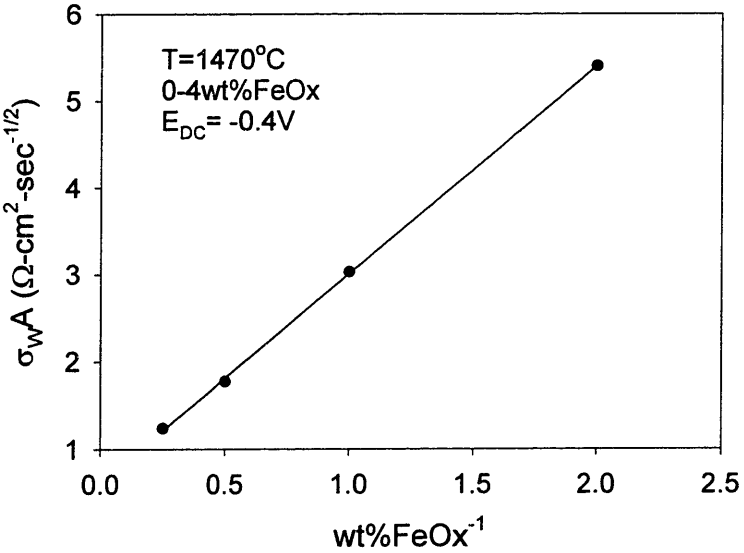

Figure 5.17d $\sigma_W A$ vs FeOx at -0.6V for H type slags. The parameter $\sigma_W A$ demonstrated sensitivity to the wt%FeOx in H type slags.

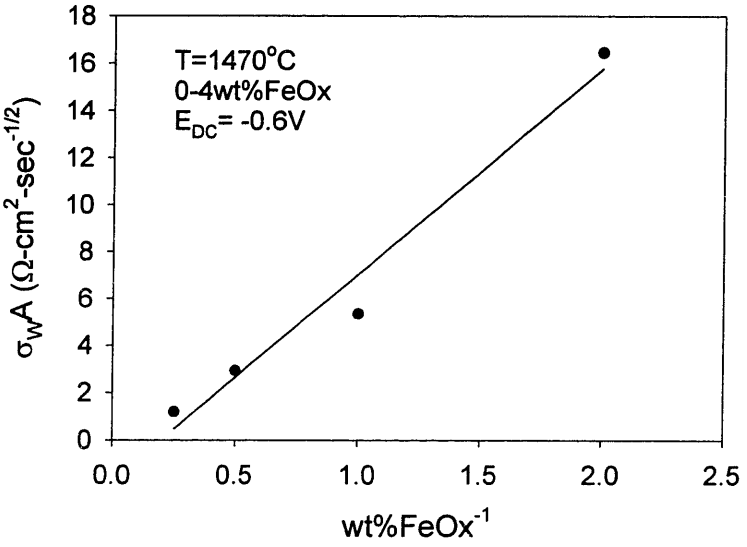

5.3.2 Viscosity Influence

5.3.2.1 Introduction

Two different solvent slag compositions were examined in order to investigate the ability of amperometric measurements to resolve variations in slag structure. The compositions investigated were chosen such that the viscosities would differ by a factor of 2 at 1500°C (figure 3.17a)[132]. There is a strong link between slag viscosity and cationic diffusion coefficients as given by the Stokes-Einstein relationship.

$$D_i = \frac{kT}{6\pi r_i \eta}\left(\frac{\delta \ln a_i}{\delta \ln c_i}\right) \approx \frac{kT}{6\pi r_i \eta} \tag{5.78}$$

Since amperometric measurements are sensitive to the transport properties of the oxide species, slag structure differences are detectable using DC potential step and impedance techniques. This is in contrast to a simple OCV measurement which can only detect differences in the oxidation state.

5.3.2.2 Area Standardization

Amperometric measurements rely strongly on accurate knowledge of the surface area of the working electrode. In general, the WE is lowered a known distance into the slag thereby fixing the WE surface area. HF impedance measurements were previously utilized to estimate the slag conductivity as described in the slag characterization section and Appendix F. Examination of R_{sol} values determined from HF impedance measurements can also be used to describe the stability of the system as a function of time. Figure 5.18 demonstrates the change in R_{sol} for a typical high and low viscosity

slag as measured during the duration of a complete experiment at temperature. Note that the R_{sol} value remains essentially constant for the high viscosity slag but steadily increases with time for the low viscosity slag. This is due to an interaction of the slag with the zirconia resulting in a slag level drop with time thereby reducing the effective WE surface area for low viscosity slags. This was confirmed by post-experimental analysis of the electrochemical cell where the ZrO_2 tube for low viscosity slags appears swollen whereas the ZrO_2 tube for high viscosity slags appears unchanged. Increased corrosion of ZrO_2 by the low viscosity slag was likely induced by its more rapid transport properties and higher basicity.

In order to compare the two different slag structures a method for estimating the WE surface area as a function of R_{sol} for low viscosity slags was developed in Appendix F. Values of R_{sol} were obtained at several immersion depths and then used to calibrate the R_{sol} value with the WE surface area. The surface area values for the low viscosity slags in the potential step and impedance sections are standardized values calculated using the technique in Appendix F.

The difficulties experienced in controlling the WE surface area of the low viscosity slags exemplify the experimental challenges associated with conducting high temperature measurements over long periods of time on systems containing reactive phases. All of slags investigated in this thesis intentionally focused on structures demonstrating relatively high viscosity (4-15 poise) in order to ensure that the system would remain relatively stable over a time frame of hours as opposed to minutes. Under industrial conditions the viscosity is expected to be considerably lower (<1 poise) as the basicity of metallurgical melts is generally quite high. While such conditions will

inevitably lower the useful "lifetime" of the sensor, information can still be obtained on the order of minutes as will be described in the Industrial Application section.

5.3.2.3 OCV Measurement

Figure 5.19 compares the initial OCV of the two different slag structures. The low viscosity slags appear to be slightly lower than the high viscosity slags on average. As described previously, the OCV measurement is mainly an indication of the oxygen activity as shown in equation 5.79.

$$E_{OCV} = \frac{-RT}{F} \ln\left(\frac{P_{O_2^{air}}^{1/4}}{P_{O_2^{slag}}^{1/4}}\right) \tag{5.79}$$

Therefore we would not have expected any influence of slag structure on the OCV because the slags were created under identical oxygen atmospheres. Equation 5.80 shows that slag structure γ_{rat} would have an effect on the OCV value if X_{rat} remains constant.

$$E_{OCV} = E_{air}^{0} + \frac{RT}{F}\ln(X_{rat}) + \frac{RT}{F}\ln(\gamma_{rat}) \tag{5.80}$$

However, slag processing would not have ensured that X_{rat} remains constant and the difference of γ_{rat} term between the two slags investigated was estimated to be no larger than -0.06V (γ_{rat} of 1.2 vs 1.8) as described in the slag characterization section. Equation 5.78 demonstrated that more rapid transport properties are associated with lower viscosity slags. Faster transport properties for the lower viscosity slag may have resulted in more rapid degassing of oxygen and a faster equilibration with the Argon phase. Therefore, the results found in figure 5.19 are most easily attributed to a secondary effect related to the

equilibration of the slag with the Argon than with the ability of OCV measurements to detect slag structure.

It should be noted that if the X_{rat} of a particular slag was known with certainty, an OCV measurement would become useful as a measure for slag structure. However, this would generally require an auxiliary measurement or sampling technique and would therefore be most typically known with less certainty than the slag structure. Further discussion on sampling implementation for industrial settings can be found in the future work and applications section.

5.3.2.4 DC Potential Step

Figure 5.20 compares the area standardized b_1 values for the low and high viscosity slags. Equation 5.78 demonstrates that lower diffusion coefficients would be expected for higher viscosity slags. Equation 5.68a indicates that b_1/A is expected to demonstrate the following proportionality with diffusivity and viscosity as shown in equation 5.81.

$$\left(\frac{b_1}{A}\right) \propto \sqrt{D_{Fe^{3+}}} \propto \frac{1}{\sqrt{\eta_{slag}}} \tag{5.81}$$

Since the high viscosity slag is approximately twice as viscous as the low viscosity slag we would expect equation 5.82 to hold:

$$\left(\frac{b_1}{A}\right)_{low} = \sqrt{2}\left(\frac{b_1}{A}\right)_{high} \tag{5.82}$$

The L type slag is modeled by the dotted line in figure 5.20 which was developed from the H type slag data assuming the validity of equation 5.81. The model appears to

correspond fairly well with the measured values of b_1/A for the L type slag. The relationship in equation 5.82 assumes that the OCV values prior to the application of potential step are identical. Part of the error between the low viscosity data and the modeled line exist because the OCV values are not identical. Table 5.4 describes the OCV values prior to applied potential step for each of the data points in figure 5.20. At low applied potentials the OCV values are more negative for the low viscosity curve while prior to large applied potentials the OCV values are less negative. If this effect were included in the model, the measured data would demonstrate even closer agreement to the modeled line as the line would move upwards at high applied potentials and downward at low applied potentials.

5.3.2.5 Impedance

Figure 5.21 compares the area standardized σ_W values for the low and high viscosity slags. Equation 5.77a indicates that $\sigma_W A$ is expected to demonstrate the following proportionality with diffusivity and viscosity as shown in equation 5.83.

$$\sigma_W A \propto \frac{1}{\sqrt{D_{Fe_{tot}}}} \propto \sqrt{\eta_{slag}} \tag{5.83}$$

Since the high viscosity slag is approximately twice as viscous as the low viscosity slag we would expect equation 5.84 to hold.

$$(\sigma_W A)_{low} = \frac{(\sigma_W A)_{high}}{\sqrt{2}} \tag{5.84}$$

The L type slag is modeled by the dotted line in figure 5.21 which was developed from the H type slag data assuming the validity of equation 5.83. The model appears to

correspond fairly well with the measured values of $\sigma_W A$ for the L type slag. Figure 5.21 more clearly demonstrates the difference between the two compositions because $\sigma_W A$ is independent of the initial OCV. Misfit between the modeled line and the low viscosity data points is partially accounted for by errors in the area standardization but is also partially caused by differences in slag structure between the two slags. Equation 5.85 describes the relationship between the location of the U shaped curve and the slag structure (γ_{rat}).

$$E_{1/2} = E^0_{air} + \frac{RT}{F}\left[\ln(X_{rat}) + \ln\left(\frac{1}{\sqrt{D_{rat}}}\right) + \ln(\gamma_{rat})\right] \tag{5.85}$$

As described in the slag characterization section γ_{rat} is expected to change from 1.8 to 1.2 for the high versus low viscosity slag. This would effectively shift the modeled line by –0.06V which would provide a better fit with the measured data.

5.3.2.6 High Frequency Impedance

As described in the Concentration Influence section, the R_{sol} value determined from the HF impedance measurement can be used to estimate a value of the slag conductivity using Appendix F. The FeOx concentration was found to only slightly influence the total conductivity over the concentration range of 0-4 wt%FeOx. Figure 5.22 demonstrates the influence of slag structure on the slag conductivity. Note that slag conductivity is an excellent indicator for changes in slag structure when the FeOx concentration is small. This is because slag conductivity for $CaO\text{-}Al_2O_3\text{-}SiO_2\text{-}FeOx$ is given by equation 5.86.

$$\sigma_{tot} = \sum_i \sigma_i = \sigma_{Fe_{tot}} + 2F\mu_{Ca^{2+}} C_{Ca^{2+}} \tag{5.86}$$

For low FeOx containing slags there is a direct relationship between σ_{tot} and the concentration and mobility of Ca^{2+} because σ_{Fe} is negligible. Under such conditions slag conductivity is more sensitive to slag structure than either b_l/A or $\sigma_W A$. However, it should be realized that conductivity measurements for higher contents of FeOx would begin to lose sensitivity to slag structure. This is because the σ_{Fe} term could no longer be considered negligible and would begin to dominate the overall conductivity.

5.3.2.7 Summary

The viscosity influence section demonstrated the ability of b_l/A and $\sigma_W A$ to distinguish between slags of different structures – an improvement over an OCV measurement which simply yields oxygen activity information. However, slag conductivity using HF impedance provided the greatest sensitivity to slag structure changes. This was attributed to the partial conductivity of iron cations as compared with calcia cations for low FeOx containing slags.

Table 5.4 Electrode surface area and OCV prior to applied DC potential step. L and H 2wt% FeOx containing slags (pap5 and pap10 respectively).

Applied Pot Step	pap5 - L OCV	pap10 - H OCV	pap5 - L Area	pap10 - H Area
-0.2	-0.0919	-0.0444	0.4812	0.55
-0.4	-0.1178	-0.0934	0.434	0.55
-0.6	-0.1613	-0.1894	0.379	0.55
-0.8	-0.21	-0.2963	0.325	0.55

Figure 3.17a Viscosity diagram for $CaO-Al_2O_3-SiO_2$ slag at 1500°C[82].

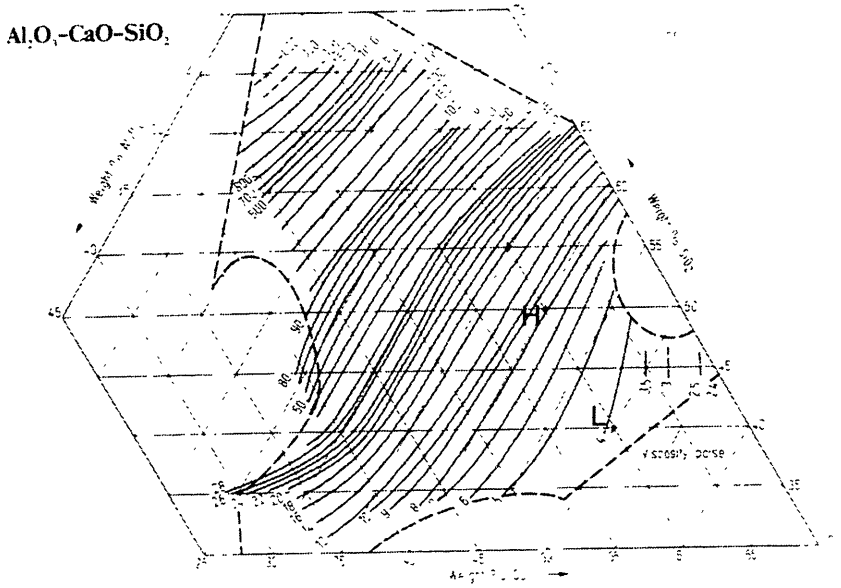

Figure 5.18 HF impedance as function of experiment time. HF impedance can detect slag level drop associated with ZrO_2 corrosion during L type slag measurements.

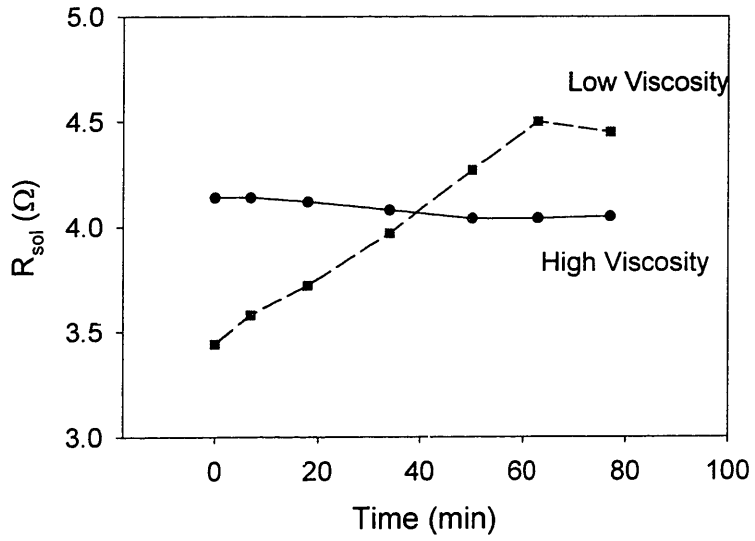

Figure 5.19 OCV vs slag structure and wt%FeOx. Neither H or L type slag demonstrates influence of wt%FeOx on OCV measurement.

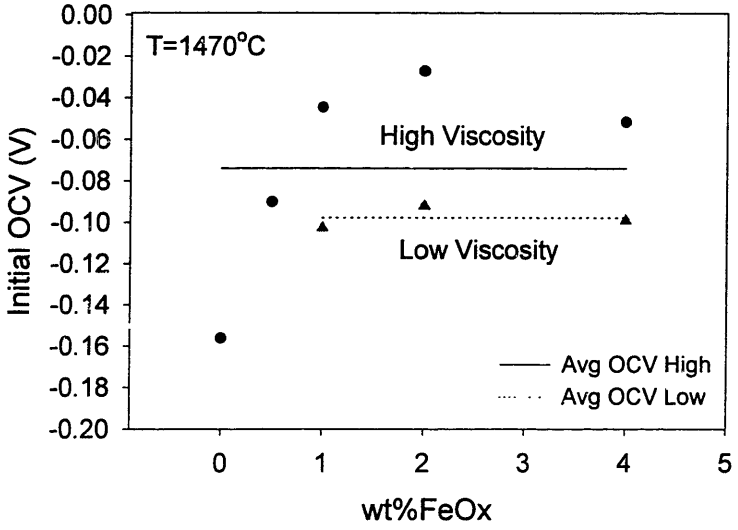

Figure 5.20 b_1/A for low and high viscosity slags (2wt%FeOx). Model generated from H type slag data assuming that L type slag behaves as would be predicted from viscosity differences (equation 5.78, figure 3.17a).

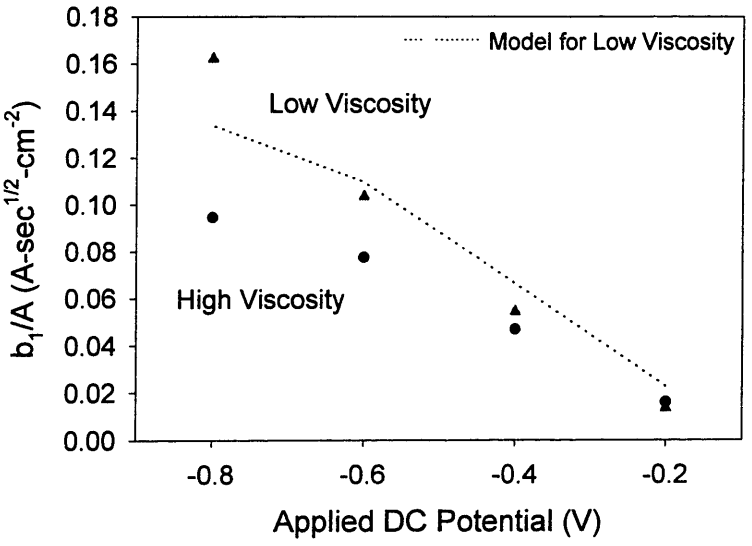

Figure 5.21 $\sigma_W A$ for low vs High viscosity slags (2wt%FeOx). Model generated from H type slag data assuming that L type slag behaves as would be predicted from viscosity differences (equation 5.78, figure 3.17a).

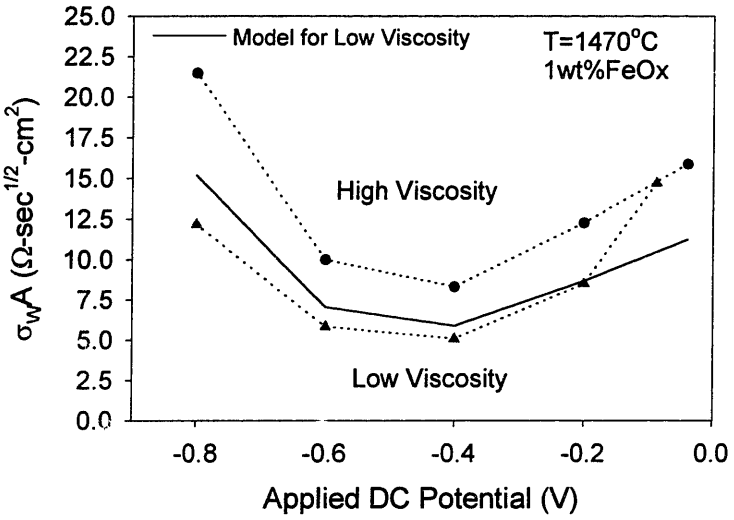

Figure 5.22 Low and high viscosity influence on conductivity. Slag conductivity is a very good measure for changes in slag structure. Measured values for conductivity agree well with data available in the literature[133,134].

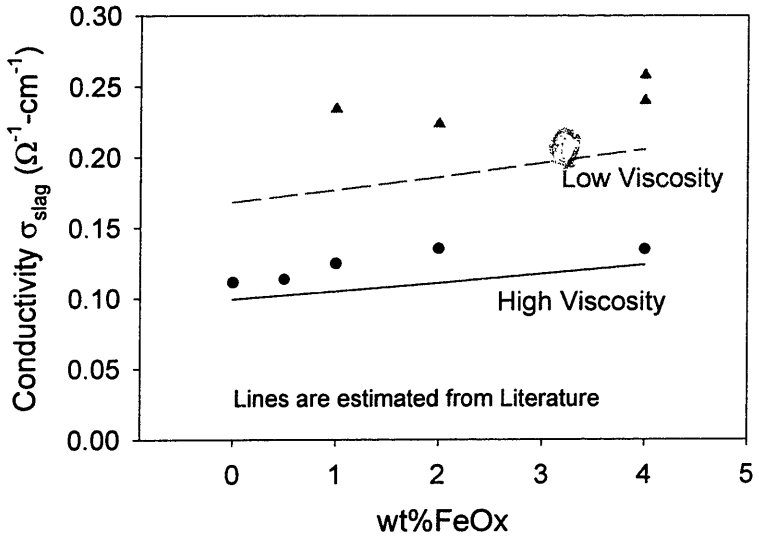

5.3.3 Solute Oxide Influence

5.3.3.1 Introduction

As well as yielding information on the concentration of dissociable oxides within a slag, amperometric techniques can also be used to indicate the type of oxide species present. This thesis is focused mainly on the properties of FeOx within the slag but one experiment utilized CuOx in place of FeOx in order to demonstrate the capability of amperometric measurements to resolve different dissociable oxide species in a high temperature $CaO\text{-}Al_2O_3\text{-}SiO_2\text{-}MOx$ system.

As described in the experimental theory section, the thermodynamics concerning the dissociable oxide species is important in determining the relative redox ratio and buffering capacity of the slag at a given oxygen activity (equation 5.87).

$$E_{OCV} = E^0_{air} + \frac{RT}{F}\ln(X_{rat}) + \frac{RT}{F}\ln(\gamma_{rat}) \tag{5.87}$$

Figure 5.23 demonstrates the difference in redox ratio for CuOx as compared with FeOx assuming that γ_{rat} is 1.2 for the low viscosity slag as described in the slag characterization section. Notice that the CuOx curve is displaced to the right of the FeOx curve – this is because CuO is less stable under reducing conditions than Fe_2O_3. The amperometric methods will utilize this displacement in order to act as an indicator for the type of oxide present within the slag.

5.3.3.2 OCV

The OCV value for the CuOx slag was –0.0277V as compared with –0.1025V for the FeOx slag. As described in the viscosity section, the OCV measurement only yields information on the oxygen activity and therefore any difference recorded between these two slags must be due to secondary effects. The CuOx containing slag demonstrated a slightly more oxidizing initial OCV, which might be attributed a number of different factors. The buffering capacity as measured by equation 5.88 would be larger for CuOx slags than FeOx slags at oxidizing potentials.

$$BC_{(E)} = nC_{M_{Tot}}\left(\frac{d\left(\frac{C_{M_O}}{C_{M_{Tot}}}\right)}{dE}\right) = \frac{nFC_{M_{Tot}}}{RT}\left[\frac{X_{rat}}{1+X_{rat}}\left(1-\frac{X_{rat}}{1+X_{rat}}\right)\right] \tag{5.88}$$

The buffering capacity measures the resistance of the slag to changes in oxidation state. A larger buffering capacity would indicate that more oxygen would have to be removed from the slag to the argon phase in order to achieve the same oxidation state. Another factor that may have influenced the OCV measurement may have been the ability of the FeOx containing slag to transport oxygen more rapidly than a CuOx containing slag.

5.3.3.3 DC Applied Potential Steps

Figure 5.24 demonstrates the difference between the b_1/A values for the CuOx and FeOx containing slags. Direct comparison between the two curves are difficult because the initial OCVs were not identical between the two measurements.

5.3.3.4 Impedance

Figure 5.25 demonstrates the difference between the CuOx and FeOx containing slags. Both CuOx and FeOx demonstrate U-shaped Warburg responses. The minima of the U-shaped curve should be located at $E_{1/2}$ as described by equation 5.89.

$$E_{1/2} = E_{air}^{o'} + \frac{RT}{F}\ln\left(\frac{1}{\sqrt{D_{rat}}}\right) \tag{5.89}$$

Assuming D_{rat}=1 and γ_{rat}=1.2 the $E_{1/2}$ for FeOx and CuOx should be located at -0.324V and 0.245V respectively. The minima for the FeOx data appears to be approximately –0.4V, which is relatively close to the predicted value of -0.324V. As would be expected, the CuOx curve in figure 5.25 is displaced to the right of the FeOx containing slag. However, the minima for CuOx in figure 5.25 appears to be closer to 0V than the 0.245V predicted from figure 5.23. In calculating figure 5.23 the γ_{rat} value for CuOx was estimated to be identical to the known value of 1.2 for FeOx because data concerning CuOx in similar slag structures was unavailable. Recalculation of γ_{rat} from the data obtained in figure 5.25 reveal that γ_{rat} for CuOx in the low viscosity slag used in this thesis is closer to a value of 0.3. This emphasizes the importance of determining γ_{rat} values independently for solute oxide species in a given slag. The value of 0.3 can be confirmed by measuring the equilibrium redox ratios for CuOx under atmospheres containing different oxygen activities. Such techniques are described in the future work section and are beyond the scope of this thesis.

5.3.3.5 Summary

The solute oxide influence section demonstrated the ability of impedance measurements to distinguish the type of solute oxide present in a high temperature slag solvent. Potential step measurements could not clearly distinguish the oxide type because of the sensitivity of the measurement to the initial OCV value which fluctuated during the experiment.

Figure 5.23 Redox ratio of CuOx as compared with FeOx. Note that the redox curve for CuOx is located far to the right of the FeOx redox curve. This is because CuO is less stable at reducing atmospheres than Fe_2O_3.

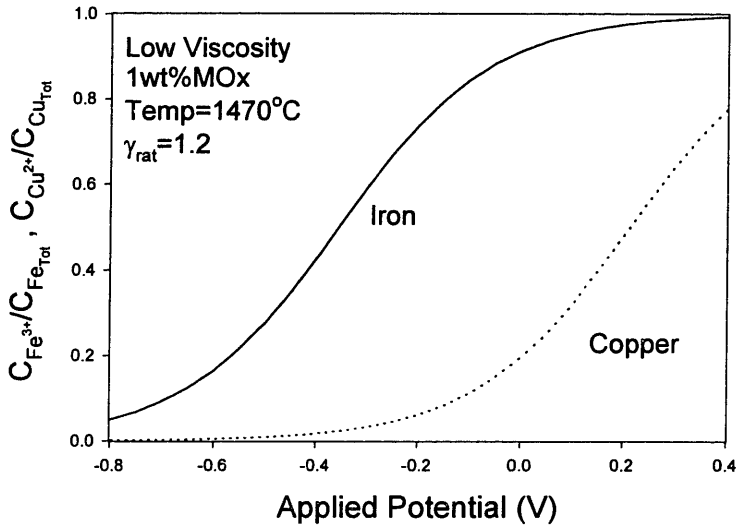

Figure 5.24 b_1/A for CuOx vs FeOx. 1wt% L type slags at 1470°C.

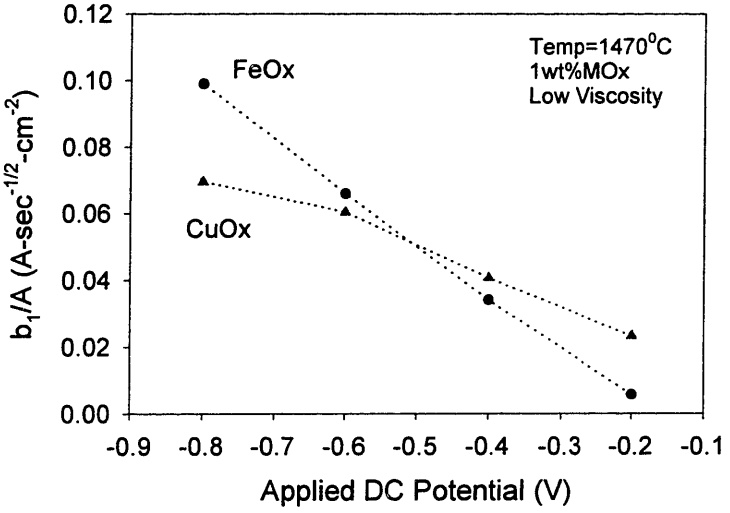

Figure 5.25 $\sigma_W A$ for CuOx vs FeOx. FeOx and CuOx can be differentiated by the location of the minima in the $\sigma_W A$ plot.

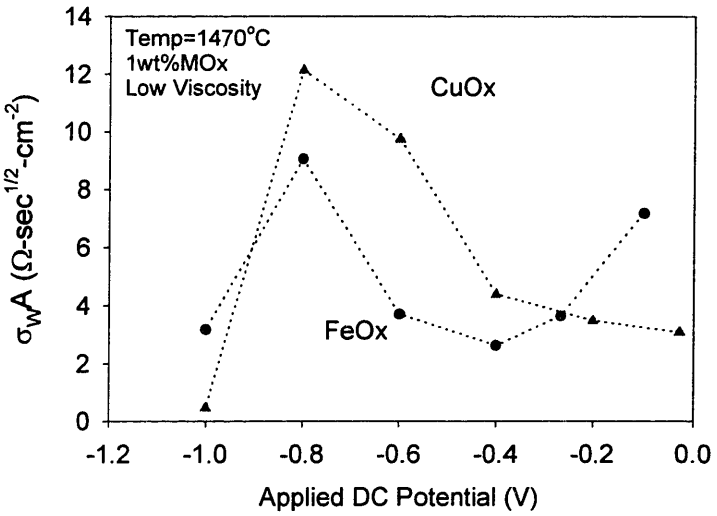

5.3.4 Estimation of Transport Properties

5.3.4.1 Introduction

The use of amperometric measurements allow for the estimation of cationic transport properties concerning the species reacting at the WE/slag interface. In order to estimate the proper diffusion coefficients accurate knowledge of the concentration, slag structure, and WE reaction must be known. Estimates for D_{Fe2+} and D_{Fe3+} were made for the high viscosity slags using both AC and DC methods as will be described in the following subsections.

The relative concentration of Fe^{3+}/Fe^{2+} at a given potential was calculated using a γ_{rat} of 1.8 obtained from literature data[135] concerning similar slag structures as was described in the slag characterization section. Changes in the total FeOx concentration were assumed to negligibly influence the slag structure; measurements in the literature[136] confirm this assumption for the Henrian range for slags containing FeOx. Therefore D_{Fe3+} and D_{Fe2+} are not expected to differ significantly with FeOx concentration over the range 0.5-4 wt%FeOx. In order to ensure that the reaction at the WE/slag interface was predominantly due to the FeOx redox reaction only potentials with magnitudes less than or equal to -0.6V were examined in the calculations below. This was because magnitudes greater than -0.6V may have contained additional reactions involving the reduction of either Fe^{2+} or Si^{4+} species at the WE which would have led to improper transport calculations as shown in Solvent section.

5.3.4.2 DC Method

Equation 5.90 was used previously to demonstrate the relationship between the measured current and the concentration for an applied DC potential step.

$$i(t) = \frac{b_1}{\sqrt{t}} = \frac{FA(\theta_{ocv} - \theta_{app})C_{Fe_{tot}}}{(1+\xi\theta_{app})(1+\theta_{ocv})}\sqrt{\frac{D_{Fe^{3+}}}{t\pi}} \tag{5.90}$$

Using a best-fit least squared error analysis of the DC potential step data for 0.5-4 wt%FeOx over the potential range of –0.2V to –0.6V, values of D_{Fe3+} and D_{rat} were found to be 2.85×10^{-5} cm²/sec and 9.52 respectively for γ_{rat} of 1.8. Figure 5.26 demonstrates the results of the model compared with the experimental data.

5.3.4.3 AC Method

Equation 5.91 has been used previously to demonstrate the relationship between total FeOx concentration and σ_W.

$$\sigma_W = \frac{RT}{n^2F^2A\sqrt{2D_{Fe^{3+}}}C_{FeO_X}}\left(2 + \frac{1}{\xi\theta} + \xi\theta\right) \tag{5.91}$$

Using a best-fit least squared error analysis of the $\sigma_W A$ impedance data for 0.5-4 wt%FeOx over the DC applied potential range of OCV to –0.8V, values of D_{Fe3+} and D_{rat} were found to be 1.72×10^{-5} cm²/sec and 6.01 respectively for γ_{rat} of 1.8. Figure 5.27 demonstrates the results of the model compared with the experimental data.

5.3.4.4 AC and DC Comparison

The models for both the DC potential step and impedance methods demonstrate excellent correlation between each of the FeOx concentrations examined in the low applied potential region. Deviation begins to occur at -0.8V because of additional WE/slag reactions involving Fe^{2+} and Si^{4+}. This results in lower $\sigma_W A$ and higher b_1/A values than would be predicted in this region as demonstrated in figures 5.26 and 5.27.

Values for D_{Fe3+} and D_{rat} for the DC method were found to be slightly higher than those found for the AC method. The DC method relied upon the knowledge and stability of the OCV which may have not been fully at equilibrium thereby resulting in slightly higher b_1/A values than predicted. Another possibility for this difference is that the γ_{rat} of 1.8 is not a good description of the oxobasicity of the slag structure. As described in the slag characterization section γ_{rat} was estimated from reliable sources for similar slag structures to be approximately 1.8. However, data concerning γ_{rat} tend to vary by large amounts in the literature because of measurement difficulties related to changing oxidation states during quenching, inappropriate equilibration, slag structure differences, and required accuracy in measurement techniques. Comparing the DC and AC methods a best fit can be obtained for both techniques when γ_{rat} is 0.9. When γ_{rat} is 0.9 the modeled value for D_{rat} becomes 1.76 and 1.5 for the DC and AC methods respectively and the modeled value for D_{Fe3+} becomes 1.72×10^{-5} cm^2/sec for both cases.

As was discussed in the slag characterization section, diffusion coefficients on the order of 1×10^{-5} cm^2/sec are in excellent agreement with values commonly found in the literature for Fe^{X+} cations in acidic slags[137,138,139,140]. Unfortunately very little information exists on the relative diffusion coefficients of Fe^{3+} and Fe^{2+} species in slags

(D_{rat}). However, Yokokawa[141] also found D_{rat} values which ranged from 1-2 for FeOx in Na_2O glass compositions.

5.3.4.5 Summary

The transport properties section demonstrated that the diffusion coefficients for the cationic species reacting at the WE/slag interface can be estimated by using amperometric measurements on a known slag structure and composition. However, knowledge of the slag structure must be known very accurately because diffusion data is very sensitive to the γ_{rat} value. Values were determined for the high viscosity slags and demonstrated diffusion properties on the same order as those reported in the literature. This is beyond the capabilities of a conventional oxygen sensor.

Figure 5.26 Model of transport properties using b_1/A.

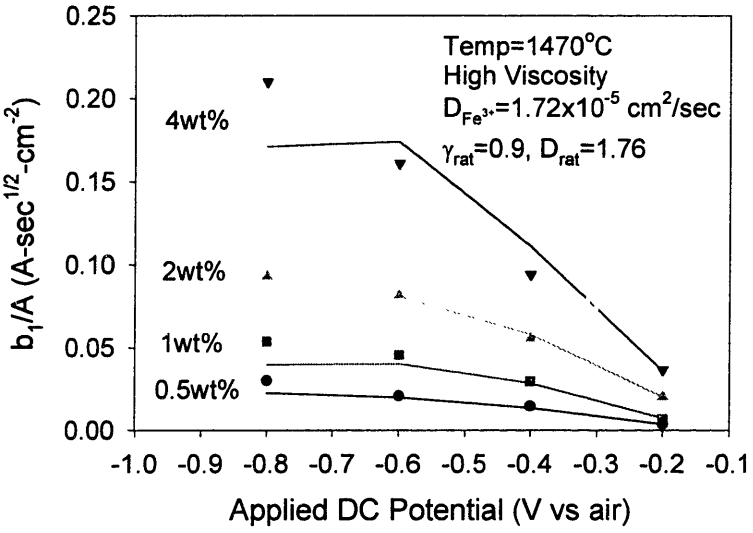

Figure 5.27 Model of transport properties using $\sigma_W A$.

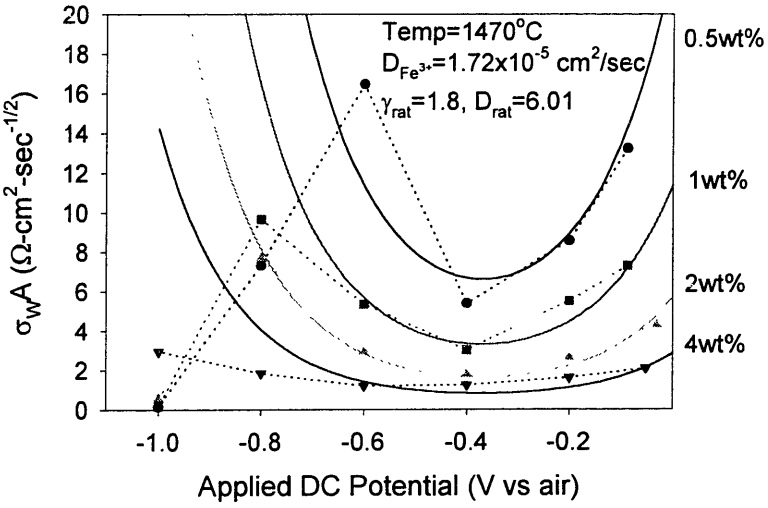

5.3.5 Solvent Influence

5.3.5.1 Introduction

Previous sections have demonstrated the influence of parameters such as solute concentration and solute type on the response of different amperometric techniques. The influence of the solvent slag on the thermodynamic and transport properties was considered during the analysis. However, the solvent was been assumed to be an inert phase during application of applied potentials. This section will examine this assumption and determine the extent of influence of the solvent at different applied potentials.

5.3.5.2 Low Applied Potentials

CNLS fitting of the 0 wt%FeOx solvent slag demonstrated that impedance frequency sweep methods at low applied potentials were primarily dominated by Warburg diffusion control as shown in table 5.3. Charge transfer resistance within the cell was found to be minimal. The main reaction occurring in the solvent slag is most likely the reduction of oxygen species which leads to an increase in the basicity of the surrounding melt as described by Emi et al.[142] and given by equations 5.92 and 5.93.

$$O_2 + e^- = O_2^- \tag{5.92}$$

$$O_2^{2-} + 2e^- = 2O^{2-} \tag{5.93}$$

Sasabe[143] demonstrated that the permeability of oxygen in slags is quite low without the presence of FeOx and therefore the impedance associated with these reactions is also

likely to be quite large. Another possible reaction would be the reduction of oxygen gas at the slag/metal/gas three-phase interface as described by equation 5.94.

$$\tfrac{1}{2}O_2 + 2e^- = O^{2-} \tag{5.94}$$

Miyaki[144] theorized that the above reaction may be important for Na_2O based melts under an air atmosphere but was unable to detect its influence. In the current investigation the impedance associated with equation 5.94 should also be quite large because the three-phase surface area for reaction is relatively small and Argon was used as a protective gas. Another source of faradaic current would be the reduction of any easily dissociable impurity ions located in the solvent by the redox reaction in equation 5.95.

$$M^{(m+n)+} + ne^- = M^{m+} \tag{5.95}$$

Impurity ions would consist of Fe, Mn, Cu, Mo, or others, which may have been present in the initial slag-making components or introduced inadvertently during slag processing. The main impurity present in the initial slag components would be iron. The total iron present in the solvent slag was estimated to be approximately 0.077wt%.

Figure 5.28a demonstrates an equivalent circuit describing the three possible reaction paths for the solvent slag. For simplicity the three reactions can be combined into a single "$Z_{solvent}$" impedance term as shown in figure 5.28b. Addition of an easily dissociable solute oxide such as FeOx would add another competing parallel reaction path, Z_{solute}, associated with the reduction of the solute oxide as shown in figure 5.28c. At low applied potentials, $Z_{solvent}$ was found to be significantly larger than the impedance measured for the FeOx containing slags examined in this thesis. Therefore, the $Z_{solvent}$ term can be ignored in the previous sections at low applied potentials without distortion

of the results. However, it should be noted that $Z_{solvent}$ does place a limit on the measurable concentration of easily dissociable oxide within the slag. Extrapolations of Z_{solute} from FeOx slags in this thesis indicate that Z_{solute} for 0.1wt% FeOx containing slags will approximately equal $Z_{solvent}$. Concentrations lower than 0.1% would be therefore be difficult to resolve from the background.

5.3.5.3 Large Applied Potentials

Figure 5.29 demonstrates the magnitude of the current response to an applied DC potential step for a 2 wt%FeOx containing slag. At low applied potentials the steady state current was relatively small, however at potentials larger than –1V significantly large currents were measured. These large currents are attributed to both the reduction of SiO_2 and FeO via equations 5.96-5.99. Sotnikov et al.[145] proposed that the reduction of SiO_2 on an iron electrode is a two-step process limited by diffusion as given by equations 5.96 and 5.97. Similar reactions are expected to hold for a platinum electrode.

$$Si^{4+} + 2e^- = Si^{2+} \tag{5.96}$$

$$Si^{2+} + 2e^- = Si^0 \tag{5.97}$$

Slags containing FeOx would be expected to undergo the following reductions at the platinum electrode.

$$Fe^{3+} + e^- = Fe^{2+} \tag{5.98}$$

$$Fe^{2+} + 2e^- = Fe^0 \tag{5.99}$$

Application of large DC potentials for extended periods of time led to the destruction of the WE. WE destruction occurred because Si and Pt are capable of forming a stable liquid phase over a wide range of compositions and temperatures as shown in the binary

phase diagram (figure 5.30)[146]. A Pt-Si molten WE was found to climb out of the slag in order to minimize the surface energy associated with the WE/slag interface. Figure 5.31 is a cross-section of a solidified WE which had been destroyed in this manner. The original electrode wires are marked in the diagram and are surrounded by the solidified molten electrode material described above. The molten material formed a granular structure during cooling which contained a significant amount of dissolved Si especially in the low melting point intergranular phase. Table 5.5 explains the composition of various phases in the diagram. Serata et al.[147] reported similar Pt/Si interactions while investigating a $63SiO_2$-26CaO-$11Al_2O_3$ mol% slag at 1460°C under both Argon and air atmospheres.

Impedance measurements of the solvent slag demonstrated similar behavior in figure 5.32. For applied DC potentials larger than -0.8V the cell impedance was found to drop dramatically, apparently due to the reduction of SiO_2 as described in equations 5.96 and 5.97.

Under conditions where the bulk solvent phase is undergoing reduction, determination of the FeOx concentration would be nearly impossible. This is because the current associated with the large concentration of solvent phase is substantially larger than that associated with the solute oxide. In addition, solvent breakdown is likely to drastically alter the slag structure near the WE surface. This would alter the viscosity, basicity, conductivity, and thermodynamic properties of the slag which would cause difficulty in interpreting the results associated with the solute species.

While useful measurements of the dissociable oxide concentration cannot be obtained at large applied potentials, valuable information concerning the buffering

capacity of the slag phase to a given oxidation state can still be determined. For example, figure 5.29 demonstrates that the oxidation state of the slag can be easily manipulated at low applied potentials but is very resistant to change at potentials greater than –1V. Therefore if a steelmaker wanted to achieve an oxidation state equivalent to approximately –1.2V a significant quantity of deoxidizer would have to be added to the system. This emphasizes the added information which can be obtained by using amperometric techniques. With a conventional oxygen sensor, the steelmaker would know only the oxidation state of the system. An amperometric device helps determine the buffering capacity which would be required to alter the state of the system. For the above example, it would be very difficult to obtain –1.2V without reducing significant quantities of SiO_2 from the slag – perhaps the steelmaker would be better advised to use a more basic slag containing smaller quantities of SiO_2 in order to achieve the desired oxidation state.

5.3.5.4 Summary

Chemical reactions with the solvent do not significantly effect measurements of solute oxides within the slag phase at low applied potentials. However, reactions with the solvent will establish a lower limit on the measurable concentration of easily dissociable oxides that can be resolved within the slag. Application of large potentials can result in solvent breakdown as SiO_2 is reduced to Si^{2+} and Si. Dissolution of silicon into the platinum electrode leads to WE destruction which prevents accurate amperometric measurements. Therefore useful measurements of dissociable oxide concentration should be limited to potential regions where the solvent is stable. Using a platinum electrode in

highly acidic slags, this region appears to be less than –0.8V vs air. While useful measurements of the dissociable oxide concentration cannot be obtained at large applied potentials, valuable information concerning the buffering capacity of the slag phase to a given oxidation state can still be determined.

Table 5.5 Composition of damaged WE

	Si (wt%)	Pt (wt%)	Rh (wt%)	Fe (wt%)
Phase I	1	86	7	7
Phase II	3	91	5	1
Phase III	5	77	18	0

Phase I: Intermediate color associated with the grain structure of molten liquid region.
Phase II: Bright color near the grain boundaries.
Phase III: Dark color at the grain boundaries.

Figure 5.28a Equivalent circuit of the solvent near the WE/slag interface.

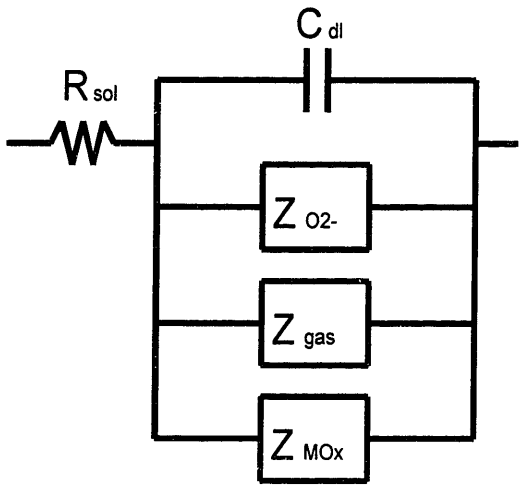

Figure 5.28b Equivalent circuit of the solvent near the WE/slag interface – simplified.

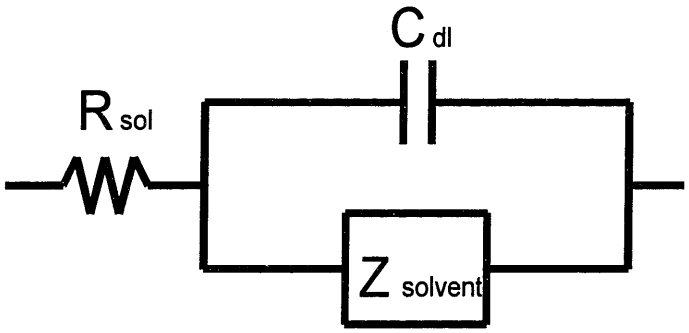

Figure 5.28c Equivalent circuit of the solute near the WE/slag interface. Note that the solvent provides a parallel reaction path in theory.

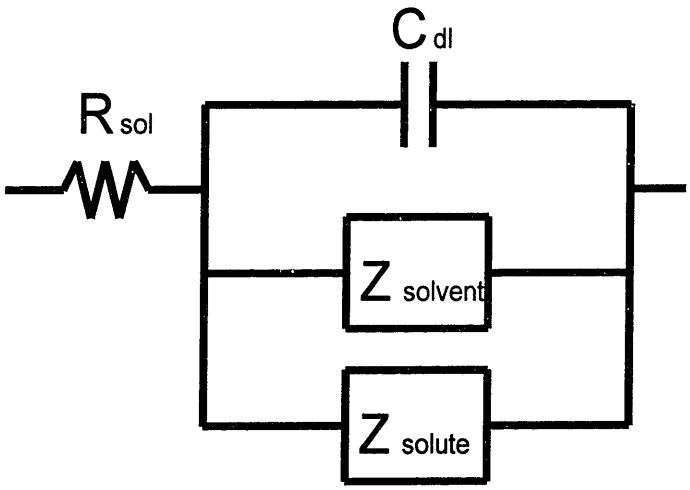

Figure 5.29 Steady state current with applied DC potential for the 2 wt%FeOx H type slag at 1470°C. At low applied potentials the predominant reaction in the redox reaction. At large applied potentials reduction of SiO_2 in the solvent can occur leading to large measured currents and electrode destruction.

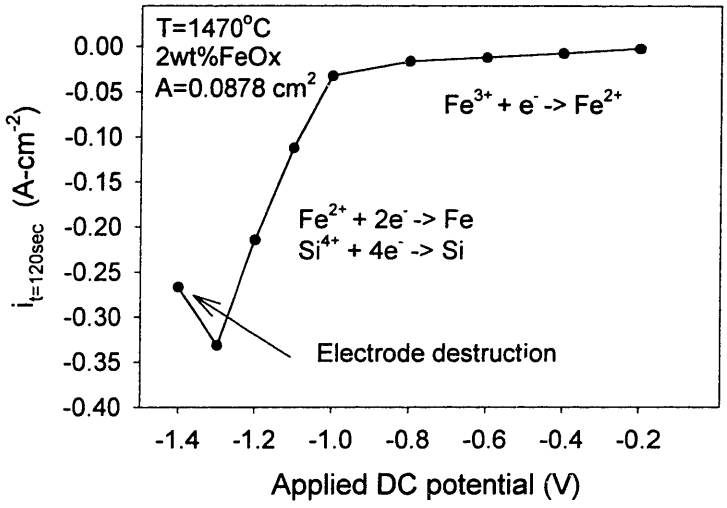

Figure 5.30 Si-Pt Phase diagram. Pt and Si form a liquid alloy over a wide temperature range[146].

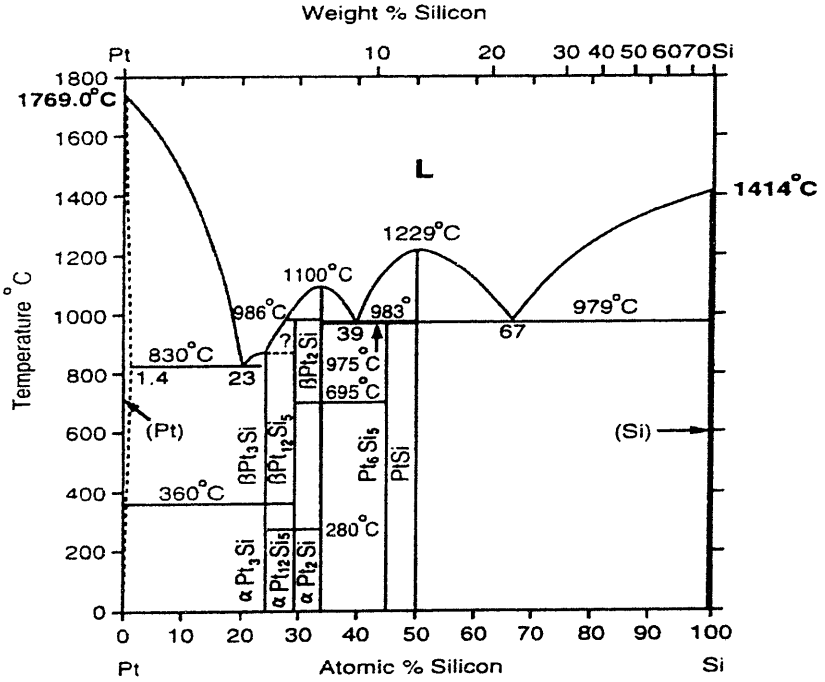

Figure 5.31 Photograph of damaged WE. The two original electrodes are still present and surrounded by a once liquid Pt-Si-Fe alloy. The intergranular phase is an Si rich lower melting point alloy.

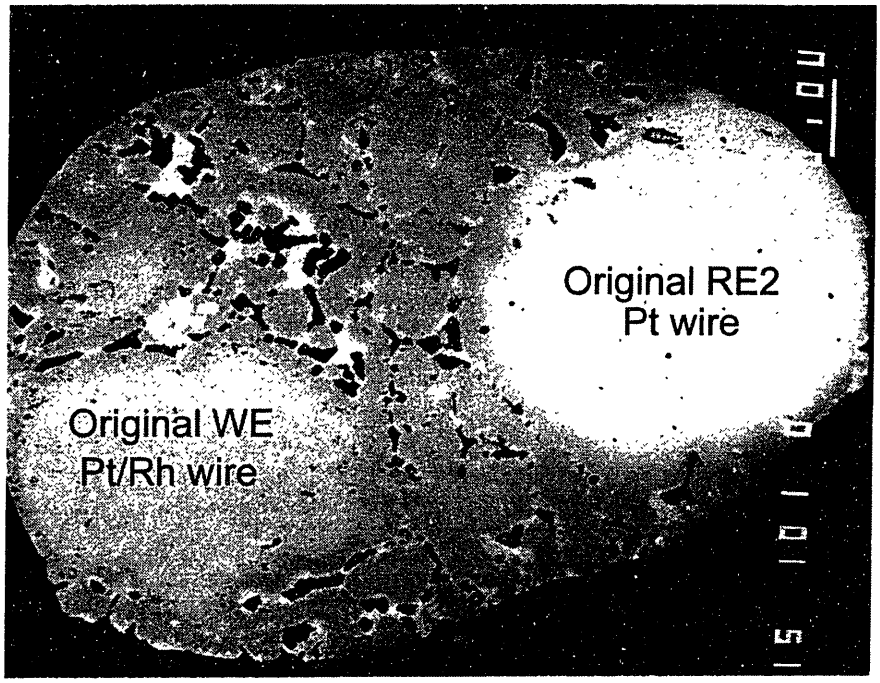

Figure 5.32 Impedance measurement of solvent slag.

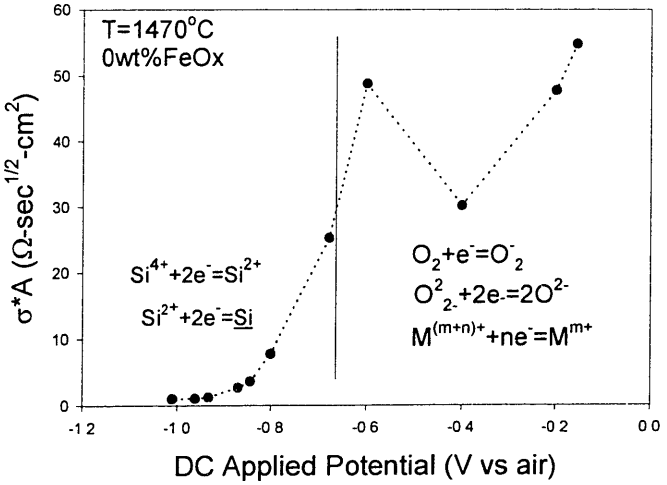

6 Experimental – High FeOx

This chapter will describe the amperometric measurements applied to slags containing high quantities of FeOx (>10wt%). The amperometric technique utilized was coulometric titration. The chapter consists of the following sections: First the experimental setup will be described. Then the appropriate theory will be introduced for the coulometric measurement technique. Finally, the results will be reported and analyzed.

6.1 Experimental Setup

6.1.1 Experimental Cell

Figure 6.1 demonstrates the setup used during the coulometric titration of high FeOx containing slags. The zirconia solid electrolyte separates the reference gas phase consisting of air from the slag phase to be measured. An inert Argon gas (BOC gasses – Grade V) is flowed through the system in order to prevent any slag/gas reactions from occurring during experimentation. The zirconia tube consisted of ZDY-4 and was characterized in the zirconia characterization section. The counter electrode (CE) consisted of a platinum gauze (mesh size, 0.2"ht x ZrO_2 OD) sintered to the zirconia tube outer diameter (OD) using platinum ink (Engelhard #6926). Two lead wires were connected to the CE in order to provide an S-type T/C for temperature measurement. An additional electrode was utilized in the gas phase consisting of another T/C where the Pt

electrode was used as the primary reference electrode. RE1 consisted of a 0.02 inch diameter wire sintered to the zirconia with Engelhard Pt ink. The working electrode (WE) consisted of eight 0.02" diameter x 1" long platinum wires welded to the end of a Pt/Pt-10%Rh T/C. The 10%Rh lead was utilized as the secondary reference (RE2) and the Pt lead as the WE. At operating temperature, the wires were immersed into the slag until they touched the bottom of the zirconia tube.

Three slag compositions were investigated ranging from 20-40wt% in CaO-SiO_2-FeOx containing slags as described in equation 6.1.

$$\left(0.37CaO - 0.63SiO_2\right)_{100-z}\left(Fe_2O_3\right)_z \qquad z = \{20,30,40\} \qquad (6.1)$$

The preparation techniques and theoretical properties for each of the compositions was previously described in the slag characterization section. Approximately 1.5g of slag sinter was charged into the sensor at room temperature for each investigation.

6.1.2 Equipment

The experimental setup used for the high FeOx containing slags was identical to the setup described in section 5.1.2 of the low FeOx containing slag experimental setup section with a few minor exceptions. No impedance analyzer or gas sensor were utilized during the measurements and all experiments were conducted at temperatures near 1570°C.

6.1.3 Measurement Procedure

The following steps describe the procedure followed for a typical coulometric titration measurement on a given high FeOx containing slag.

1. At room temperature the cell is fabricated as shown in figure 6.1 and the slag sinter is charged into the sensor. The WE tip is positioned well above the slag surface and argon is flowed through the system at 15 ml/min. The furnace is then programmed to heat to 1570°C at a rate of 4°/min. The hydra data acquisition system is turned on and begins recording data.
2. When the furnace reaches a temperature of 1570°C the system is allowed to equilibrate for at least 15 minutes. The WE is lowered slowly until contact of the WE with the bottom of the zirconia tube is established. An OCV measurement is taken for 10 minutes.
3. After the OCV measurement, the potential between the RE1 and RE2 electrodes is ramped from OCV to –0.2V at 3mV/sec and the current is measured with respect to time.
4. At –0.2V the potential is held until the measured current drops to a small fraction of the initial current.
5. Steps 3 and 4 are repeated at -0.2V increments until the potential is held at –1V.
6. The furnace is turned off and the cell is quenched to room temperature.
7. The quenched cell is sectioned and examined using visual inspection, SEM, and/or chemical techniques.

Figure 6.1 Experimental setup for the coulometric titration of high FeOx containing slags.

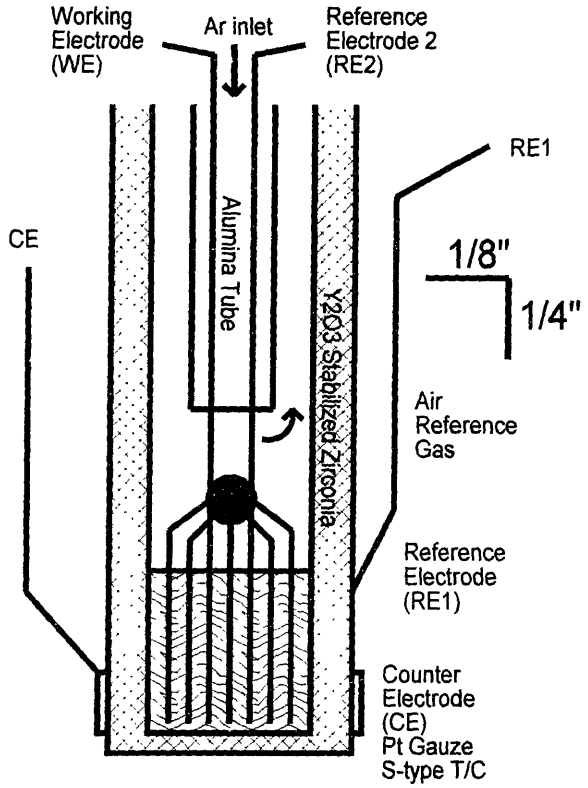

6.2 Experimental Theory

Impedance and potential step measurements used for investigating the low FeOx slags examined the reactions occurring at the WE/slag interface in order to determine information concerning the slag phase. These methods become more difficult to implement with increasing FeOx concentration because of the large currents which are generated. The large currents result in large iR_{sol} potential drops which require strict electrode positioning in order to ensure that no inhomogeneities occur along the WE/slag interface and that identical cell operation is established under all conditions. Coulometric titration techniques examine the bulk changes of an isolated slag volume as opposed to the surface changes at a WE/slag interface. Many wires are immersed into a known volume of slag and the oxygen associated with easily dissociable species is pumped out of the slag until the entire slag volume reaches another desired thermodynamic equilibrium state. By measuring the charge removed during this process the buffering capacity and concentration of dissociable oxide species can be estimated.

The following sections will describe the reversible cell potential as it relates to the thermodynamic equilibrium state of the slag and derive a model for the system response to a coulometric titration.

6.2.1 Reversible Cell Potential

The reversible cell potential was fully explained in the low FeOx experimental theory section. Equations 6.2 and 6.3 were previously derived in order to describe the equilibrium between Fe^{3+}, Fe^{2+}, and Fe at a given potential.

$$E_{OCV} = E^{0'}_{air} + \frac{RT}{F}\ln\left(\frac{X^{WE}_{FeO_{1.5}}}{X^{WE}_{FeO}}\right) = E^{0'}_{air} + \frac{RT}{F}\ln\left(X_{rat}\right) \tag{6.2}$$

$$E_{OCV} = E^{0'}_{air} + \frac{RT}{F}\ln\left(X^{WE}_{FeO}\right) \tag{6.3}$$

Therefore, under coulometric titration conditions when the cell current approaches zero, equations 6.2 and 6.3 approximate the equilibrium state of the entire slag with respect to the measured potential.

6.2.2 Coulometric Titration

The quantity of charge required to assume a new equilibrium state during coulometric titration of FeOx-CaO-SiO_2 slag can be described by equation 6.4.

$$\Delta Q = Q^{ocv} - Q^{app} = F\left[3\left(n^{ocv}_{Fe^{3+}} - n^{app}_{Fe^{3+}}\right) + 2\left(n^{ocv}_{Fe^{2+}} - n^{app}_{Fe^{2+}}\right)\right] \tag{6.4}$$

The relative concentrations of Fe^{3+}/Fe^{2+} in the slag can be determined from the measured potential with respect to the reference as described by equation 6.2. At large applied potentials, iron will be in equilibrium with the slag and an additional constraint will be applied to the system as described by equation 6.3. The terms in equation 6.4 can therefore be calculated using equations 6.5-6.9 as described below.

$$n^{ocv}_{Fe^{2+}} = \frac{n^{ocv}_{tot}}{1 + X^{ocv}_{rat}} \tag{6.5a}$$

$$n^{app}_{Fe^{2+}} = \frac{n^{app}_{tot}}{1 + X^{app}_{rat}} \tag{6.5b}$$

$$n^{ocv}_{Fe^{3+}} = n^{ocv}_{tot}\left(\frac{X^{ocv}_{rat}}{1 + X^{ocv}_{rat}}\right) \tag{6.6a}$$

$$n^{app}_{Fe^{3+}} = n^{app}_{tot}\left(\frac{X^{app}_{rat}}{1 + X^{app}_{rat}}\right) \tag{6.6b}$$

$$X^{ocv}_{rat} = \exp\left(\frac{\left(E^{ocv} - E^{0'}_{rat}\right)F}{RT}\right) \tag{6.7a}$$

$$X^{app}_{rat} = \exp\left(\frac{\left(E^{app} - E^{0'}_{rat}\right)F}{RT}\right) \tag{6.7b}$$

where n is the number of moles of Fe^{3+} or Fe^{2+} in the confined slag, X_{rat} is the ratio of Fe^{3+}/Fe^{2+} species in the confined slag, ocv is the initial equilibration state of the system, app is the final equilibration state of the system, and n_{tot} is the number of iron units present in the slag phase. If no metallic iron exists at the given slag equilibration state than n_{tot} will be given by equation 6.8.

$$n_{tot}^{ocv} = \frac{(wt\%FeO_{1.5})g_{tot}}{MW_{FeO_{1.5}}} \qquad (6.8a) \qquad n_{tot}^{app} = \frac{(wt\%FeO_{1.5})g_{tot}}{MW_{FeO_{1.5}}} \qquad (6.8b)$$

If metallic iron exists at the given slag equilibration state than n_{tot} is given by equation 6.9.

$$n_{tot}^{ocv} = \frac{X_{FeO}^{ocv}\left(n_{SiO_2} + n_{CaO}\right)}{\left(1 - X_{FeO}^{ocv}\right)} \qquad (6.9a) \qquad n_{tot}^{app} = \frac{X_{FeO}^{app}\left(n_{SiO_2} + n_{CaO}\right)}{\left(1 - X_{FeO}^{app}\right)} \qquad (6.9b)$$

$$X_{FeO}^{ocv} = \exp\left(\frac{\left(E^{ocv} - E_{rat}^{0'}\right)F}{RT}\right) \qquad (6.10a) \qquad X_{FeO}^{app} = \exp\left(\frac{\left(E^{app} - E_{rat}^{0'}\right)F}{RT}\right) \qquad (6.10b)$$

where X_{FeO} is the mole fraction of FeO in the confined slag, n_{SiO2} and n_{CaO} are the number of moles of SiO_2 and CaO in the confined slag respectively.

Equations 6.4-6.10 above will be used to model the results obtained in the high FeOx coulometric titration experiments in the results and discussion section. Note however, that equations 6.4-6.10 could also be utilized to estimate the FeOx concentration in an unknown or partially known slag system. Further discussion and approaches concerning the use of coulometric techniques to determine more information on an unknown slag can be found in the future work and applications section.

6.3 Results and Discussion

Figure 6.2a demonstrates the typical i-V response to the 3mV/sec potential sweep from the initial cell conditions (-0.05V) to the applied cell conditions (-0.2V). Figure 6.2b demonstrates the typical i-t response to the applied potential step (-0.2V). After approximately 10 minutes the system was judged to be at equilibrium and the charge removed was calculated by integration of both the potential sweep and potential step responses.

$$\Delta Q = \int_0^t i(t)_{step}\,dt + \int_0^t i(t)_{sweep}\,dt \qquad (6.11)$$

The charge obtained by integration of each potential sweep and step can be found in table 6.1 for each of the three slags investigated. Figure 6.3 demonstrates the total coulombs removed from the slag in order to change the equilibration state of the slag from OCV (-0.05V) to the given applied potential. The solid lines in figure 6.3 are the coulombs predicted using the model developed in the theory section. The values utilized in the model were as follows: γ_{rat}=1, γ_{FeO}=2.5, γ_{tot}=1.5g. There is good agreement between the model and the measured data. The total charge removed at any given potential is sensitive to the total FeOx concentration in the slag. Slag compositions with larger FeOx concentrations have a larger buffering capacity to a given oxidation state and therefore require the removal of more charge in order to achieve a new equilibrium state. The data demonstrated two regions of reduction. At low potentials the predominant reaction was the reduction of Fe^{3+} to Fe^{2+} whereas at large potentials the predominant reaction was the reduction of Fe^{2+} to Fe. The data near the intermediate region (-0.6 to -0.8V) do not show the same sharp transition as the model would predict. This was likely caused by the

presence of platinum wires in the system. Platinum and iron form a solid solution at these temperatures and therefore some of the reduced iron may have formed with an activity less than one. This would have lowered the potential required for the reduction of Fe^{2+} species as demonstrated in equation 6.12.

$$E_{app} = E_{air}^{0'} + \frac{RT}{F}\ln\left(X_{FeO}^{WE}\right) - \frac{RT}{F}\ln\left(a_{Fe}^{WE}\right) \tag{6.12}$$

Figure 6.4 shows a typical cross-section of the cell after a coulometric titration experiment. Molten droplets of Fe can be found throughout the slag phase. The FeOx concentration in the bulk slag has dropped considerably from the initial 20-40wt% to values near 2-4wt%. The change in bulk slag FeOx concentration is consistent with the measured coulombs removed during the coulometric titration as calculated in table 6.2 indicating that the cell efficiency is nearly 100%.

The fact that the cell efficiency operates at nearly 100% allows the coulometric titration technique to be utilized accurately for determining the concentration of species in an unknown slag system. Current efficiencies of 100% are not commonly found in the literature concerning the electrolysis of oxide or salt melts containing iron oxide[148,149,150] using two electrodes immersed within the slag. Typical problems associated with electrolysis of FeOx containing slags without a zirconia membrane include the following:

1. Formation of an iron dendrite from the cathode which connects to the anode resulting in a short circuit.
2. Oxidation of the anode during electrolysis.
3. Reoxidation of iron units at the anode instead of the formation of oxygen gas resulting in no net electrolysis in the system.

4. Electronic short circuit due to hole conduction mechanism associated with large FeOx concentrations[151,152].

The use of a zirconia membrane in this investigation prevented the typical problems mentioned above. This was possible because the zirconia is primarily an oxygen anion conductor and therefore ensures that charge transfer reactions will occur and oxygen will be generated at the anode. However, at very reducing or oxidizing potentials the zirconia may become electronic, as described in the zirconia characterization section, at which point the cell may become less efficient. The potential at which the electronic and ionic transport numbers are equal was calculated to be near –1.35V at 1570°C for the ZDY-4 zirconia material.

6.4 Summary

This chapter demonstrated that coulometric titration techniques can be used to determine the concentration of easily dissociable oxide species in molten slags. The technique clearly differentiated between 20, 30, and 40 wt%FeOx and demonstrated close agreement with the predicted model. The cell efficiencies, which approached 100%, were obtained because of the membrane properties of the zirconia.

Table 6.1 Coulometric titration data for 20-40wt%FeOx.

	Potential (V vs air)	Sweep (Coulombs)	Step (Coulombs)	Qocv-Qapp (Coulombs)
20wt%FeOx				
	-0.05	0.000	0.000	0.000
	-0.2	-22.256	-73.725	-95.981
	-0.4	-27.817	-83.152	-206.951
	-0.6	-29.444	-93.497	-329.892
	-0.8	-76.282	-275.631	-681.805
	-1	-38.132	-152.739	-872.676
30wt%FeOx				
	-0.05	0.000	0.000	0.000
	-0.2	-51.438	-92.899	-144.337
	-0.4	-85.108	-77.059	-306.505
	-0.6	-56.139	-102.399	-465.042
	-0.8	-85.108	-338.585	-888.735
	-1	-97.502	-417.086	-1403.322
40wt%FeOx				
	-0.05	0.000	0.000	0.000
	-0.2	-101.306	-54.437	-155.743
	-0.4	-197.841	-2.384	-355.968
	-0.6	-130.253	-65.453	-551.674
	-0.8	-186.094	-589.952	-1327.721
	-1	-131.434	-406.753	-1865.908

Table 6.2 Cell Efficiency.

Initial wt%FeOx	Measured Charge Removed (Coulombs)	Final Measured wt%FeOx	Charge Required Initial to Final wt% (Coulombs)	Efficiency(%)
20	-872.676	4	-867	99.35
30	-1403.322	3	-1416	100.90
40	-1865.908	1.5	-1967	105.42

Figure 6.2a Typical i-V response to potential sweep during coulometric titration.

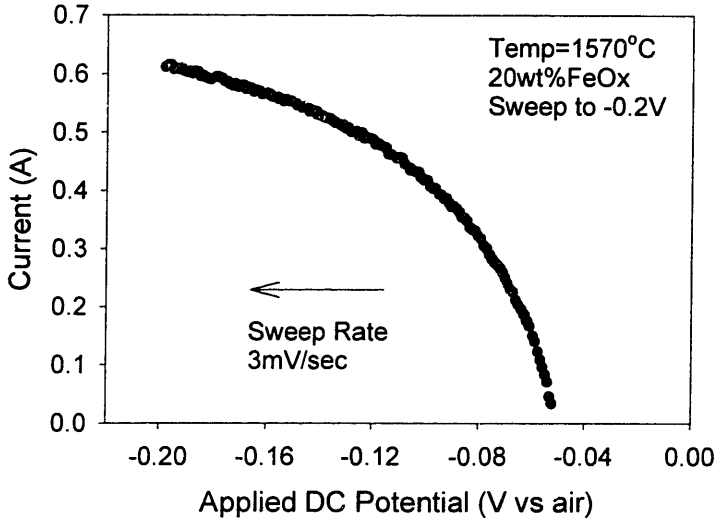

Figure 6.2b i-t response to an applied potential step during coulometric titration.

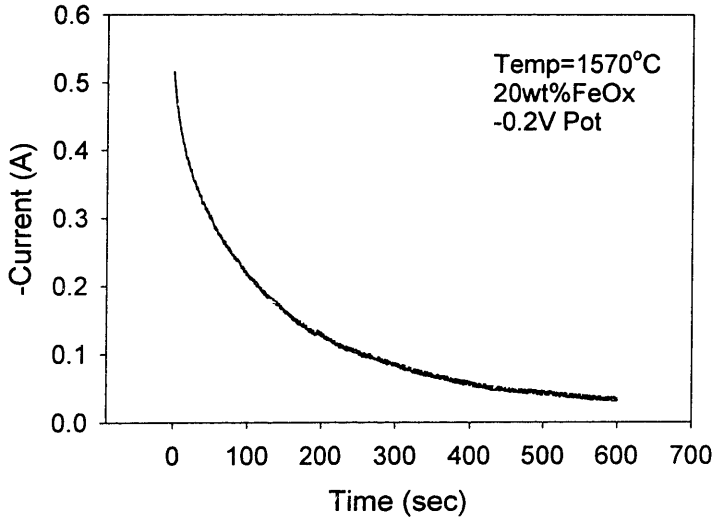

Figure 6.3 Total coulombs removed from OCV to each given applied potential. The modeled lines were made using γ_{rat}=1 and γ_{FeO}=2.5.

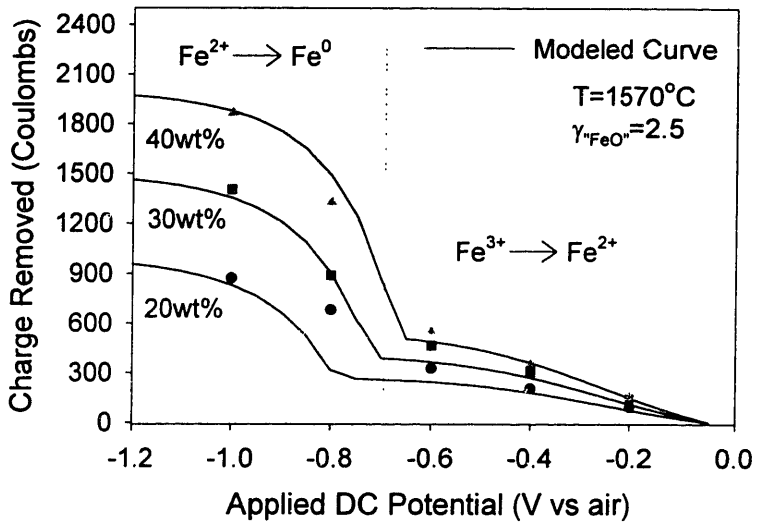

Figure 6.4 Cross-section of the cell after the coulometric titration experiment. Slag FeOx concentration was reduced from 20-40 wt%FeOx to 2-4 wt%FeOx.

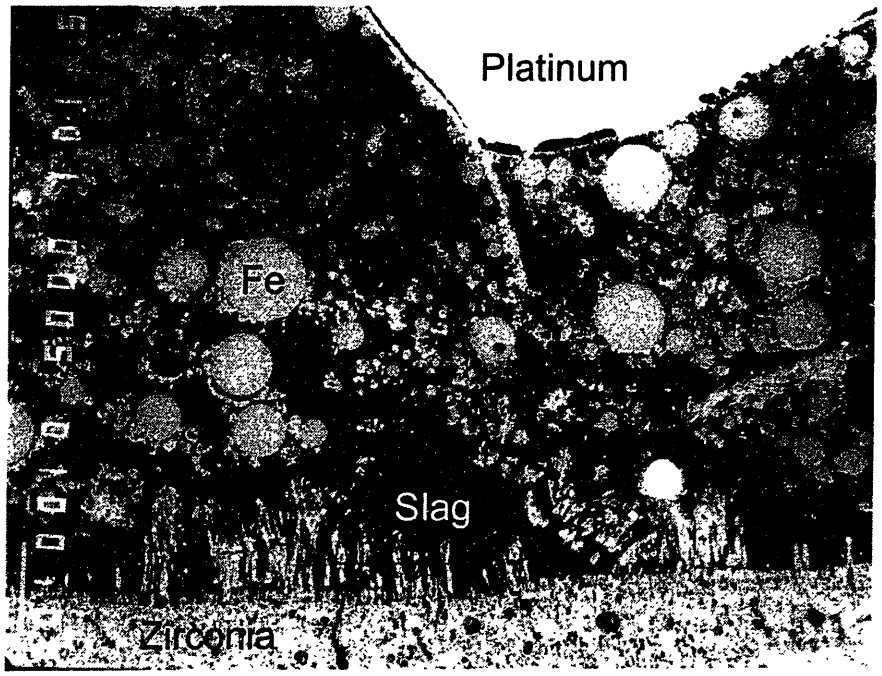

7 Conclusions

The use of amperometric techniques was shown to yield information which can supplement conventional open circuit potential (OCV) measurements. An OCV measurement simply yields the oxygen activity of the slag whereas an amperometric approach gathers information concerning the buffering capacity of the slag to a given oxidation state. The slags investigated in this thesis intentionally contained identical oxygen activities. Therefore, a simple OCV technique was unable to distinguish differences between the slags. However, amperometric techniques allowed the slags to be distinguished in terms of dissociable oxide concentration, dissociable oxide type, and solvent slag viscosity. Two different ranges of FeOx concentration were examined. 0-4 wt% low FeOx containing slags were investigated using DC applied potential steps and impedance frequency sweeps over a range of applied DC potentials. 20-40 wt% high FeOx containing slags were investigated using a coulometric titration technique.

Results obtained by applying DC potential steps and impedance frequency sweeps at applied DC potentials on the low FeOx slags were thoroughly modeled using appropriate kinetic equations and an equivalent circuit model. The parameters b_l/A and $\sigma_w A$, which were derived from the modeling, demonstrated strong proportionality with concentration. Therefore, b_l/A and $\sigma_w A$ can be used as sensing parameters for concentration. Using knowledge of appropriate thermodynamics concerning the slag structure, values for the diffusion coefficients of species reacting at the WE/slag interface were calculated. The values obtained compared well with values reported in the literature for similar slag structures. Amperometric measurements are sensitive to the buffering

capacity of the slag at a given oxidation state. By applying appropriate thermodynamic modeling to impedance frequency sweeps at different applied DC potentials allowed determination of the type of oxide species present. The influence of viscosity on transport properties was also examined. While b_l/A and $\sigma_w A$ parameters were sensitive to slag structures, high frequency impedance measurements describing overall slag conductivity provided a much better independent method for estimating slag structure changes.

Coulometric titration measurements on isolated volumes of high FeOx containing slags provided information concerning the concentration of FeOx. The membrane properties of the YSZ allowed oxygen associated with FeOx in the slag to be pumped out of the slag system. Therefore, the total coulombs removed yielded a quantitative estimate of the amount of FeOx initially present. During the measurement, slag containing 20-40wt% FeOx was reduced to slags containing 2-4% FeOx by the formation of liquid iron droplets. The current efficiency of this process was estimated to be quite large – approaching 100%. This technique demonstrated many advantages compared to direct electrolysis of iron using electrodes simply immersed into the electrolyte. Typical problems such as short circuiting, anode destruction, and reoxidation of iron units were avoided by using the membrane technique. Further discussion on the use of this technique for metals production can be found in the future work section.

The advantages of amperometric measurements has been demonstrated in this thesis. The following section will describe the packaging required to implement the process under steelmaking conditions. In addition, a theoretical model is included which describes the predicted benefits which can be obtained.

8 Future Work and Applications

8.1 Sensors for Steelmaking

This thesis has demonstrated that additional knowledge concerning solute concentration, oxide type, and buffering capacity can be obtained by using amperometric measurements. The next logical step would be to develop a prototype which can operate in a steelmaking furnace. A steelmaking furnace poses additional problems to those encountered in the laboratory. For example, steelmaking slags are typically far more basic than the SiO_2 rich slags investigated in the thesis. This would lead to more rapid corrosion of the ZrO_2 membrane than was measured in the laboratory. Therefore, the sensor is not expected to be a continuous on-line device but rather a single-use device similar to the conventional oxygen sensor. This will influence the methodology for obtaining desired information. Because of the short life span of the device, strict procedures for quickly obtaining the most desired information will have to be implemented. This is in contrast to the wide range of impedance frequency sweeps and potential steps which could be measured under lab conditions.

Metallurgists have found that conventional oxygen sensors demonstrate more reproducible results under steelmaking conditions when reference metal / metal oxide systems such as Cr / Cr_2O_3 are used instead of gaseous phases such as air. Therefore it is expected that a metal / metal oxide system will also perform better for the amperometric device. However, caution should be taken to ensure that the counter electrode can provide a sink for the removal of oxygen species without influencing the stability of the reference oxide or changing the composition of the measured phase.

Additional parameters which may influence sensor performance include slag fluid dynamics and furnace electrical interference. These parameters will differ from furnace to furnace and will have to be evaluated by running tests in industrial settings.

8.2 Electrolysis for Metals Production

Coulometric titration was examined for use in determining the concentration of easily dissociable oxide species in an isolated slag volume. The current efficiency measurement in this thesis approached 100%. Because of the high current efficiency a similar method could be used for the production of metals via electrolysis in order to replace conventional steelmaking techniques. The steel industry is one of the worlds largest producers of greenhouse gasses via the production of CO_2. Electrolysis methods would alleviate the need for carbon as a reducing agent thereby reducing CO_2 emissions.

The use of a zirconia membrane offers advantages over traditional electrolysis methods by preventing anode oxidation, reoxidation of reduced metallic species, electronic short circuiting and dendritic short-circuiting. In essence, the zirconia membrane acts to ensure oxygen removal from the molten oxide. Coulometric titration was demonstrated to be successful for the formation of Fe from high FeOx containing slags, however, further research on the economics of production need to be considered. Future research should be focused on the reactions between the zirconia and the slag as well as the types of metal which can be produced and the scale of economical production.

A. Appendix. Relationship between activity coefficients of equation 3.45 and 3.46.

Thermodynamic equations describing redox equilibrium between FeOx and oxygen partial pressure have been written as follows in the literature.

$$FeO + \frac{1}{4}O_2 = FeO_{1.5} \tag{A.1}$$

$$FeO + \frac{1}{4}O_2 = \frac{1}{2}Fe_2O_3 \tag{A.2}$$

The free energy for both reactions is identical and therefore:

$$K_{A1} = \left(\frac{a_{FeO_{1.5}}}{a_{FeO} P_{O_2}^{1/4}} \right) = K_{A2} = \left(\frac{a_{Fe_2O_3}^{1/2}}{a_{FeO} P_{O_2}^{1/4}} \right) \tag{A.3}$$

The following equation describes the relationship between the Fe^{3+} species.

$$2n_{Fe_2O_3} = n_{FeO_{1.5}} \tag{A.4}$$

Substituting mole fractions and activity coefficients for activities and inserting equation A.4 into equation A.3 the following general relationship is achieved relating the activity coefficient ratio derived for equation A.2 with the activity coefficient ratio derived for equation A.3.

$$\frac{\gamma_{Fe_2O_3}^{1/2}}{\gamma_{FeO}} = \frac{\gamma_{FeO_{1.5}}}{\gamma_{FeO}} \left(\frac{2 + \frac{X_{FeO_{1.5}}}{1 - X_{FeO_{1.5}}}}{\frac{X_{FeO_{1.5}}}{1 - X_{FeO_{1.5}}}} \right)^{1/2} \tag{A.5}$$

For small quantities of iron oxide in the slag the number of moles will have a negligible influence on the total number of moles in the slag:

$$2X_{Fe_2O_3} \approx X_{FeO_{1.5}} \tag{A.6}$$

Thereby simplifying equation A.5 as follows:

$$\frac{\gamma_{Fe_2O_3}^{1/2}}{\gamma_{FeO}} \approx \frac{\gamma_{FeO_{1.5}}}{\gamma_{FeO}} \left(\frac{2}{X_{FeO_{1.5}}} \right)^{1/2} \tag{A.7}$$

Equations A.5 and A.7 can then be used to compare γ_{rat} values between different reported literature values.

B. Appendix. Experimental Data concerning $FeO_{1.5}$/FeO equilibrium.

Experiments on the CaO-FeOx (figure B.1)[153] and SiO_2-FeOx (figure B.2) binaries have been summarized by Turkdogan[154]. The data is reported as a Fe^{3+}/Tot_{Fe} mole ratio – this can be converted to X_{rat} by the following equations:

$$X_{rat} = \frac{\left(\frac{n_{Fe^{3+}}}{n_{Fe_{total}}}\right)}{1-\left(\frac{n_{Fe^{3+}}}{n_{Fe_{total}}}\right)} = C_{rat} \tag{B.1}$$

$$\frac{n_{Fe^{3+}}}{n_{Fe_{total}}} = \frac{X_{rat}}{1+X_{rat}} = \frac{C_{Fe^{3+}}}{C_{Fe_{tot}}} \tag{B.2}$$

$$C_{Fe_{tot}} = C_{Fe^{2+}} + C_{Fe^{3+}} = \frac{2\rho_{slag} wt\%Fe_2O_3}{100 MW_{Fe_2O_3}} \tag{B.3}$$

These early measurements found that the addition of CaO yields higher concentrations of Fe^{3+} whereas the addition of SiO_2 yields lower concentrations for a given temperature and oxygen partial pressure. Timucin and Morris investigated the CaO-SiO_2-FeOx slag system[155] (figure B.3, B.4) and found similar trends as in the binaries. Quaternary systems have been investigated by Pargamin et al. where they considered additions of Al_2O_3 to CaO-SiO_2-FeOx containing slags[156]. In general γ_{rat} increases with for increasing slag basicity. Additions of Al_2O_3 also appear to effectively increase γ_{rat} by competing with Fe^{3+} ions for octahedral locations within the melt.

In general, changes in the total iron oxide concentration will NOT have a large effect on X_{rat} at a given temperature and oxygen partial pressure provided that the overall slag structure is not dramatically altered in the process. For low total iron concentrations (Henrian region) small changes in dilute concentrations of iron oxide would not be

expected to effect the overall slag structure and basicity. Ichise et al. demonstrated this Henrian behavior by investigating the changes in valance state of dilute iron oxide in $CaO-Al_2O_3-FeOx$ at 1873K[157] with small changes in total iron concentration (figure B.5). They noted that the influence of X_{FeOx} was negligible on X_{rat} in the Henrian region. Schreiber et al.[158] also reported negligible influence on X_{rat} with iron content for dilute $Al_2O_3-CaO-SiO_2-MgO-FeOx$ melts with 0.2-1.4% FeOx. Strangely, Jahanshahi and Wright[159] reported somewhat conflicting results for an Al_2O_3 saturated $CaO-Al_2O_3-SiO_2-FeOx$ slag in which the ratio of Fe^{3+}/Fe^{2+} became much greater with lower total iron content (figure B.6). This was most likely caused errors associated with either the Mossbauer or wet chemical analysis as discussed within the paper (p200) but it may have been due to near Al_2O_3 saturation in the system. Thus, for the Henrian region the influence of iron concentration can be neglected and γ_{rat} will be determined by a description of the overall slag structure by some measure of basicity or by comparison with similar slag structures existing in the literature. Bowker et al. have suggested that γ_{rat} decreases slightly for acidic slags when increasing concentrations of FeOx (up to 35%) are added to $CaO-SiO_2-FeOx$ containing slags[160] (figure B.7). This is because of the influence of FeOx on the surrounding slag structure at large concentrations.

Figure B.1 State of oxidation of iron in CaO-FeO-Fe_2O_3 melts at 1550^0C[153].

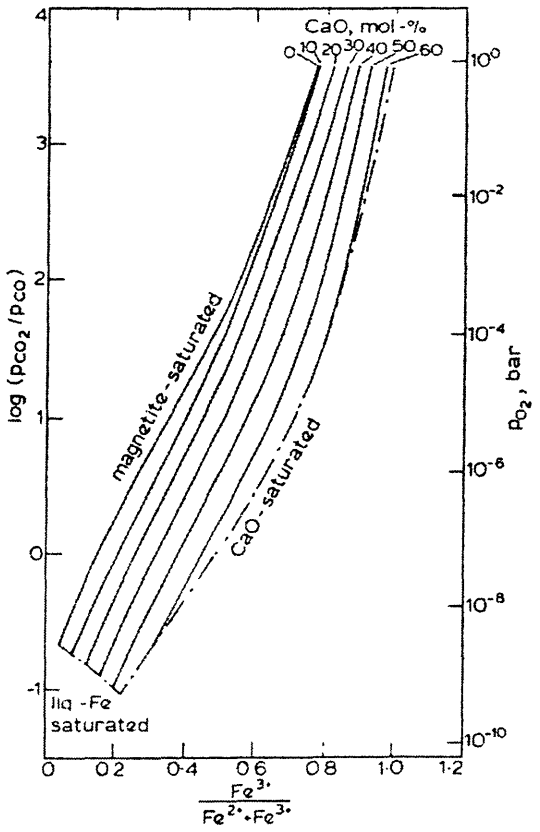

Figure B.2 State of oxidation of iron in SiO_2-FeO-Fe_2O_3 melts at 1550^0C[154].

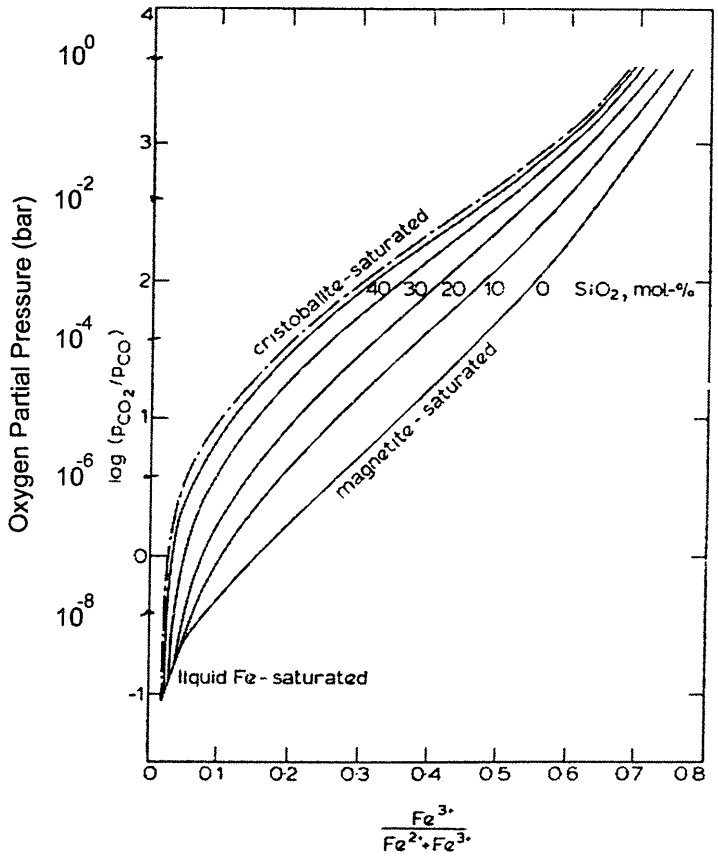

Figure B.3 The 30wt% SiO_2 isothermal phase diagram for the CaO-FeO-Fe_2O_3-SiO_2 system. L = Liquid oxide, C_2S = $2CaOSiO_2$[155].

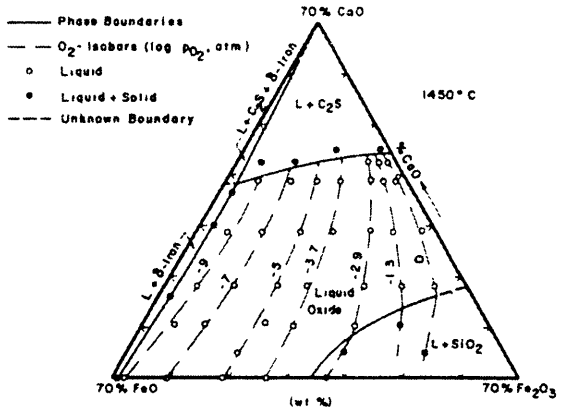

Figure B.4 The effect of silica additions on the relative Fe^{3+} stability of the CaO-FeO-Fe_2O_3-SiO_2 melts containing 20 wt% CaO[155].

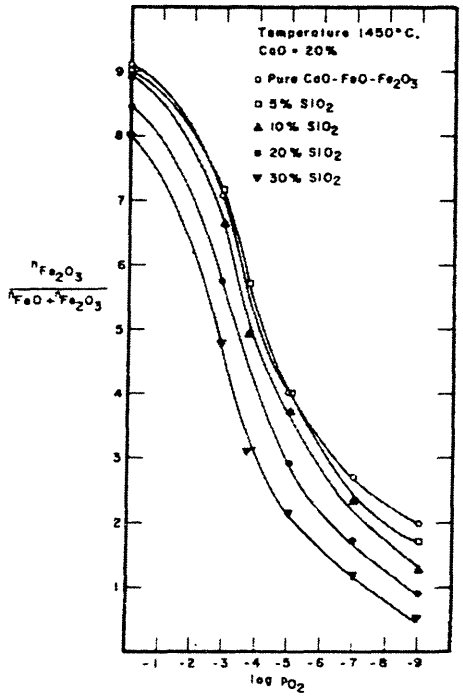

Figure B.5 Relationships between wt%Fe^{2+}/wt%Fe_{tot} and wt%tot for fluxes of $X_{CaO}/X_{Al2O3} = 61/39$[157].

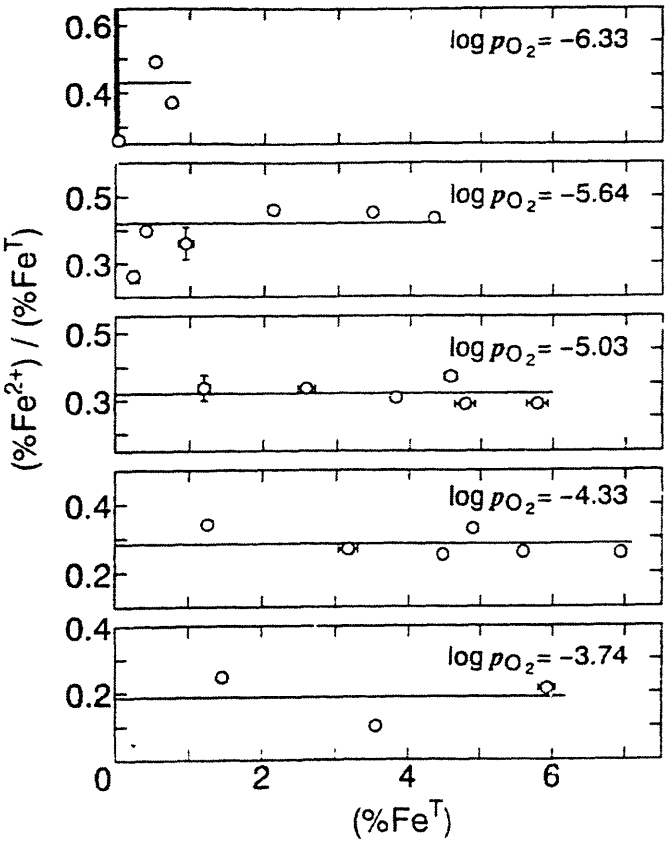

Figure B.6 Variation of Fe^{3+}/Fe^{2+} ratio with the total iron contents of slags at 1400°C[159].

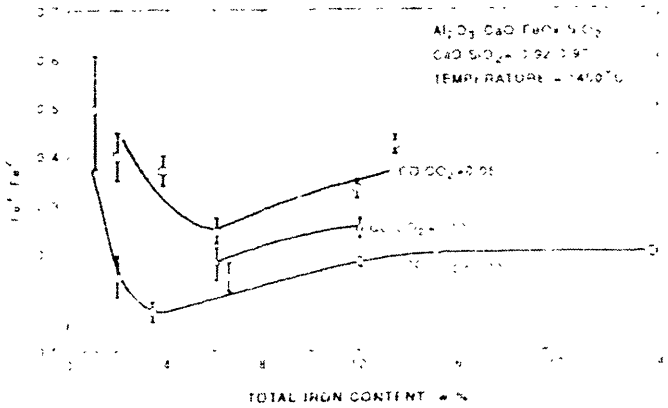

Figure B.7 State of oxidation of the iron cations in a series of slags represented by the formula $(0.55CaO\text{-}0.45SiO_2)_{100-y}(Fe_2O_3)_y$, where y is the wt% of Fe_2O_3[156]. Curve 1 is from Larson and Chipman[153] and Curve 2 is extrapolated from Phillips and Muan[161]. Taken from Bowker et al.[160].

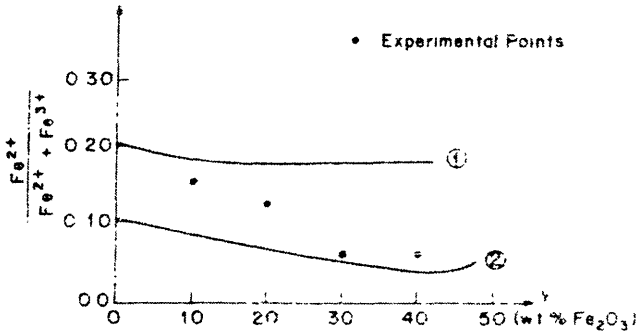

C. Appendix. Experimental data on concerning the Fe/FeO system.

Turkdogan[162] demonstrated a correlation between slag basicity and the activity coefficient of FeOx as shown in figure C.1. The measure of basicity has been defined in a variety of different ways in the literature[163]. Turkdogan uses as his measure of basicity the following relationship using the assumption that Al_2O_3 behaves identically to SiO_2 on a molar basis[162]:

$$B = \frac{\%CaO}{\%SiO_2 + 0.6 * \%Al_2O_3} \tag{C.1}$$

The reader should note that this definition of basicity is somewhat misleading for acidic slags because under such conditions Al_2O_3 is likely to behave in a more basic manner.

Experimental measurements of the a_{FeO} in equilibrium with pure Fe as a function of X_{FeO} can be found in the literature for a variety of slag systems[162,164,165,166,167,168,169]: figure C.2[168], figure C.3[169], and figure C.4[164]. Examination of the above figures reveals that for many systems the use of Raoults law (γ=1) is NOT a terrible approximation for the activity/concentration relationship between Fe/FeO.

Various solution models exist which attempt to use knowledge of the slag structure and composition to determine the relationship between concentration and activity. Different modeling approaches include the regular solution model, ideal mixing model, and structure related models as described by Turkdogan[170]. A recent article describing the Ca-Fe-O-Si system using an ionic two-sublattice model can be found in the literature[171]. Although the fit obtained by comparing modern solution modeling results with experimental data is improving, significant error is still a factor in such approaches. For this reason, this thesis does not attempt to use solution modeling in

order to determine the activity concentration relationship of the redox reaction of iron oxide with respect to slag structure.

Figure C.1 The effect of slag basicity is shown on the activity coefficient of iron oxide in simple and complex slags at temperatures of 1500°C to 1700°C[162].

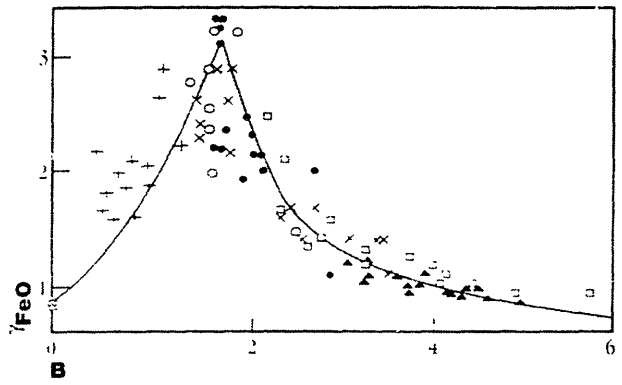

Figure C.2 Activity of FeO(l) in CaO-FeO-SiO_2 melts in equilibrium with liquid iron at 1550°C[168].

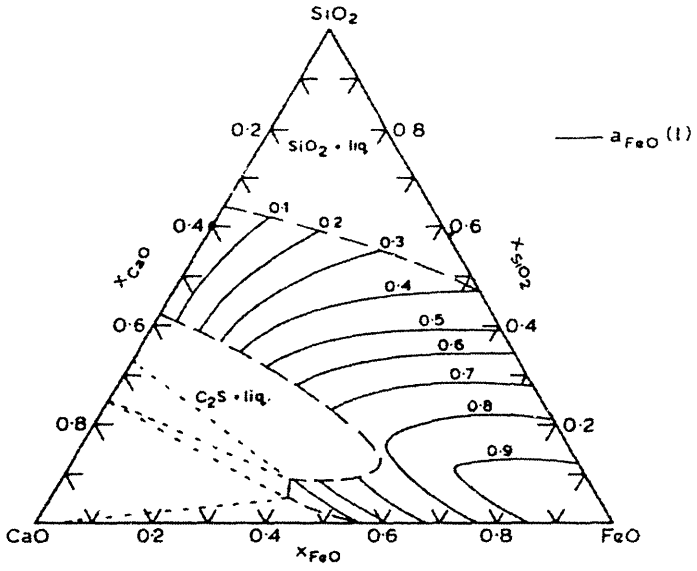

Figure C.3 Activity of 'FeO' in the system $CaO\text{-}FeO_n\text{-}SiO_2$ at 1600°C after Oerters. Taken from slag atlas[169].

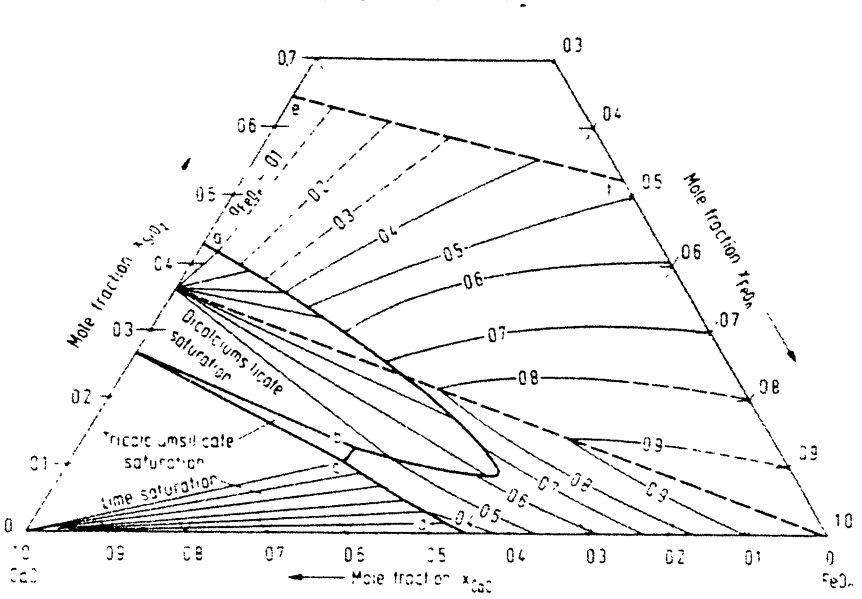

Figure C.4 Iso-activity curves for FeO in the system $CaO\text{-}SiO_2\text{-}FeO$ at 1673K[164].

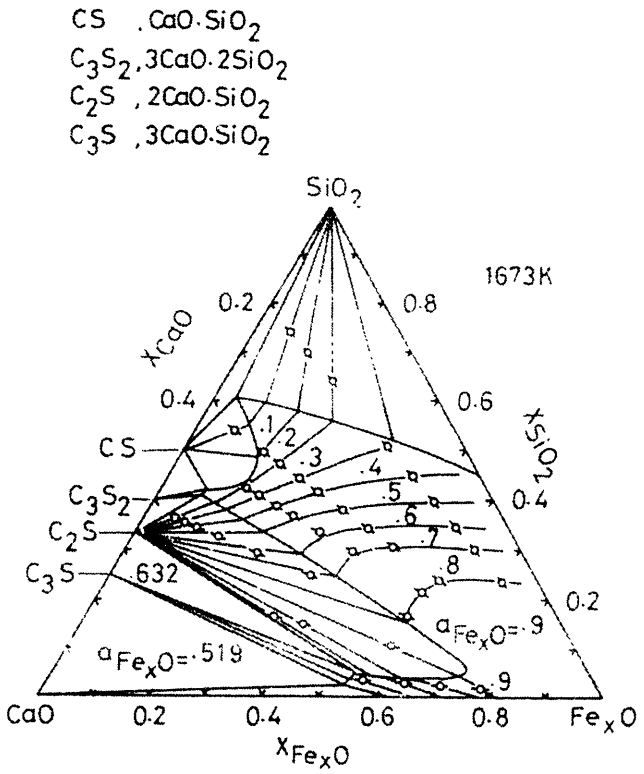

D. Appendix. Derivation of Equations 4.7 and 4.8 to estimate the potential drop along various electrode surfaces.

Thin Film Electrodes:

For a thin film electrode geometry, assume that the current density (i/A) is uniform over the entire electrode surface (no potential drop along the surface). All current must exit out of the top of the film (RE2 contact with WE at this point). The current as a function of the distance x from the top of the film is described by equation 1.

$$i(x) = \frac{i}{A} y(L - x) \qquad (1)$$

where i(x) is the current in the film at a distance x from the top (A), i/A is the current density (A/cm^2), y is the length of the film (cm), and L is the total height of the film (cm). The resistance of any increment (dx) in the film is given by equation 2.

$$R = \frac{dx}{ty\sigma} \qquad (2)$$

where R is the resistance of increment (dx) in the film (Ω), t is the film thickness (cm), σ the film conductivity, and y the length of the film (cm). The voltage drop across the total height of the film can then be estimated from equations 3 and 4.

$$V(x) = V_0 - \int_0^x \frac{i}{A} y(L - x) \frac{1}{\sigma t y} dx \qquad (3)$$

For x=L:

$$V(L) = V_0 - \frac{L^2}{2t\sigma} \frac{i}{A} \qquad (4)$$

In order to ensure that less than 1% voltage drop occurs across the electrode film the current density must not exceed the following value obtained from equation 5.

$$\frac{i}{A} \leq \frac{0.02\sigma t V_0}{L^2} \qquad (5)$$

Cylindrical wire electrodes

For a cylindrical wire geometry, assume that the current density (i/A) is uniform over the entire electrode surface (no potential drop along the surface). All current must exit out of the top of the electrode (RE2 contact with WE at this point). The current as a function of the distance x from the top of the wire is described by equation 6.

$$i(x) = \frac{i}{A} 2\pi r(L - x) \quad (6)$$

where i(x) is the current in the wire at a distance x from the top (A), i/A is the current density (A/cm^2), r is the radius of the wire (cm), and L is the total height of the film (cm). The resistance of any increment (dx) in the wire is given by equation 7.

$$R = \frac{dx}{\sigma \pi r^2} \qquad (7)$$

where R is the resistance of increment (dx) in the film (Ω), r is the wire radius (cm), and σ the film conductivity (1/Ω-cm). The voltage drop across the total height of the film can then be estimated from equations 8 and 9.

$$V(x) = V_0 - \int_0^x \frac{i}{A} 2\pi r(L - x) \frac{1}{\sigma \pi r^2} dx \quad (8)$$

For x=L:

$$V(L) = V_0 - \frac{L^2}{r\sigma}\frac{i}{A} \qquad (9)$$

In order to ensure that less than 1% voltage drop occurs across the electrode film the current density must not exceed the value obtained from equation 10.

$$\frac{i}{A} \leq \frac{0.01\sigma r V_0}{L^2} \qquad (10)$$

Conductivity values for various electrodes:

Pt wire electrode:

Metals become more resistive with increasing temperature because of the influence of atomic vibrations on the drift velocity of electrons. At 1500°C the conductivity of Pt is approximately 18050 (1/Ω-cm). For a radius of 0.01 inches, an applied potential of 0.2V and an immersion depth of 0.5cm the maximum current density to prevent a 1% voltage drop across the electrode would be approximately 3.66 A/cm^2 using equation 10. This is significantly larger than the currents measured in the diffusion limited regime. For example Fontana et. al.[172] reported charge transfer limiting current densities of approximately 10-30 A/cm^2 for Manganese oxidation at 1500°C in 40wt% SiO_2 (10-60wt%MnO) 0-50wt%CaO using chronopotentiometric techniques.

$LaSrCrO_3$ electrode:

The conductivity of $LaSrCrO_3$ and TiO_2 doped ZrO2 are approximately 5 (1/Ω-cm) at 1500°C. For a film thickness of 300 microns, an applied potential of 0.2V and a height of 0.5cm the maximum current density to prevent a 1% voltage drop across the

electrode would be approximately $2.4x10^{-5}$ A/cm^2 using equation 5. This is significantly lower than current densities measured during experiments within this thesis. Unless the film thickness is dramatically increased beyond that normally realized during slurry deposition, the potential drops within the electrode will add a significant source of error.

E. Appendix. Investigated cermet compositions and preparation techniques.

Composition	Firing Temp	Firing Time	Firing Atmosphere	Notes and Adherence
15gMo 4.2g ZrO_2 PVA unknown Viscous	1360C	~12hrs	H_2/H_2O then H_2	Adherence pretty good some flaking - some good
	1200C+ 1100C Infiltrated	~12hrs ~7hrs	H_2/H_2O then H_2	About the same adherence some flaking - some good
6,13,25,33 wt% ZrO_2 Balance MO 40 wt% PVA	1500C	17hrs	H_2/H_2O then H_2	All about the same adherence. Can easily be flaked off but will stay on ZrO_2
25 wt% ZrO_2 33 wt% PVA 75 wt% Mo	1500C	17hrs	H_2/H_2O	Samples did not adhere well and appeared oxidized. Some Mo metal remained on ZrO_2 surface and was VERY adherent
50 wt% ZrO_2 PVA unknown Mortar and Pestle 50 wt% Mo	1500C	17hrs	H_2/H_2O then H_2	Samples had bad dispersion but was pretty adherent. Cracking and cermet removal but firmly attached Cermet was non-conductive
TiO_2 doped ZrO_2 from Worrell	1500C	17hrs	H_2/H_2O then H_2	Sample was VERY adherent.
100 wt% ZrO_2 40 % PVA	1500C	17hrs	AIR	Sample very cracked, sort of adherent - need to scrape off.
100 wt% ZrO_2 unknown PVA ZrO_2 Milled for one week	1500C	17hrs	AIR	Sample had bad dispersion but was pretty adherent. More adherent than for unmilled ZrO_2. Difficult to scrape off.
100 wt% ZrO_2 40 % PVA or 20% H_2O	1500C	17hrs	H_2/H_2O then H_2	Samples were same as 100% above.
Mixture of ZrO_2 and Pt ink	1500C	17hrs	H_2/H_2O then H_2	Samples had better adherence than 100% ZrO_2 but poor dispersion and uniformity
ZrO_2 on Pt ink pre and post sintered	1500C	17hrs	H_2/H_2O then H_2	Pt adhered OK ZrO_2 did not adhere well on top of Pt
TiO_2 doped ZrO_2	1500C	17hrs	H_2/H_2O then H_2	Very adherent (fully dense)

F. Appendix. Conductivity Approximations.

The conductivity of the slag can be estimated using HF impedance measurements because at high frequencies the Z' term of the impedance approaches R_{sol}. Assuming that a single WE wire is centered in the tube as shown in figure 5.1c the conductivity of the slag can be estimated as follows:

$$R_{sol} = \int_{r_1}^{r_2} \frac{dr}{A\sigma_{slag}} \tag{F.1}$$

$$A = 2\pi rh \tag{F.2}$$

where R_{sol} is the overall solution resistance (Ω), r is the radius of interest (cm), A is the surface area (cm^2), h is the height of the WE (cm), and σ_{slag} is the slag conductivity (Ω^{-1}-cm^{-1}).

σ_{slag} can be solved for using equation F.3 which describes R_{sol} over both the slag and zirconia phases.

$$R_{sol} = R_{ZrO_2} + R_{Slag} = \frac{1}{2\pi h_{wire}}\left(\frac{\ln\left(\frac{r_{ID}}{r_{wire}}\right)}{\sigma_{slag}} + \frac{\ln\left(\frac{r_{OD}}{r_{ID}}\right)}{\sigma_{ZrO_2}}\right) \tag{F.3}$$

where h is the height of the wire, σ_{slag} is the conductivity of the slag, σ_{ZrO2} is the conductivity of the zirconia, r_{ID}, r_{OD}, and r_{wire} are the respective radii.

Equation F.3 assumes the "ideal" case where the end effects are negligible, the WE is perfectly centered within the slag phase, and only one WE is utilized. End effects would tend to yield higher σ_{slag} values than are actually present because equation F.3 does not describe all of the current paths available to the system. As the electrode is lowered into the slag HF impedance measurements were taken at different immersion depths. Assuming that the final depth demonstrates negligible immersion, R_{sol} "ideal" is

plotted on the graph along with the measured data for the H2 case (1 wire). R_{sol} "ideal" can be calculated as follows.

$$R_{sol} = R_{fin}\frac{h_{fin}}{h} \tag{F.4}$$

As expected the predicted resistance from equation F.3 is always larger than the measured cell resistance – the effect becoming more pronounced as the end-effects play a larger roll in the overall cell conductivity. The slag conductivity for the H2 case with one wire can be estimated by simply using equation F.3 and assuming that at the final depth the end-effects play only a minor roll.

Most experiments utilized a type A or B setup with two immersed wires rather than the type C setup as in the above case (see figures 5.1a-c). It is substantially more difficult to calculate the R_{sol} equation for the type A and B setups. Instead an empirical solution was obtained. Both a two wire and a single wire immersion case was conducted for the H2 slag. The percentage differences between the two cases were measured at each depth and then compared with the resistance measured at the final depth (0.55cm) for the single wire, double wire, and ideal cases. The percentage differences were almost identical for the single and double wire cases indicating that end effects account for the remaining fraction. An empirical cell correction factor, X, was developed in order to correspond the R_{sol} value obtained for two wires into an R_{sol} value which would have been obtained with one wire.

$$R_{sol,1} = XR_{sol,2} \tag{F.5}$$

From the H2 experiment X was determined to be 1.4. Using the correlation factor X, R_{sol} values from the impedance data, and equation 3, conductivity values for each of the slags used in the low concentration measurements were estimated. Figure 5.22 demonstrates

the estimated results and the expected conductivity values determined in the slag characterization section. The values of conductivity determined using the present method yielded slightly higher conductivities than were reported in the slag characterization section. This is most likely attributed to the fact that end-effects have not been entirely eliminated and the WE is not perfectly centered within the tube. Both of these effects would lead to a slightly higher predicted conductivity than actual. If slag conductivity was the parameter of importance in the sensor greater care would have been taken to more closely standardize the cell geometry for conductivity measurements. The above exercise demonstrates several important things:

1. The transport number of iron remains less than 0.2 even at 4wt% Fe, this is similar to the value predicted by the Themilis regression data.
2. While the measured current is directly proportional to the iron content, the conductivity is not directly proportional – i.e. this was not developed to be a conductivity measuring device.
3. The sensor can ALSO yield useful information concerning the slag conductivity in the same measurement.

Use of HF measurements to standardize the surface area for L type slag measurements:

The HF impedance measurements were also used to standardize the L type slag measurements which demonstrated ZrO_2 corrosion and a lowering of the slag height with time. When the electrode was lowered into the slag several HF impedance measurements were taken as a function of distance in order to determine the cell resistance as a function

of electrode depth (step 2 of section 5.1.3). The parameter k(h) was found to be universal for all H type slags.

$$k(h) = \frac{R_{sol}(h)}{R_{sol}(0.55)} \tag{F.6}$$

where $R_{sol}(h)$ is the solution resistance at immersion depth h (Ω) and $R_{sol}(0.55)$ is the solution resistance at immersion depth 0.55cm (Ω).

The immersion data for 4wt%FeOx L type experiment was best fit to yield the following equation for $k(h)_{low}$.

$$k(h)_{low} = 2.012 - 3.9h + \frac{0.047}{h} + 3.48h^2 \tag{F.7}$$

Using equations F.6 and F.7, R_{sol} values taken during the L type slag experiments were converted into electrode immersion depths corresponding to the surface area of the electrode in the slag. The first impedance measurement made at a depth of 0.55cm was used as the $R_{sol}(0.55)$ value. Subsequent measurements were used to calculate a new h value for the electrode. The surface areas calculated from the above standardization procedure are the ones used in the b_1/A and $\sigma_W A$ calculations. H type slags did not demonstrate any corrosion or R_{sol} variation during measurement and hence no correction to the surface area was required.

G. Appendix. Oxygen sensor used for experiments.

The oxygen sensor used for the experiments in this thesis was constructed in the laboratory. The sensor, depicted in figure G.1, consisted of a one end closed ZDY-4 Coors tube (12" x 0.4" OD x 0.3" ID) located in a furnace with air atmosphere at 875°C. Furnace exit gas was passed into the sensor using a series of swagelocks and an Al_2O_3 double-bored tube. The electrode in contact with the unknown gas consisted of 0.02" Pt and Pt/Rh wires pressed and attached to the zirconia using platinum ink (Engelhard #6926). The internal wires also acted as an S-type thermocouple. The electrode in contact with air consisted of a 0.01" Pt wire attached to the zirconia using platinum ink. The potential measured between the two electrodes reveals the oxygen partial pressure of the unknown argon phase using equation G.1.

$$E = \frac{RT}{4F} \ln\left(\frac{P_{O_2}^{Ar}}{P_{O_2}^{air}}\right) \qquad \text{(G.1)}$$

Figure G.1 Schematic of oxygen sensor used for experiments.

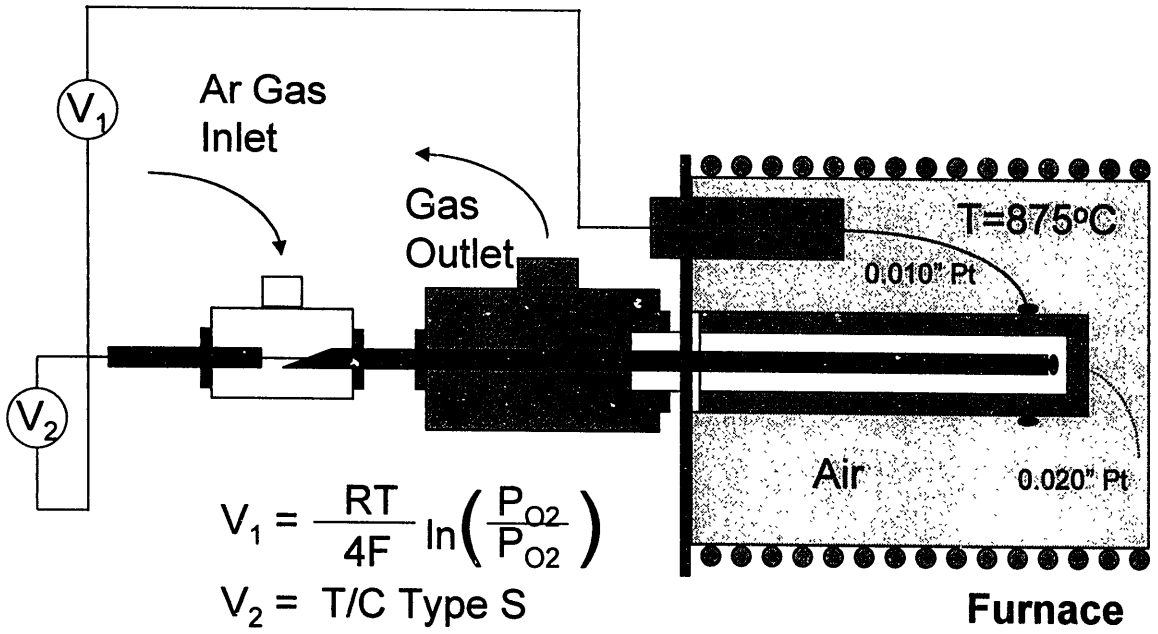

H. Appendix. Reference gas phase.

Often it is not possible to use an air reference as was used in the current investigation. In order to compare the results measured in this thesis with other data present in the literature this appendix will compute the potential difference between an air reference and several other typically used reference phases. For a reference phase of a known oxygen activity the difference in potential would be given by equation H.1.

$$E = \frac{RT}{4F}\ln(0.21) - \frac{RT}{4F}\ln\left(P_{O_2}^{REF}\right) \tag{H.1}$$

For metal / metal oxide references with activity of 1, the difference in potential would be given by equation H.2.

$$E = E_o^{ref} + \frac{RT}{4F}\ln(0.21) \tag{H.2}$$

where

$$E_0^{ref} = \frac{-\Delta G_0^{ref}}{nF} \tag{H.3}$$

ΔG_0^{ref} values can be computed from data available in the literature[173]. The following is a list of ΔG_0^{ref} values for commonly used reference metal / metal oxides (in J).

$$\Delta G_0^{Cr/Cr_2O_3} = -1130900 + 257T \tag{H.4}$$

$$\Delta G_0^{Mo/MoO_2} = -548050 + 143T \tag{H.5}$$

$$\Delta G_0^{Ni/NiO} = -252850 + 95T \tag{H.6}$$

When the reference gas phase is a mixture of buffer gasses the potential would be given by equation 7 and 8 for H_2/H_2O and CO/CO_2 respectively.

$$E = E_o^{H_2/H_2O} + \frac{RT}{4F}\ln(0.21) + \frac{RT}{2F}\ln\left(\frac{P_{H_2}}{P_{H_2O}}\right) \quad \text{(H.7)}$$

$$E = E_o^{CO/CO_2} + \frac{RT}{4F}\ln(0.21) + \frac{RT}{2F}\ln\left(\frac{P_{CO}}{P_{CO_2}}\right) \quad \text{(H.8)}$$

where ΔG_0^{ref} for the two buffer gas mixtures[173]:

$$\Delta G_0^{H/H_2O} = -252240 + 58.4T \quad \text{(H.9)}$$

$$\Delta G_0^{CO/CO_2} = -278865 + 84.5T \quad \text{(H.10)}$$

Using the above equations a relationship between the potentials measured in this thesis and the potentials measured in the literature can be compared quickly and easily.

I. Appendix. Derivation of redox diffusion to WE interface.

In order to solve the problem of diffusion at the WE under an applied potential the following linear diffusion equations must be solved assuming planar conditions.

$$\frac{dC_O(x,t)}{dt} = D_O \frac{d^2C_O(x,t)}{dx^2} \tag{I.1}$$

$$\frac{dC_R(x,t)}{dt} = D_R \frac{d^2C_R(x,t)}{dx^2} \tag{I.2}$$

The following boundary conditions are present in the system.

$$C_O(x,0) = C_O^{Bulk} \tag{I.3}$$

$$\lim_{x\to\infty} C_O(x,t) = C_O^{Bulk} \tag{I.4}$$

$$C_R(x,0) = C_R^{Bulk} \tag{I.5}$$

$$\lim_{x\to\infty} C_R(x,t) = C_R^{Bulk} \tag{I.6}$$

Where O is Fe^{3+} and R is Fe^{2+} and conservation of mass is employed (sorry Einstein).

$$D_O\left(\frac{dC_O(x,t)}{dx}\right)_{x=0} + D_R\left(\frac{dC_R(x,t)}{dx}\right)_{x=0} = 0 \tag{I.7}$$

The above equations are solved with respect to time for the condition where an applied potential step imposes the following surface conditions on the electrode surface as described by equation 5.33.

$$E = E_0 + \frac{RT}{nF}\ln\left(\frac{C_O(0,t)}{C_R(0,t)}\right) \tag{I.8}$$

Solving the above equations using Laplace equations, yields the following current-potential-time profile relationship:

$$i(t) = \frac{(n_O - n_R)FA\left(C_O^B - \theta C_R^B\right)}{(1+\xi\theta)}\sqrt{\frac{D_O}{t\pi}} \tag{I.9}$$

where:

$$\theta = \frac{C_O(0,t)}{C_R(0,t)} = \exp\left(\frac{nF}{RT}(E - E_0)\right) \tag{I.10}$$

$$\xi = \sqrt{\frac{D_O}{D_R}} \tag{I.11}$$

J. Appendix. CNLS fitting techniques.

The acquired impedance frequency sweep data was best fit to a Randles type equivalent circuit (figure 5.6) using a complex non-linear least squares immittance fitting program provided with ZView from Solartron Instruments. The error was calculated using the Calc-Modulus mode which normalizes the magnitude of each data point. The data were fit over a frequency range of 20kHz to 100Hz and generally demonstrated very good fit to the finalized parameters of R_{sol}, C_{dl}, R_{ct}, and σ_W. More information concerning CNLS fitting can be found in references by J. Ross Macdonald[174,175].

K. Appendix. Sensitivity of different techniques on the total FeOx concentration.

The sensitivity of different parameters for the detection of FeOx concentration was computed for b_1/A, $\sigma_W A$, and cell conductivity.

Sensitivity is determined for the –0.4V applied DC potential in equation K.1.

$$Sensitivity_{DCstep} = \frac{\left(\frac{d\frac{b_1}{A}}{dwt\%}\right)}{\frac{b_1}{A}(2wt\%)} = \frac{-0.02303}{-0.0295} = 0.7807 \qquad \text{(K.1)}$$

Sensitivity is determined for the –0.4V impedance frequency sweep in equation K.2.

$$Sensitivity = \frac{\sigma_W A_{(2wt\%)}}{\left(\frac{d\sigma_W A}{d\,1/wt\%}\right)} = \frac{1.81}{2.39} = 0.757 \qquad \text{(K.2)}$$

Sensitivity is determined for the cell conductivity in equation K.3.

$$Sensitivity = \frac{\left(\frac{d\sigma}{dwt\%}\right)}{\sigma_{(2wt\%)}} = \frac{0.006153}{0.12709} = 0.0484 \qquad \text{(K.3)}$$

Sensitivity is in units of 1/wt%

Equations K.1-K.3 reveal that the parameters $\sigma_W A$ and b_1/A are quite sensitive to the FeOx concentration whereas the cell conductivity is not very sensitive. The low sensitivity of the conduction parameter to the FeOx concentration in this concentration range causes difficulty in resolving concentration effects from geometry induced error effects present in the cell design. For example, the standard deviation of the data from the regression line was calculated to be 0.00579 which is of the same order as the change in conductivity with change in wt% in equation K.3.

L. Appendix. Discussion of b_0 influences.

As described in equation 5.66, b_0 may be dependent on several different cell phenomenon.

$$b_0 = b_{cyl} + b_{rxn} + b_{bl} \tag{L.1}$$

After long times a boundary layer may develop at which point the steady-state current would be given by equation L.2 for b_{bl}.

$$b_{bl} = nFAD_i \frac{\left(C_i^{ocv} - C_i^{app}\right)}{\delta} \tag{L.2}$$

b_{bl} would therefore be quite sensitive to the boundary layer thickness developed in the system and may be difficult to control between setups.

A reaction occurring at the gas/slag/WE three phase interface may yield a constant current if the rate limitation was in the gas phase. However, b_{rxn} is expected to be quite small because argon was used as a protective gas and the three-phase interfacial area is small compared with the electrode surface area.

Since the electrode geometry is actually cylindrical rather than planar if the response to a cylindrical coordinate frame is plotted vs 1/sqrt(t) the response will appear to have a steady-state value at long times yielding a b_{cyl} value. The response of a single diffusing species to a cylindrical electrode has been solved explicitly by Hladik[176].

$$\left[\frac{dC(r,t)}{dr}\right]_{r=r_0} = \frac{4C^0}{r_0\pi^2}\int_0^\infty \frac{e^{-Dx^2t}}{x\left[J_0^2(r_0x)+Y_0^2(r_0x)\right]}dx \tag{L.3}$$

where J_0 and Y_0 are zero-order bessel functions of the first and second kinds respectively. The current is then represented by equation L.4.

$$i = nFAD\left[\frac{dC(r,t)}{dr}\right]_{r=r_0} \tag{L.4}$$

The current approaches zero very slowly and therefore a constant "steady-state" value may appear when the response is plotted vs 1/sqrt(t).

The program located at the end of this appendix was written in Mathematica in order to numerically calculate the solution to equation L.3 for the geometry of the setup used in the thesis. The following information must be input as constants: density, #wires in slag, depth of immersion in slag. The writematrix command allows for the data to be saved within a file "caseX" where the four inputs to mymatrix are as follows: electrode radius, diffusion coefficient, n, and wt% FeOx respectively.

Figure L.1 shows the typical results of the simulation. Depending upon the parameters chosen, b_0 values could be obtained on the same order as the ones measured in the thesis. This model was developed for the diffusion of only a single species to the electrode surface whereas the cell conditions had one species diffusing toward and another away from the electrode surface. A model describing this case is very complex and is beyond the scope of this thesis. However, this appendix has demonstrated the possible influence of cylindrical coordinates and the multiple parameters which may influence b_0 values. Therefore, b_0 was not considered as a useful sensing parameter.

Figure L.1 Simulation using model written in Mathematica for approximating cylindrical coordinates.

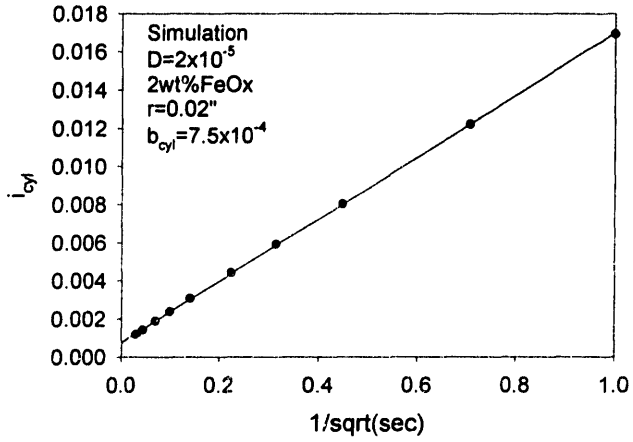

```
time = Join[Range[1, 101, 10], Range[201, 1101, 100]]
```

```
{1, 11, 21, 31, 41, 51, 61, 71, 81, 91, 101, 201,
 301, 401, 501, 601, 701, 801, 901, 1001, 1101}
```

```
time = {1, 2, 5, 10, 20, 50, 100, 200, 500, 1000}
```

```
{1, 2, 5, 10, 20, 50, 100, 200, 500, 1000}
```

```
f = 96320
```

```
96320
```

```
helper[a_, b_, c_] = {a, b, c}
```

```
{a, b, c}
```

```
density = 2.6
```

```
2.6
```

```
mwfe2o3 = 160
```

```
160
```

```
c0[wt_] = (.000456 - .0000884) * wt
```

```
0.0003676 wt
```

```
wire = 1
```

```
1
```

```
area = 2 * π * r0 * h
```

```
3.45575 r0
```

```
h = .55
```

```
0.55
```

```
plan[t_] =
 wire * n * f * area * Sqrt[d] * c0[wt] / Sqrt[t * π]
```

$$\frac{69.1517\ \sqrt{d}\ n\ r0\ wt}{\sqrt{t}}$$

```
cyl[t_] = (wire * n * f * area * d * 4 * c0[wt] / (r0 * π^2)) *
 NIntegrate[(E^(-d * x^2 * t)) /
   (x * (BesselJ[0, r0 * x]^2 + BesselY[0, r0 * x]^2)),
  {x, 0, 1000}]
```

NIntegrate::inum : Integrand $\frac{0.002\ \text{<<20>>}^{-\text{<<8>>}\ \text{<<1>>}\ t}}{\text{<<1>>}^2 + \text{<<1>>}^2}$ is not numerical at {x} = {500}.

NIntegrate::inum : Integrand $\frac{0.002\ \text{<<20>>}^{-\text{<<8>>}\ \text{<<1>>}\ t}}{\text{<<1>>}^2 + \text{<<1>>}^2}$ is not numerical at {x} = {500}.

```
49.675 d n wt
```

$$\text{NIntegrate}\left[\frac{E^{-d\,x^2\,t}}{x\,(\text{BesselJ}[0,\ r0\,x]^2 + \text{BesselY}[0,\ r0\,x]^2)},\ \{x,\ 0,\ 1000\}\right]$$

```
45.4318387321504335` d n t
```

$$\text{NIntegrate}\left[\frac{E^{-d\,x^2\,t}}{x\,(\text{BesselJ}[0,\ r0\,x]^2 + \text{BesselY}[0,\ r0\,x]^2)},\ \{x,\ 0,\ 1000\}\right]$$

NIntegrate::inum : Integrand $\frac{0.002\ \text{<<20>>}^{-\text{<<8>>}\ \text{<<1>>}\ t}}{\text{<<1>>}^2 + \text{<<1>>}^2}$ is not numerical at {x} = {500}.

```
45.4318 d n t
```

$$\text{NIntegrate}\left[\frac{E^{-d\,x^2\,t}}{x\,(\text{BesselJ}[0,\ r0\,x]^2 + \text{BesselY}[0,\ r0\,x]^2)},\ \{x,\ 0,\ 1000\}\right]$$

```
WriteMatrix[filename_String,
 data_List, separator_String: "\t"] :=
With[{myfile = OpenWrite[filename]},
 Scan[(WriteString[myfile, First[#]];
   Scan[
     WriteString[myfile, separator, #]&, Rest[#]];
   WriteString[myfile, "\n"])&, data];
 Close[myfile]]
```

```
mymatrix[r0_, d_, n_, wt_] =
 Join[{{"r0", "d", "n", "wt"}},
  {{r0, d, n, wt}}, {{"cyl", "plan", "time"}}, Thread[
   helper[Map[cyl, time], Map[plan, time], time]]];
```

NIntegrate::inum : Integrand $\frac{0.002\ \text{<<20>>}^{-\text{<<8>>}\,d}}{\text{<<1>>}^2 + \text{<<1>>}^2}$ is not numerical at {x} = {500}.

NIntegrate::inum : Integrand $\frac{0.002\ \text{<<20>>}^{-\text{<<8>>}\,d}}{\text{<<1>>}^2 + \text{<<1>>}^2}$ is not numerical at {x} = {500}.

NIntegrate::inum : Integrand $\frac{0.002\ \text{<<20>>}^{-\text{<<8>>}\,d}}{\text{<<1>>}^2 + \text{<<1>>}^2}$ is not numerical at {x} = {500}.

```
General::stop :
 Further output of NIntegrate::inum will be
   suppressed during this calculation.
```

```
WriteMatrix["0913b", mymatrix[.0254, .0000167, 1, 1],
 "     "]
```

```
0913b
```

```
WriteMatrix["0703b",
 mymatrix[2.54 * .015, .000005, 1, 2], "     "]
```

```
0703b
```

```
WriteMatrix["0703c",
 mymatrix[2.54 * .02, .00001, 1, 2], "     "]
```

```
0703c
```

```
WriteMatrix["0703d",
 mymatrix[2.54 * .02, .00002, 1, 2], "     "]
```

```
case4
```

```
WriteMatrix["0703e",
 mymatrix[2.54 * .02, .000025, 1, 2], "     "]
```

```
case5
```

```
WriteMatrix["0703f",
 mymatrix[2.54 * .02, .00003, 1, 2], "      "]
```

```
case6
```

```
! ! 0703 f
```

[1] M. Iwase, T. Mori. Transactions ISIJ. "Problems in Oxygen Sensors for Steelmaking". 19, 1979, p126-132.

[2] K. Goto. "Chapter 11: Solid-oxide Oxygen Sensors for the Steelmaking Industry", Solid State Electrochemistry and its Applications to Sensors and Electronic Devices, Elsevier, NY, 1988.

[3] E. Subbarao, H. Maiti. "Oxygen Sensors and Pumps", Science and Technology of Zirconia III. S. Somiya, N. Yamamoto, H. Hanagida edts. The American Ceramic Society, 1988, p731-747.

[4] D. Janke. "Oxygen Sensing in Iron and Steelmaking". Science and Technology of Zirconia II. N. Clausen, M. Ruhle, A. Heuer, edts. The American Ceramic Society, 1984, p636-646.

[5] W. Lankford, N. Samways, R. Craven, R. McGannon edts. The Making, Shaping and Treating of Steel. 10th Edition. Association of Iron and Steel Engineers, 1985, p749.

[6] E. Turkdogan et al. "Implementation of a Ladle Slag Oxygen Activity Sensor to Optimize Ladle Slag Practices at the US Steel Mon Valley Works". Iron and Steelmaker. July, 1997, p33-39.

[7] M. Kawakami, K. Goto, M. Matsuoka. "A Solid Electrolyte Oxygen Sensor for Steelmaking Slags of the Basic Oxygen Converter". Metallurgical Transactions B. 11B, 1980, p463-469.

[8] M. Van Wijngaarden, R. Dippenaar. "The use of zirconia-based solid electrolytes for the rapid determination of iron oxide activities in iron- and steel-making slags". J. S. Afr. Inst. Min. Metall. 86, 1986, p443-453.

[9] M. Iwase et al. "Activity Determinator for the Automatic Measurements of the Chemical Potentials of FeO in Metallurgical Slags". Metallurgical Transactions B. 23B, 1992, p459-466.

[10] M. Iwase et al. "Automatic Determinator for the FeO Activities in Metallurgical Slags Based on an Electrochemical Technique". 4th International Conference on Molten Slags and Fluxes, 1992, Sendai, ISIJ.

[11] S. Otsuka, Z. Kozuka. "A New Type of Oxygen Analyzer Utilizing a Potentiostatic Coulometric Titration Technique". Metallurgical Transactions B. 16B, 1985, p113-119.

[12] B. Liaw, J. Liu, W. Weppner. "Amperometric Tetragonal Zirconia Sensors", Science and Technology of Zirconia V. S. Badwal, M. Bannister, R. Hannink edts. Technomic Publishing Company, 1993. p611-622.

[13] A. Azad, K. Goto, et al. "Solid-State Gas Sensors: A Review". J. Electrochemical Society. 139, 1992, p3690-3704.

[14] R. Copcutt, W. Maskell. "CO/CO_2 electrochemistry on zirconia electrolyte with platinum electrodes in relation to amperometric oxygen sensors". Solid State Ionics. 53-56, 1992, p119-125.

[15] M. Oberg, R. Rapp et al. "The Diffusivity and Solubility of Oxygen in Liquid Copper and Liquid Silver from Electrochemical Measurements". Metallurgical Transactions. 4, 1973, p61-67.

[16] Z. Hasham, U. Pal, K. Chou. "Deoxidation of Molten Steel Using a Short-Circuited Solid Oxide Electrochemical Cell". J. Electrochem. Soc. 142, 1995, p469-475.

[17] S. Yuan, U. Pal, K. Chou. "Deoxidation of Molten Metals by Short Circuiting Yttria-Stabilized Zirconia Electrolyte Cell". J. Electrochem. Soc. 141, 1994, p 467-474.

[18] K. Oberg, R. Rapp, et al. "Electrochemical Deoxidation of Induction-Stirred Copper Melts". Metallurgical Transactions. 4, 1973, p75-82.

[19] R. Odle, R. Rapp. "Further Study of the Electrochemical Deoxidation of Induction-Stirred Copper Melts". Metallurgical Transactions B. 8B, 1977, p581-589.

[20] N. Minh. "Ceramic Fuel Cells". J. Am. Ceram. Soc. 76, 1993, p563-588.

[21] S. Otsuka, Z. Kozuka. "Application of a Potentiostatic Coulometric Titration Technique for an Oxygen Analyzer". Trans. Japan Institute of Metals. 25, 1984, p639-648.

[22] W. Worrell. "Chapter 6: Oxide Solid Electrolytes". Solid Electrolytes. S. Geller edt. Springer-Verlag 1977. p160.

[23] A. Bard, L. Faulkner. Electrochemical Methods: Fundamentals and Applications. John Wiley and Sons, 1980.

[24] K. Vetter. Electrochemical Kinetics: Theoretical Aspects. Academic Press, 1967.

[25] W. Dickson, E. Dismukes. "The Electrolysis of $FeO-CaO-SiO_2$ Melts". Trans AIME. 224, 1962, p505-511.

[26] K. Goto. "Chapter 9: Electrochemical Kinetics at the interface between metals and liquid oxides with ionic conduction". Solid State Electrochemistry and its Applications to Sensors and Electronic Devices. Elsevier Science Publishers, 1988. p238-243.

[27] N. Nowak, K. Schwerdtfeger. "Determination of Mobilities of Fe^{2+}, Co^{2+}, Ni^{2+}, and Ca^{2+} in Silicate Melts at 1600°C by a Galvanostatic technique". Metal-Slag-Gas Reactions and Processes. Electrochemical Society Inc. 1975, p98-110.

[28] K. Nagata, K. Goto. "Electrochemical determination of quasi-binary interdiffusivity of CaO and SiO_2 in a blast-furnace type slag using a memory-type oscilloscope". Ironmaking and Steelmaking. 1, 1977, p23-28.

[29] J-Y. Tilquin, J. Glibert, P. Claes. "Qualitative and Quantitative Electrochemical Studies of Multivalent Elements in Molten Oxide Glasses". Electrochemica Acta. 38, 1993, p479-486.

[30] K. Suzumura, K. Kawamura, T. Yokokawa. "Voltammetric Studies on the Redox Behaviour of Cr, Mn, Cu, Sb, and As Ions in Na_2O-B_2O_3 Melts". J. Chem. Soc. Faraday Trans. 87, 1991, p307-312.

[31] Slag Atlas. Verein Deutscher Eisenhuttenleute edt. Verlag Stahleisen, 1981, p258.

[32] K. Mori. "Kinetics of Fundamental Reactions Pertinent to Steelmaking Process". ISIJ. 28, 1988, p246-261.

[33] A. Yazawa. "Slag-Metal and Slag-Matte Equilibria and their Process Implications". 2nd International Symposium on Metallurgical Slags and Fluxes. H. Fine, D. Gaskell, edts. American Insititute of Mining, Metallurgical, and Petroleum Engineers. 1984. p701-720.

[34] P. Riboud, L. Lucas. "Influence of Mass Transfer upon Surface Phenomena in Iron and Steelmaking". Canadian Metallurgical Quarterly. 20, 1981, p199-208.

[35] T. Dulski. "Classical Wet Analytical Chemistry". ASM Handbook: Materials Characterization Vol 10. ASM International. 1986.

[36] R. Levy, C. Lupis, P. Flinn. "Mossbauer analysis of the valence and coordination of iron cations in SiO_2-Na_2O-CaO glasses". Physics and Chemistry of Glasses. 17, 1976, p94-103.

[37] H. Schreiber, G. Balazs. "Mutual interaction of Ti, Cr, and Eu redox couples in silicate melts". Physics and Chemistry of Glasses. 22, 1981, p99-103.

[38] M. Cable, Z. Xiang. "Cuprous-Cupric equilibrium in soda-lime-silica glasses melted in air". Physics and Chemistry of Glasses. 30, 1989, p237-242.

[39] A. Lenhart, H. Schaeffer. "Redox Behavior of Glass Melts". Diffusion and Defect Data. 53-54, 1987, p335-344.

[40] W. Lankford, N. Samways, R. Craven, R. McGannon edts. The Making, Shaping and Treating of Steel. 10th Edition. Association of Iron and Steel Engineers, 1985, p482.

[41] E. Turkdogan et al. "Implementation of a Ladle Slag Oxygen Activity Sensor to Optimize Ladle Slag Practices at the US Steel Mon Valley Works". Iron and Steelmaker. July, 1997, p33-39.

[42] S. Geller, edt. Solid Electrolytes. Springer-Verlag. 1977. p143-221.

[43] S. Somiya, N. Yamamoto, H. Yanagida. Science and Technology of Zirconia III. American Ceramic Society. 1988.

[44] J. Hladik. Physics of Electrolytes. Academic Press. 1972.

[45] N. Claussen, M. Ruhle, A. Heuer. Science and Technology of Zirconia II. American Ceramic Society. 1984.

[46] M. Yoshimura. "Phase Stability of Zirconia". Ceramic Bulletin. 67, 1988, 1950-1955.

[47] J. Patterson. "Conduction Domains for Solid Electrolytes". Journal of the Electrochemical Society. July 1971, p1033-1039.

[48] C. Wagner. Z. Phys. Chem. B21, 1933, p25.

[49] H. Schmalzried. Z. Physik. Chem. NF 38, 1962, p87.

[50] T. Etsell, S. Flengas. "N-type Conductivity in Stabilized Zirconia Solid Electrolytes". Journal of the Electrochemical Society. 119, 1972, p1-7.

[51] M. Kleitz, P. Fabry et al. "Determination of electronic conductivities and ionic domains of ZrO_2-Y_2O_3 by semipermeability measurements". Advances in Ceramics – Science and Technology of Zirconia 3. A. Heuer, L. Hobbs edts. The American Ceramic Society, 1981. p349-363.

[52] P. Scaife, D. Swinkels, S. Richards. "Characterisation of Zirconia Electrolytes for Oxygen Probes Used in Steelmaking". High Temperature Science. 3, 1976, p31-47.

[53] M. Iwase, T. Yamasaki et al. "Measurements of the Parameter, P_{Θ}, for the Determinations of Mixed Ionic and N-Type Electronic Conduction in Commercial Zirconia Electrolytes". Trans. JIM. 25, 1984, p43-52.

[54] D. Swinkels. "Rapid Determination of Electronic Conductivity Limits of Solid Electrolytes". J. Electrochemical Soc. Oct 1970, p1267-1268.

[55] A. Kvist. "Chapter 8: Electrical Conductivity". Physics of Electrolytes. J. Hladik edt. Academic Press, 1972. p321.

[56] H. Tuller, A. Nowick. "Doped Ceria as a Solid Oxide Electrolyte". J. Electrochemical Society. 122, 1975, p255-259.

[57] F. Sanchez-Bajo, F. Cumbrera, F. Guiberteau, A. Dominguez-Rodriquez. "Microstructural characterization of Y-PSZ (4 mol%) polycrystals by means of X-ray diffraction experiments". Materials Letters. 15, 1992, p39-44.

[58] J. Bauerle. J. Phys. Chem. Solids. 30, p565, (1967).

[59] Slag Atlas. Verein Deutscher Eisenhuttenleute edt. Verlag Stahleisen, 1981, p68.

[60] Slag Atlas. Verein Deutscher Eisenhuttenleute edt. Verlag Stahleisen, 1981, p67.

[61] Slag Atlas. Verein Deutscher Eisenhuttenleute edt. Verlag Stahleisen, 1981, p57.

[62] Slag Atlas. Verein Deutscher Eisenhuttenleute edt. Verlag Stahleisen, 1981, p178.

[63] Slag Atlas. Verein Deutscher Eisenhuttenleute edt. Verlag Stahleisen, 1981, p7.

[64] H. Fine, D. Gaskel. 2nd International Symposium on Metallurgical Slags and Fluxes. American Institute of Mining, Metallurgical, and Petroleum Engineers, 1984.

[65] 5th International Conference on Molten Slags, Fluxes, and Salts. Iron and Steel Society, 1996.

[56] E. Turkdogan. Physicochemical Properties of Molten Slags and Glasses. The Metals Society, 1983.

[67] Slag Atlas. Verein Deutscher Eisenhuttenleute edt. Verlag Stahleisen, 1981.

[68] K. Goto. "Chapter 2: Ionic and Electronic Conduction of Solid and Liquid Oxides and of Other Ionic Compounds". Solid State Electrochemistry and its Applications to Sensors and Electronic Devices. Elsevier Science Publishers, 1988. p28.

[69] K. Goto. "Chapter 3: Relation Between the Conductivity and Diffusivity of Ions in Oxides". Solid State Electrochemistry and its Applications to Sensors and Electronic Devices. Elsevier Science Publishers, 1988. p55.

[70] S. Goto, M. Sasabe, M. Kawakami. Transactions ISIJ. 17, (1977), p213.

[71] Slag Atlas. Verein Deutscher Eisenhuttenleute edt. Verlag Stahleisen, 1981, p258.

[72] Q. Jiao, N. Themelis. Metallurgial Transactions B. 19B, (1988), p133.

[73] H. Engell, P. Vygen. Berichte der Bunsengesellschaft. 72, (1968), p5.

[74] E. Turkdogan. Physicochemical Properties of Molten Slags and Glasses. The Metals Society, 1983, p41.

[75] H. Keller, K. Schwerdtfeger. Metallurgical Transactions B. 17B, (1986), p497.

[76] N. Nowack, K. Schwerdtfeger. "Determination of Mobilities of Fe^{2+}, Co^{2+}, Ni^{2+}, and Ca^{2+} in Silicate Melts at 1600°C by a Galvanostatic Technique". Metal-Slag-Gas Reactions and Processes. Electrochemical Society Inc. 1975, p98.

[77] K. Goto, T. Kurahashi, M. Sasabe. Metallurgical Transactions B. 8B, (1977), p523.

[78] K. Nagata, N. Sata, K. Goto. ISIJ. 13, (1982), p1694.

[79] Fontana et al. Canadian Metallurgical Quarterly. Vol 20, 1981, No. 2, pp209-214.

[80] J. Bowker, C. Lupis, P. Flinn. Canadian Metallurgical Quarterly. 20, (1981), p69.

[81] Slag Atlas. Verein Deutscher Eisenhuttenleute edt. Verlag Stahleisen, 1981, p267.

[82] Slag Atlas. Verein Deutscher Eisenhuttenleute edt. Verlag Stahleisen, 1981, p202.

[83] A. Martin, G. Derge. Trans. AIME. 154, (1943), p104.

[84] C. Masson. Proc. Roy. Soc. A287, p201 (1965).

[85] D. Gaskell. Canadian Metallurgical Quarterly. 20, p3-19, 1981.

[86] D. Hyun, H. Shim. ISIJ, 28, p736-745, 1988.

[87] M. Selleby. Met. Trans. B. 28B, p563-576, 1997.

[88] M. Selleby, Met. Trans. B. 28B, p577-596, 1997.

[89] E. Turkdogan. Physicochemical Properties of Molten Slags and Glasses. The Metals Society, 1983, p236.

[90] T. Yokokawa, Canadian Metallurgical Quarterly, 20, p21-26, 1981.

[91] M. Temkin. Acta. Phys. Chim. USSR. 20, p411, 1945.

[92] M. Kawakami, K. Goto, M. Matsuoka. Met. Trans. B. 11B, p463-469, 1980.

[93] S. Jahanshahi, S. Wright. ISIJ International. 33, p195-203, 1993.

[94] J. Elliot, M. Gleiser, V. Ramakrishna. Thermochemistry for Steelmaking – Vol II. Addison-Wesley, 1963, p620.

[95] M. Timucin, A. Morris. Met. Trans. 1, p3193-3201, 1970.

[96] E. Ichise et al. Met. Trans. B. 28B, p243-250, 1997.

[97] E. Turkdogan, P. Bills. In 'Physical Chemistry of Process Metallurgy, Part I', p207, 1961, New York, Interscience.

[98] J. Bowker, C. Lupis, P. Flinn. Canadian Metallurgical Quarterly, 20, p69-78, 1981.

[99] E. Turkdogan et al. Iron and Steelmaker, 24, p33-39, 1997.

[100] M. Iwase et al. Met. Trans. B. 23B, p459-466, 1992.

[101] L. Pargamin, C. Lupis, P. Flinn. Met. Trans. 3, p2093-2105, 1972.

[102] E. Turkdogan. Physicochemical Properties of Molten Slags and Glasses. The Metals Society, 1983, p105.

[103] C. Wagner, Z. Elektrochem. 60, p4, 1956.

[104] M. Hebb. J. Chem. Phys. 20, p185, 1952.

[105] I. Riess. Solid State Ionics. 51, p219, 1992.

[106] S. Yuan, U. Pal, K. Chou. J. Electrochem. Soc. 141, p467, 1994.

[107] L. Tai, P. Lessing. J. Am. Ceram. Soc. 74, p155, 1991.

[108] S. Jahanshahi, S. Wright. ISIJ International. 33, p195, 1993.

[109] T. Arato, M. Tokuda, M. Ohtani. Tetsu-to-Hagane. 68, p2263, 1982.

[110] T. Ogura, M. Iwase et al. Met. Trans. B. 23B, p459, 1992.

[111] L. J. Swartzendruber. 1984. Binary Alloy Phase Diagrams.

[112] K. Vetter. Electrochemical Kinetics: Theoretical Aspects. Academic Press, 1967.

[113] A. Bard, L. Faulkner. Electrochemical Methods: Fundamentals and Applications. John Wiley and Sons, 1980.

[114] K. Vetter. Electrochemical Kinetics: Theoretical Aspects. Academic Press, 1967, p79.

[115] K. Serata, H. Inoue, M. Tokuda, and M. Ohtani. "Comments of the Analysis for Electrochemical Kinetics of Slag-Metal Systems at High Temperatures". From: Metal-Slag-Gas Reactions and Processes, Editors: Foroulis and Smeltzer. The Electrochemical Society, 1975, p50-62.

[116] T. Emi, T. Sakuraya, K. Sanbongi. "Kinetics of Oxygen Electrode Reaction at the Interface of Slag/Metal Boundaries". Ibid. p87-97.

[117] A. Bard, L. Faulkner. Electrochemical Methods: Fundamentals and Applications. John Wiley and Sons, 1980, p103, p165-166.

[118] B. Mikhailetz, A. Plischewski. Izv. Vuz. Chern. Met., 2, 1972, 20.

[119] R. Prange, K. Heusler, K. Schwerdtfeger. Met. Trans. B. 15B, 1984, p281-288.

[120] K. Serata, H. Inoue, M. Tokuda, M. Ohtani. "Comments of the Analysis for Electro-Chemical Kinetics of Slag-Metal Systems at High Temperatures". Gas-Slag-Metal reactions. p50-62.

[121] K. Vetter. Electrochemical Kinetics: Theoretical Aspects. Academic Press, 1967, p365.

[122] J. Macdonald. Impedance Spectroscopy: Emphasizing Solid Materials and Systems. John Wiley and Sons, 1987. p6.

[123] E. Warburg. "Uber das Verhalten sogenannter unpolarisierbarer Electroden gegen Wechselstron". Ann. Phys. Chem. 67, 1899, p493-499.

[124] A. Bard, L. Faulkner. Electrochemical Methods: Fundamentals and Applications. John Wiley and Sons, 1980, Chapter 10.

[125] H. Fujiwara, E. Ichises et al. "Thermodynamics of Iron Oxide in Fe_xO-Dilute CaO + Al_2O_3 + Fe_xO Fluxes at 1873K". Metallurgical Transactions B. 28B, 1997, p243-250.

[126] Q. Jiao, N. Themelis. Metallurgial Transactions B. 19B, (1988), p133.

[127] Slag Atlas. Verein Deutscher Eisenhuttenleute edt. Verlag Stahleisen, 1981, p267.

[128] Y. Nikitin, O, Esin. Dokl. Akad. Nauk SSSR, Fiz. Khim. 111, 1956, p133.

[129] A. Plischewski, A. Sotnikov, O. Esin. Electrokhimiya. 4, 1968, p304.

[130] T. Emi. "Slag-Metal Reactions from the Electrochemical Viewpoint". In: Electrochemistry, Physical Chemistry Series Two, Volume 6. Edts: A. Buckingham, J. Bockris. Butterworths, London, 1976, p277-332.

[131] T. Hirai, Y. Miura, K. Takahashi. Denki Kagaku, 40, 1972, p138.

[132] Slag Atlas. Verein Deutscher Eisenhuttenleute edt. Verlag Stahleisen, 1981, p202.

[133] Q. Jiao, N. Themelis. Metallurgical Transactions B. 19B, 1988, p133.

[134] Slag Atlas. Verein Deutscher Eisenhuttenleute edt. Verlag Stahleisen, 1981, p267.

[135] L. Pargamin, C. Lupis, P. Flinn. Met. Trans. 3, p2093-2105, 1972.

[136] E. Ichise et al. Met. Trans B. 28B, 1997, p243-250.

[137] H. Keller, K. Schwerdtfeger. Metallurgical Transactions B. 17B, (1986), p497.

[138] N. Nowak, K. Schwerdtfeger. "Determination of Mobilities of Fe^{2+}, Co^{2+}, Ni^{2+}, and Ca^{2+} in Silicate Melts at 1600°C by a Galvanostatic technique". Metal-Slag-Gas Reactions and Processes. Electrochemical Society Inc. 1975, p98-110.

[139] K. Goto, T. Kurahashi, M. Sasabe. Metallurgical Transactions B. 8B, (1977), p523.

[140] K. Nagata, N. Sata, K. Goto. ISIJ. 13, (1982), p1694.

[141] A. Sasahira, T. Yokokawa. Electrochemica Acta. 30, 1985, p441-448.

[142] T. Emi, T. Sakuraya, K. Sanbongi. "Kinetics of Oxygen Electrode Reaction at the Interface of Slag/Metal Boundaries". Metal-Slag-Gas Reactions and Processes. Electrochemical Society Inc. 1975, p87-97.

[143] M. Sasabe, Y. Kinoshita. Transactions ISIJ. 20, 1980, p801-809.

[144] T. Miyaki, A. Furuta, K. Kawamura, T. Yokokawa. 36, 1995, 36-40.

[145] A. Sotnikov, O. Esin, L. Barmin, A. Plischewski. Izv. V.U.Z. Chern. Metall. 7, 1967, p5. (got from Emi p320.)

[146] L. Tanner, H. Okamkoto. "The Pt-Si (Platinum-Silicon) System". J. Phase Equil. 12, 1991, p571-574.

[147] K. Serata, M. Tokuda, M. Ohtani. Japanese Article, vol 38, p566-573.

[148] W. Dickson, E. Dismukes. Trans. AIME. 224, 1962, p505-511.

[149] K. Nagata, T. Kawashima, K. Goto. ISIJ International. 32, 1992, p26-42.

[150] M. Simnad, G. Derge, I. George. Trans. AIME. 200, 1954, p1386-1390.

[151] Q. Jiao, N. Themelis. Metallurgical Transactions B. 19B, 1988, p133.

[152] K. Goto. "Chapter 2: Ionic and Electronic Conduction of Solid and Liquid Oxides and of Other Ionic Compounds". Solid State Electrochemistry and its Applications to Sensors and Electronic Devices. Elsevier Science Publishers, 1988. p28.

[153] H. Larson, J. Chipman. Trans. AIME. 197, p1089, 1953.

[154] E. Turkdogan. Physicochemical Properties of Molten Slags and Glasses. The Metals Society, 1983, p244.

[155] M. Timucin, A. Morris. Met. Trans. 1, p3193-3201, 1970.

[156] L. Pargamin, C. Lupis, P. Flinn. Met. Trans. 3, p2093-2105, 1972.

[157] E. Ichise et al. Met. Trans. B. 28B, p243-250, 1997.

[158] Schreiber et al. Journal of Non-Crystalline Solids. 38-39, p785-790, 1980.

[159] S. Jahanshahi, S. Wright. ISIJ International. 33, p195-203, 1993.

[160] J. Bowker, C. Lupis, P. Flinn. Canadian Metallurgical Quarterly, 20, p69-78, 1981.

[161] B. Phillips, A. Muan. J. Amer. Ceram. Soc. 42, 1959, p413.

[162] E. Turkdogan et al. Iron and Steelmaker, 24, p33-39, 1997.

[163] Slag Atlas. Verein Deutscher Eisenhuttenleute edt. Verlag Stahleisen, 1981.

[164] M. Iwase et al. Met. Trans. B. 23B, p459-466, 1992.

[165] M. Timucin, A. Morris. Met. Trans. 1, p3193-3201, 1970.

[166] H. Larson, J. Chipman. Trans. AIME. 197, p1089, 1953.

[167] E. Turkdogan. Physicochemical Properties of Molten Slags and Glasses. The Metals Society, 1983, p244.

[168] E. Turkdogan. Physicochemical Properties of Molten Slags and Glasses. The Metals Society, 1983, p105.

[169] Slag Atlas. Verein Deutscher Eisenhuttenleute edt. Verlag Stahleisen, 1981. p128.

[170] E. Turkdogan. Physicochemical Properties of Molten Slags and Glasses. The Metals Society, 1983, p142-146.

[171] M. Selleby, Met. Trans. B. 28B, p577-596, 1997.

[172] A. Fontana, L. Segers, R. Winand. Canadian Metallurgical Quarterly. 20, p209, 1980.

[173] J. Elliott, M. Gleiser, V. Ramakrishna. Thermochemistry for Steelmaking. Addison-Wesley 1963. p620.

[174] J. Macdonald. "CNLS". Operating manual for LEVM version 6.1 software. Solarton Instruments LTD. 1994.

[175] J. Macdonald. Impedance Spectroscopy. John Wiley and Sons. 1987.

[176] J. Hladik. Physics of Electrolytes – Volume 2. Academic Press, 1972. p883.